



2008-11-24

Design of a Three-Passage Low Reynolds Number Turbine Cascade with Periodic Flow Conditions

Daniel R. Rogers

Brigham Young University - Provo

Follow this and additional works at: <https://scholarsarchive.byu.edu/etd>



Part of the [Mechanical Engineering Commons](#)

BYU ScholarsArchive Citation

Rogers, Daniel R., "Design of a Three-Passage Low Reynolds Number Turbine Cascade with Periodic Flow Conditions" (2008). *All Theses and Dissertations*. 1630.

<https://scholarsarchive.byu.edu/etd/1630>

This Thesis is brought to you for free and open access by BYU ScholarsArchive. It has been accepted for inclusion in All Theses and Dissertations by an authorized administrator of BYU ScholarsArchive. For more information, please contact scholarsarchive@byu.edu, ellen_amatangelo@byu.edu.

DESIGN OF A THREE-PASSAGE, LOW REYNOLDS NUMBER TURBINE
CASCADE WITH PERIODIC FLOW CONDITIONS

by

Daniel R. Rogers

A thesis submitted to the faculty of

Brigham Young University

in partial fulfillment of the requirements for the degree of

Master of Science

Department of Mechanical Engineering

Brigham Young University

December 2008

Copyright © 2008 Daniel R. Rogers

All Rights Reserved

BRIGHAM YOUNG UNIVERSITY

GRADUATE COMMITTEE APPROVAL

of a thesis submitted by

Daniel R. Rogers

This thesis has been read by each member of the following graduate committee and by majority vote has been found to be satisfactory.

Date

Steven E. Gorrell, Chair

Date

Dale R. Tree

Date

Scott L. Thomson

BRIGHAM YOUNG UNIVERSITY

As chair of the candidate's graduate committee, I have read the thesis of Daniel R. Rogers in its final form and have found that (1) its format, citations, and bibliographical style are consistent and acceptable and fulfill university and department style requirements; (2) its illustrative materials including figures, tables, and charts are in place; and (3) the final manuscript is satisfactory to the graduate committee and is ready for submission to the university library.

Date

Steven E. Gorrell
Chair, Graduate Committee

Accepted for the Department

Larry L. Howell
Graduate Coordinator

Accepted for the College

Alan R. Parkinson
Dean, Ira A. Fulton College of
Engineering and Technology

ABSTRACT

DESIGN OF A THREE-PASSAGE, LOW REYNOLDS NUMBER TURBINE CASCADE WITH PERIODIC FLOW CONDITIONS

Daniel R. Rogers

Department of Mechanical Engineering

Master of Science

A numerical method for modeling a low Reynolds number turbine blade, the L1M, is presented along with the pitfalls encountered. A laminar solution was confirmed to not accurately predict the flow features known in low Reynolds number turbine blade flow. Three fully turbulent models were then used to try to predict the separation and reattachment of the flow. These models were also found to be insufficient for transitioning flows. A domain was created to manually trip the laminar flow to turbulent flow using a predictive turbulence transition model. The trip in the domain introduced an instability in the flow field that appears to be dependent on the discretization order, turbulence model, and transition location. The method was repeated using the Pack B blade and the same obstacles were apparent.

The numerical method developed was then used in an optimization technique developed to design a wind tunnel simulating periodic flow conditions using only 2 blades. The method was first used to predict a c_p distribution for the aft loaded L1A research blade provided by the U.S. Air Force. The method was then extended to a larger domain emulating the 2 blade, 2D wind tunnel. The endwall geometry of the tunnel was then changed

using previously defined control points to alter the distribution of c_p along the suction surface of the interior blades. The tunnel c_p 's were compared to the computationally acquired periodic solution. The process was repeated until an acceptable threshold was reached. The optimization was performed using the commercially available software iSIGHT by Engineous Solutions. The optimization algorithms used were the gradient based Successive Approximation Method, the Hooke Jeeves, and Simulated Annealing.

ACKNOWLEDGMENTS

I am grateful for the knowledge and guidance of my graduate advisor, Dr. Steven Gorrell, and for Dr. Deryl Snyder, and Dr. Jeffrey Bons who have also put many hours into this research project. Many thanks to the BYU Supercomputing Center, especially Lloyd Brown, who has been there with every answer and every fix needed to get my research off the ground. I would also like to acknowledge the financial support from the Air Force Office of Scientific Research, with Lt. Col. Rhett Jefferies as program manager, who has partially funded this project. To my amazing wife who has given me the motivation and desire to finish this work.

Table of Contents

List of Tables	xii
List of Figures	xiv
Chapter 1 Introduction	1
1.0.1 Periodic Conditions	2
1.0.2 Experimental Techniques	5
1.0.3 Optimization	7
1.0.4 Objective	8
Chapter 2 CFD Model	11
2.1 Model	13
2.2 Results-L1M	15
2.2.1 Laminar Solution	15
2.2.2 Turbulence Model	17
2.2.3 Turbulent Trip	18
2.2.4 Transition Models	20
2.3 Results-Pack B	23
2.3.1 Pack B Application	23
2.4 Conclusions from CFD Model Development	24
Chapter 3 Mesh Manipulation	27
3.1 Original Experimental Configuration	27
3.1.1 Experimental Methods of c_p Matching	28
3.2 New Test Section Configuration	29
3.2.1 Model Definition	30
3.3 Parametric Study of Design Variables	32

3.3.1	The Variables	32
3.3.2	Parametric Study	34
3.4	Summary	39
Chapter 4	Optimization	41
4.1	Introduction	41
4.2	Method	43
4.3	Results	48
4.3.1	Original Domain	48
4.3.2	Narrow Tunnel	51
4.3.3	Reynolds Number	54
4.3.4	Longer Nozzle	56
4.3.5	Full Tunnel	60
4.3.6	Successive Approximation Summary	64
4.3.7	Optimization Method Change	66
4.3.8	Separating Streamline	76
4.4	Summary and Analysis	80
4.4.1	Recommendations	86
Chapter 5	Summary & Conclusions	89
5.1	CFD Model	89
5.2	Mesh Manipulation	89
5.3	Optimization	90
5.4	Continuation and Improvement	92
References	93
Appendix A	Resources	97
A.1	Sample Matlab Code	97
A.2	Full Tunnel Journals	99
A.2.1	Gambit	99
A.2.2	Fluent	102
A.3	Test Section Journals	106

A.3.1	Gambit	106
A.3.2	Fluent	109
A.3.3	UDF Fluent Files	113
A.4	Streamline ICEM Coordinates	116

List of Tables

2.1	Separation Locations for Various Models and Cases in % Axial Chord . . .	16
2.2	Transition Locations for the Pack B and LIM blades in % Axial Chord . . .	21
4.1	<i>R.S.</i> for Successive Approximation Method	65
4.2	<i>R.S.</i> for All Optimization Cases	82

List of Figures

1.1	Global Hawk UAV	2
1.2	Shows location of low pressure turbine in a turbofan engine.	3
1.3	The computational solution for LPT blade with no turbulent transition (left) and the experimental contour plot of velocity magnitude for a LPT blade showing the reattachment of flow (right).	3
1.4	Periodic heat exchanger configuration.	4
1.5	Turbine blade configurations showing (a) annular blade rows and (b) an example of a linearized blade cascade.	5
1.6	Experimental tunnel cascade implementing suction and tailboard movement for a 35° inlet flow angle.	7
2.1	Experimental contour plot of velocity magnitude for the L1M blade.	12
2.2	(a) The periodic computational domain of the Pack B cascade with periodic boundary shown by the white lines, and (b) the boundary layer mesh on the blade.	13
2.3	Grid refinement study for the L1M blade, showing a coarse and fine mesh c_p distribution.	14
2.4	Grid refinement study for the Pack B blade, showing a coarse and fine mesh c_p distribution.	15
2.5	Stream function of the laminar solution for the L1M at $Re=20,000$	16
2.6	Fluent solutions of the L1M cascade using the Spallart-Almaras, $k - \epsilon$, and $k - \omega$ turbulence models compared to experimental data.	17
2.7	The laminar and turbulent zones (a) initial domain, and (b) second attempt .	18

2.8	The Fluent solutions to the tripped turbulent solutions using the experimental transition data and the Spallart Almaras, $k - \varepsilon$, and $k - \omega$ turbulence models, compared to the experimental data for the L1M blade.	19
2.9	The Fluent solutions to the 1st and 2nd order tripped turbulent solutions using the experimental transition data and the $k - \omega$ turbulence model, compared to the experimental data.	20
2.10	The Fluent solutions to the tripped turbulent solutions using the Praisner and Clark transition data, compared to the experimental data for the L1M blade.	22
2.11	Computational contour plot using the $k - \varepsilon$ turbulence model and $Re=20,000$ and experimental contour plot of velocity magnitude for the L1M blade. . .	22
2.12	The Fluent solutions to the non-tripping turbulent solutions using Spallart Almaras, $k - \varepsilon$, and $k - \omega$ models, compared to the experimental data for the Pack B blade.	23
2.13	The Fluent solutions to the tripped turbulent solutions using Praisner and Clark's method of predicting transition and the experimental values for transition compared to the experimental data for the Pack B blade.	25
3.1	Original experimental tunnel configuration showing the last portion of the 9m section to the outlet of the test section.	28
3.2	Original experimental tunnel test section configuration.	29
3.3	The computational domain based on the geometry of the original wind tunnel.	31
3.4	Structured boundary layer mesh transitioning to unstructured triangular grid.	32
3.5	Changes in spacing between the walls and the blades for three cases, 9% smaller than design, design spacing, and 10% larger than design.	33
3.6	Tail boards shifted out for each case of pitch.	34
3.7	Blades shifted up and forward compared to the original domain.	35
3.8	Comparisons of the c_p distribution for variations in wall spacing.	36
3.9	Comparisons of tail board shift compared to original configuration for the smaller wall spacing.	37

3.10	Comparisons of tail board shift compared to original configuration for the original wall spacing.	37
3.11	Comparisons of tail board shift compared to original configuration for the larger wall spacing.	38
3.12	Comparisons of c_p for shifted blade compared to original configuration. . .	38
4.1	Flow chart of steps in the global iteration process.	44
4.2	c_p distribution for the L1A LPT blade calculated from the CFD model of Chapter 2.	44
4.3	Tunnel domain with the variable control points on the top and bottom surfaces.	46
4.4	Percent error of both tunnel blades compared to periodic solution for the original optimization domain.	49
4.5	Tunnel geometry showing the large bulge on the pressure wall of the tunnel and the velocity magnitude contours for the original optimization domain. .	50
4.6	c_p of both tunnel blades compared to the periodic solution.	50
4.7	Tunnel geometry showing the large bulge on the pressure wall of the tunnel for the narrow tunnel case.	52
4.8	c_p distribution of the narrow tunnel using the successive approximation optimization method.	53
4.9	Percent error of both tunnel blades compared to periodic solution for the narrow tunnel domain.	53
4.10	Velocity angle of the incoming flow at various c_x locations for the narrow tunnel domain.	54
4.11	Tunnel geometry and velocity contours for the variable Reynolds number case, $Re=15,550$	56
4.12	c_p distribution of the variable Reynolds number case, $Re=15,550$ using the successive approximation optimization method.	57
4.13	Percent error of both tunnel blades compared to periodic solution for the case of variable Reynolds number, $Re=15,550$, using the successive approximation method.	57

4.14	Optimized end wall geometry and velocity magnitude contours for the case of extended nozzle length.	59
4.15	c_p distribution of the extended nozzle length case using the successive approximation optimization method.	59
4.16	Percent error of both tunnel blades compared to periodic solution for the case of extended nozzle length entering the test section.	60
4.17	Full tunnel control point configuration, where B1 and TA are the added control points.	61
4.18	Full tunnel configuration including $12c_x$ upstream from the inlet plane of the blade row and velocity magnitude contours.	62
4.19	Close up view of the tunnel geometry showing the large bulge on the pressure wall of the tunnel and velocity magnitude contours for the full tunnel geometry using the successive approximation optimization method.	63
4.20	Showing the c_p distribution of the extended tunnel using the successive approximation optimization method.	64
4.21	Percent error of both tunnel blades compared to periodic solution for the extended tunnel case.	65
4.22	Tunnel geometry showing the end wall geometry of the tunnel and velocity magnitude contours for the narrow domain case using (top) the successive approximation, and (bottom) the simulated annealing optimization method.	68
4.23	c_p distribution of the narrow domain using (a) the successive approximation optimization method and (b) the simulated annealing method.	69
4.24	Percent error of both tunnel blades compared to periodic solution for the case of reduced width of the tunnel for (a) the successive approximation and (b) simulated annealing methods.	69
4.25	Tunnel geometry showing the large bulge on the pressure wall of the tunnel and velocity magnitude contours for the variable Reynolds number case for both optimization methods	70
4.26	c_p distribution of the variable Reynolds number using (a) the successive approximation and (b) simulated annealing optimization methods.	71

4.27	Percent error of both tunnel blades compared to periodic solution for the case of variable Reynolds number using (a) the successive approximation and (b) simulated annealing methods.	72
4.28	Tunnel geometry showing the end wall geometry and velocity contours of the optimized solution for the case of extended nozzle length using the (top) successive approximation and (bottom) simulated annealing optimization methods.	73
4.29	c_p distribution of the extended nozzle length case using (a) the successive approximation and (b) the Hooke-Jeeves optimization method.	74
4.30	Percent error of both tunnel blades compared to periodic solution for the case of extended nozzle length entering the test section using (a) the successive approximation and (b) the Hooke-Jeeves optimization methods.	74
4.31	Characteristics of the test section geometry and velocity magnitude contours of the full tunnel case for the (top) successive approximation and (bottom) Hooke-Jeeves optimization methods	75
4.32	c_p distribution of the full tunnel using (a) the successive approximation and (b) the Hooke-Jeeves optimization methods.	76
4.33	Percent error of both tunnel blades compared to periodic solution for the full tunnel case using (a) the successive approximation and (b) the Hooke-Jeeves optimization methods.	77
4.34	Tunnel geometry and velocity magnitude contours using the separating streamline end wall from the best Hooke-Jeeves extended tunnel case.	78
4.35	c_p distribution using the separating streamline end wall from the best Hooke-Jeeves extended tunnel case.	78
4.36	Percent error using the separating streamline end wall from the best Hooke-Jeeves extended tunnel case.	79
4.37	Tunnel geometry using the smooth separating streamline end wall from the best Hooke-Jeeves extended tunnel case.	80
4.38	c_p distribution using the smooth separating streamline end wall from the best Hooke-Jeeves extended tunnel case.	81

4.39	Percent error using the smooth separating streamline end wall from the best Hooke-Jeeves extended tunnel case.	81
4.40	Optimized tunnel domain using the smooth separating stream line compared to the initial optimization domain.	85
4.41	Optimized tunnel c_p using the smooth separating stream line compared to the initial domain c_p	86

Chapter 1

Introduction

The Global Hawk unmanned air vehicle (UAV), seen in Figure 1.1 initiated the investigation of very low Reynolds (Re) number flows through low pressure turbines (LPT). A schematic showing the components of a typical jet engine is shown in Figure 1.2. The LPT is found near the end portion of the engine just before the nozzle. During development of the engine it was found that because of the flight envelope of the aircraft, i.e. cruise altitude of 60,000 feet and the ability to loiter in an area for an extended period of time, the Reynolds number of the flow seen by the turbine was as low as 10,000 to 25,000 [1]. Operating at this low Reynolds number decreased the efficiency and power output of the LPT dramatically. The reason for the decrease was due to the complex flow field found in the LPT. Specifically, the laminar boundary layer along the turbine blade was prone to separate along the suction surface. This separation reduced the available lift on the blade and was a major limitation in LPT performance. This loss in efficiency reduced the range, loiter ability, and electrical power that was needed in the surveillance UAV. To increase efficiency at low Re , flow control is being studied as a means to reduce flow separation.

Some of the ideas under evaluation are passive surface protrusions and recesses, electro static discharge devices, heated wires, MEMs actuators, and vortex generating jets [2]. To study the flow control effects, high turning angle blades have been developed that purposely create a flow separation. If the blade has enough turning for the flow to separate, two things can occur. One, the flow will reattach to the blade, or two, the separated region will extend beyond the trailing edge of the blade and become an unsteady flow, shedding vortices off the trailing edge of the blade. Figure 1.3 shows both of these possibilities. Reattachment to the blade has been hypothesized to be caused by the transition of the shear



Figure 1.1: Global Hawk UAV, Photo by George Rothmaller, Courtesy of Air Force News.

layer to turbulence [3]. The extension of separation beyond the trailing edge of the blade leads to the most loss, in some turbine configurations as much as 7% [4].

To produce accurate data from the numerous experiments needed to test all the methods of flow control and increase understanding of the complex flow field generated by the LPT blade, the methods of modeling and analyzing the flow field, both experimental and computational, must be improved.

1.0.1 Periodic Conditions

Periodicity is a flow condition that plays an integral role in turbomachinery research. A periodic flow field is defined as the repetition of small domains to create a larger domain. An example of this is a radiator that has multiple heat exchanger fins repeated multiple times, a square inch can define the whole radiator. This allows a solution of a smaller portion of the domain to solve for the whole domain. There are many naturally oc-

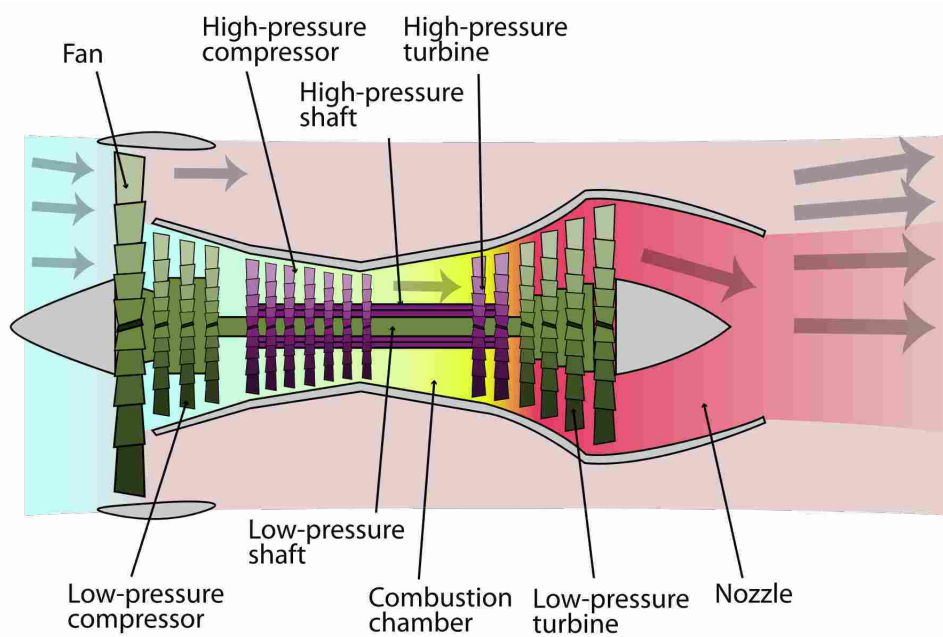


Figure 1.2: Shows location of low pressure turbine in a turbofan engine.

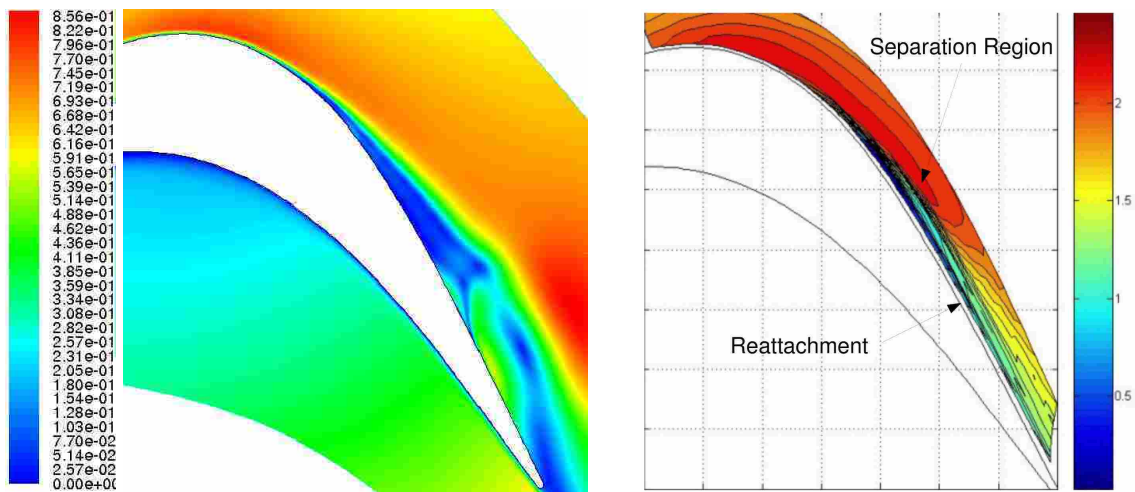


Figure 1.3: The computational solution for LPT blade with no turbulent transition (left) and the experimental contour plot of velocity magnitude for a LPT blade showing the reattachment of flow (right).

curing periodic domains. A computationally based explanation of periodicity is presented by Patankar [5] and is summarized below. This approach provides the basis of experimental and computational periodic flows.

Consider calculating the flow field of Figure 1.4. This configuration can be described by a repetition of identical smaller domains. This configuration is commonly found in heat exchangers and heat transfer augmentation devices. The entire domain is large and would require an excessive amount of computational resources to solve the flow field numerically. The alternative to solving the whole domain is to separate the large domain by repeatable smaller sections, as seen by the dashed lines in Figure 1.4. These sections that have the same geometry, if fully developed, will also have the same temperature and velocity fields. This allows the calculation of a much smaller, less computationally expensive domain. Because the flow fields for each smaller domain are the same, the inlet and outlet conditions are the same.

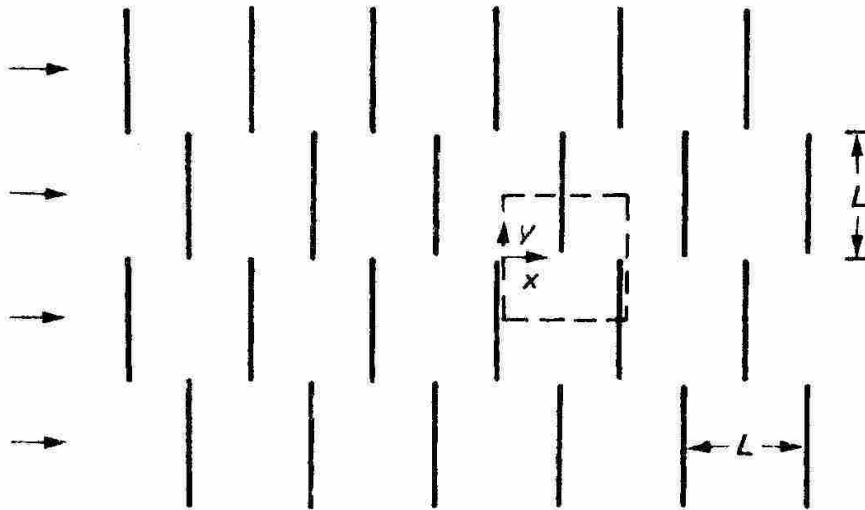


Figure 1.4: Periodic heat exchanger configuration.

In solving the flow for this geometry the inlet and exit velocities of the domain are not known and are not needed. If the smaller domain is repeated in rows, the domain exit plane is the exact same as the domain inlet plane, thereby making all the fluid properties and vectors for the two planes equal. So all that is needed is an initial average condition to begin the numeric calculation. This method assumes that all the streamwise stations are arranged as if it were in an infinite loop. This is also applicable if the domain was repeated in columns. The top and bottom boundaries of the columns would be the same.

This method for calculating periodic heat exchanger flow can also be used to model a turbine blade row. Turbine blades are usually evenly spaced in the circumferential direction. This means that the blade row can be broken into smaller domains including just one blade or one passage (space between blades). The domain created in this situation is only partially periodic. The inlet and outlet conditions are not equal because the small number of blade rows. This requires inlet values to be known. The rotational direction, however, is periodic. So the boundaries separating each individual blade have the same values of velocity and other fluid properties. For this case the assumption is that the blades are stacked on top of each other creating an endless row of blades as can be seen in Figure 1.5. The annulus or blade row is accurately modeled in this manner because it really is an endless loop of blades.

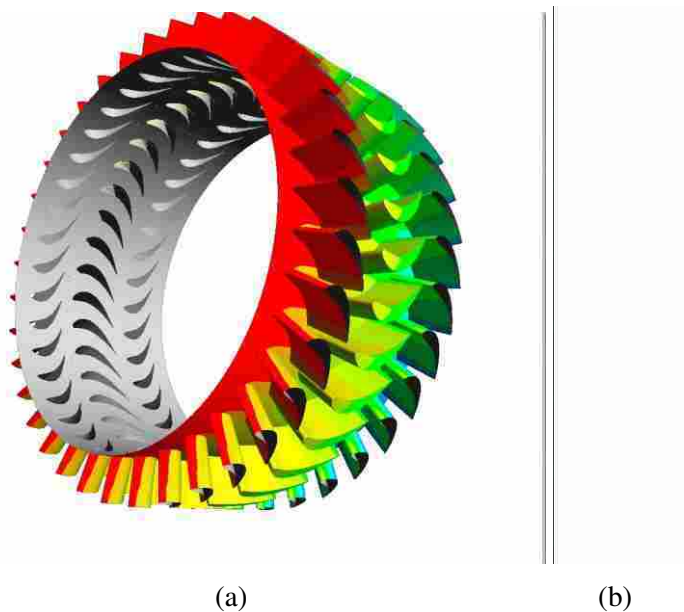


Figure 1.5: Turbine blade configurations showing (a) annular blade rows and (b) an example of a linearized blade cascade.

1.0.2 Experimental Techniques

Experimental studies are an important means of analyzing the flow fields and investigating critical flow features. In complex flow fields, especially those with turbulence generation, a high resolution study of the flow fields is needed. Experimental resolution

is based on how many data points can be taken in an specific area of the domain. More data points result in better resolution. A widely used practice is to build linear blade cascades for experiments and use only the data from the interior blades where the flow is most periodic. This way the periodic conditions are simulated if enough blades are included. However, using a multiple blade cascade increases the size of the experimental configuration and increases the required mass flow rate of the tunnel. Based on the Reynolds number relationship between length, l and velocity, u where $Re = \frac{ul}{\nu}$, the smaller blade chord increases the necessary velocity, while the large blades will decrease the velocity. If too small a cascade is used there is not enough useful resolution, or not enough data points to accurately define the flow. To increase the resolution of the experiment it is advantageous to reduce the blade count of the cascade and make the blade larger. This reduction of blades and increased size allows increased optical access, and the ability to increase the number of data points taken in a specific domain region. The problem then is keeping the periodic behavior of the blade cascade.

In reality, periodic conditions are not exactly maintained in a wind tunnel configuration. The boundary layer created by the wind tunnel wall causes the flow fields of the blades nearest the wall to change. The difference in the near wall blade's flow field propagates through the rest of the domain. If there are enough blades, the innermost blades will represent the nearest periodic flow. As discussed previously, too many blades can greatly influence cost and resolution of the experiment. Currently, periodicity has been maintained by using suction to remove the upstream boundary layer and tailboards [3]. Figure 1.6 shows the experimental cascade used by Bons et al. [6] where suction and tailboard movement was used to adjust the pressure coefficient, c_p , distribution where $c_p = \frac{p - p_{ref}}{\frac{1}{2}\rho_{ref}v_{ref}^2}$, p =static pressure, p_{ref} =reference pressure (atmospheric), ρ_{ref} =reference density (for air $\rho_{ref} = 1.225$), and $v_{ref} = 1 \frac{m}{s}$ was the reference velocity. The c_p used in Chapter 2 was defined differently to match the data of Bons et al. [6] as $c_p = \frac{p_{T,in} - p_{local}}{p_{T,in} - p_{S,in}}$ where $p_{T,in}$ =total inlet pressure, p_{local} =local static pressure, and $p_{S,in}$ =static inlet pressure. These experimental methods can be tedious to implement [7]. The comparison of experimental data to CFD can also be problematic due to the varying inlet conditions. The resolution of the experimental study could be improved, resulting in much more data of smaller scales that

could be recorded and analyzed. In the case of low Re turbine blades where a shear layer transition to turbulence occurs, more spatial resolution would significantly increase the understanding of the system. This would directly benefit the current research in LPT flow control. To create a wind tunnel that creates a periodic flow field of a blade row with a low number of blades greatly increases the experimental resolution of the experimental measurements and eliminates the inconsistencies of tailboard movement and the immeasurable amounts of suction.

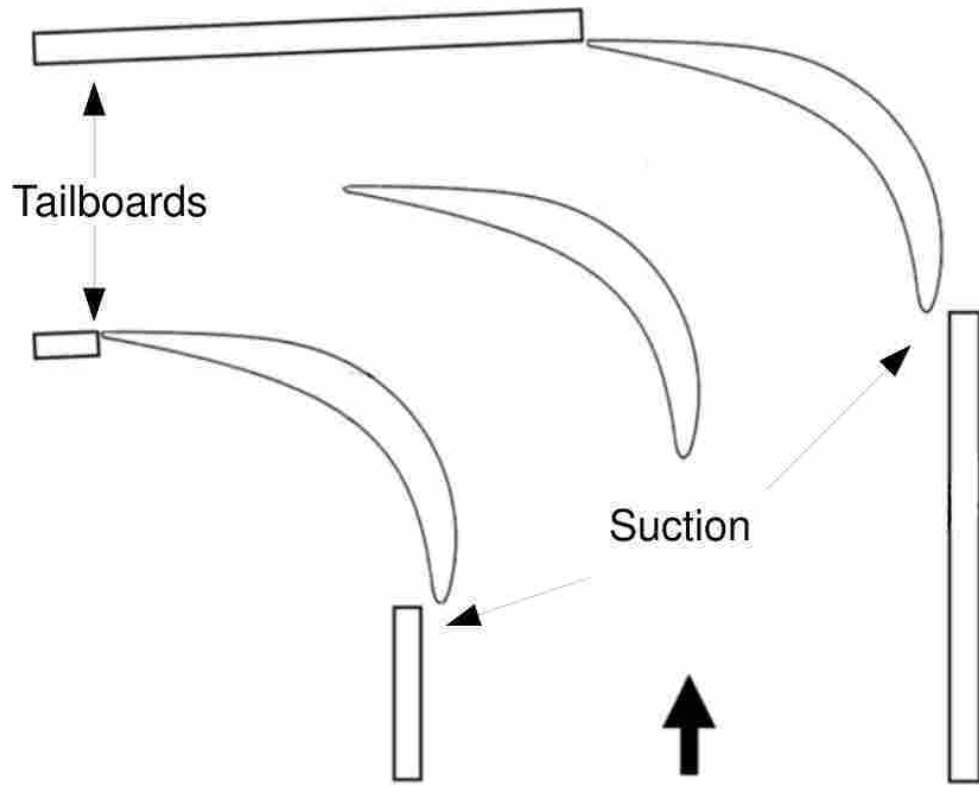


Figure 1.6: Experimental tunnel cascade implementing suction and tailboard movement for a 35° inlet flow angle.

1.0.3 Optimization

In an inviscid flow field, the end walls of the tunnel would simply need to follow the streamlines of the periodic solution and the respective surfaces of the blade. In the case of a real experiment, viscosity is a major contributor to the near wall flow and the

wall geometry is not as easily defined. The definition of the wall geometries needed for the viscous experiments could be solved using numerical simulations. As discussed previously, the flow field of this type separates and can either reattach or the wake can extend off the trailing edge of the blade. Both outcomes have disadvantages. At this point in time there is not an adequate RANS turbulence model capable of predicting the transition of the laminar separation on the blade, and unsteady cases are computationally expensive. A new method of solving transition flows, the $k - kl - \omega$ model, has recently been included in a developmental beta version of Fluent. This model was introduced after the development of the method presented here. The new $k - kl - \omega$ method could greatly simplify flow analysis if it is found to sufficiently predict LPT flows. Large eddy simulations (LES) studies have been performed by Gross et al. [8], [9], and have shown an accurate prediction of the flow field for the described LPT separation zones and reattachment. LES, however, is very expensive computationally and does not lend itself well to iterative optimization.

Recent studies by Laskowski et al. [10]. have shown the successful application of optimization techniques in solving the boundary geometry of an experimental wind tunnel's walls for a transonic turbine blade flow. This application was based on computational fluid dynamics (CFD) using a RANS $k - \epsilon$ model, and an iterative approach to solve for the wall shape that produced periodic flow between blades. The main difference for this research is the extension of the idea to low Reynolds number flows, which as previously discussed introduces different physical flow characteristics.

1.0.4 Objective

The objective of this research is to design a periodic linear cascade of LPT vanes by optimizing tunnel wall geometry based on CFD simulations using an automated iterative optimization technique. The experimental tunnel used by Bons et al. [6] was used to define inlet dimensions and conditions of the periodic tunnel cascade. The first step in this process was to obtain a method of numerically solving the complex flow field of low Reynolds number, high turning angle turbine blades using readily available commercial codes, and highlight potential pitfalls of using CFD for separated transitional flows. Then the periodic wind tunnel could be designed by iteratively manipulating the geometry of the end walls until the c_p distributions of both blades in the domain match the c_p distribution obtained

through the periodic numerical solution of step 1. The final design was determined by matching the c_p of the periodic solution and a visual inspection of the manufacturability of the end wall geometry. Each step of the modeling and optimization processes will be explained, and a conclusion made on the effectiveness of the techniques.

The CFD model developed to accurately predict the flow fields of reattaching LPT blades is presented in Chapter 2. The model was then used to define cascade design guidelines. Chapter 3 presents cascade design guidelines determined from a parametric analysis of tunnel wall spacing, tailboard shifting, and blade shifting. The optimization was then run using control points to define the end wall geometry of the domain. The optimization runs, their results, and a discussion of results is presented in Chapter 4. Conclusions and recommendations are given in Chapter 5

Chapter 2

CFD Model

To use an optimizing routine to find the tunnel end wall geometry, an accurate prediction of the desired flow field must be calculated. This prediction could come from already existing experimental data, or for the case of a new blade that has no experimental data, it could come from a CFD calculation. Some CFD models have been used to predict LPT blade flow fields that transition to turbulence along the blade surface [9]. However, the methods used do not lend themselves well to iterative processes of optimization due to the computational cost of the methods. This chapter will present a method developed to solve for an accurate pressure coefficient, c_p , prediction. This method was validated using the experimental c_p distributions of the Pack B and L1M blades. The method was then used in the following chapters, to solve the periodic flow field of a new research blade with no experimental data.

The nature of low pressure turbine blades at low Reynolds numbers poses many problems for computational modeling. Experimental and computational studies of two research turbine blades has greatly advanced understanding of the flow field. The Pack B blade profile is a Mach number scaled adaption of a highly loaded LPT blade by Pratt & Whitney. The design solidity, $\sigma = \frac{c_x}{s}$, where c_x = axial chord and s = blade spacing, for the blade is 1.13 and has an inlet flow angle of 35° and exit angle of 55° [6]. The L1M is a mid-loaded (maximum lift on the middle section of the blade) variation of the Pack B designed by the Air Force Research Laboratory [11]. The L1M has a solidity of 0.99 and the same design inlet and exit flow angles as the Pack B [3]. An LES study performed on these blades by Gross et al. [8], [9] at $Re=25,000$, showed the flow fields over both blades had significant separation, and each blade had a unique axial location of separation. Separation for the L1M was predicted at $57\%c_x$. The behavior of flow over the blade was

also presented in experimental studies by Bons et al. [3]. In this study, the inlet had a free stream turbulence level of 3% intensity and $Re=20,000$. The flow consisted of laminar boundary layer growth despite the existence of free-stream turbulence. The combination of the boundary layer growth and the curvature of the blades in the cascade caused separation to occur. If the transition to turbulence occurs in the separated free shear layer the flow can then reattach to the blade. For the L1M blade at these flow conditions, flow separation was identified at $59\%c_x$ and reattachment was noted at $73\%c_x$. This separation and reattachment can be seen in Figure 2.1, an experimental contour plot created by Reimann et al. [12]. Bons et al. [3] hypothesized that the cause of this reattachment was boundary layer transition to turbulence. The location of reattachment is a function of Reynolds number, blade curvature, blade spacing and free stream turbulence.

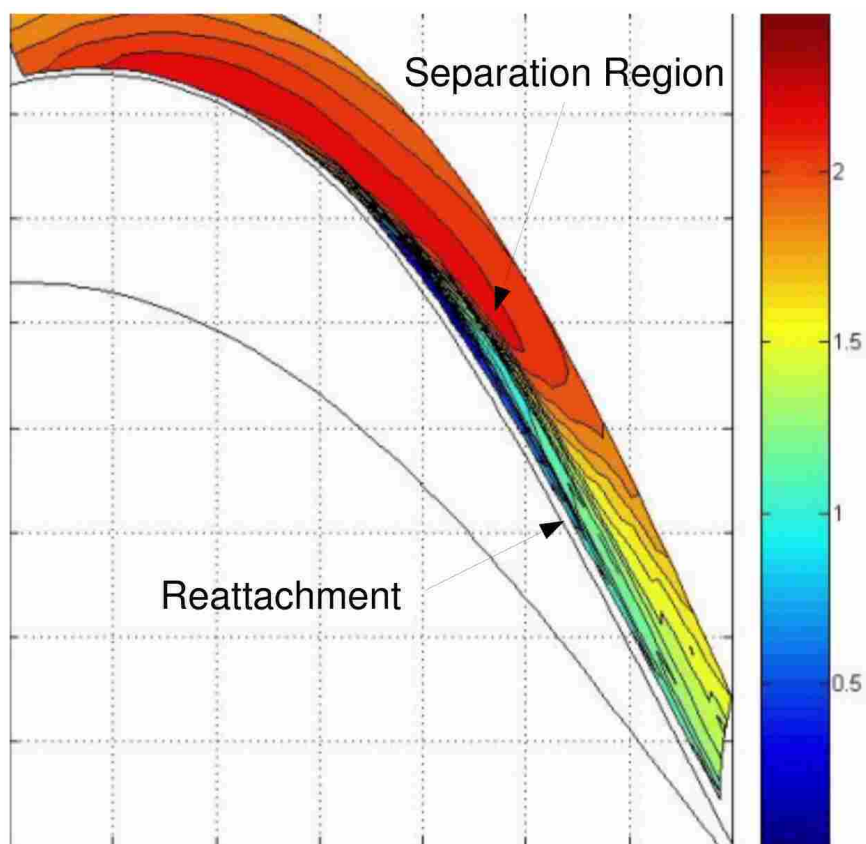


Figure 2.1: Experimental contour plot of velocity magnitude for the L1M blade [12].

2.1 Model

The steady, incompressible, Navier Stokes equations (RANS equations in the case of turbulent simulations) were integrated using an unstructured, segregated, pressure-based finite-volume procedure as implemented within the Fluent version 6.2 solver (Fluent, Inc., Lebanon, New Hampshire). The solution/discretization procedure, employed pressure-velocity coupling using the SIMPLEC algorithm [13]. Differencing of the convective terms in the momentum and turbulence equations used a 1st order upwind scheme.

The program Gambit (by ANSYS) was used to create the computational grid. The domain consisted of a two dimensional single blade with periodic conditions imposed at approximately the mid-passage (see Figure 2.2). The domain extends $.3 c_x$ upstream of the leading edge with a velocity inlet condition and a velocity flow angle of 35° and an outflow boundary $.5 c_x$ downstream from the trailing edge of the blade. Near the blade, a structured quad mesh was generated to capture the boundary layer, also shown in Figure 2.2.

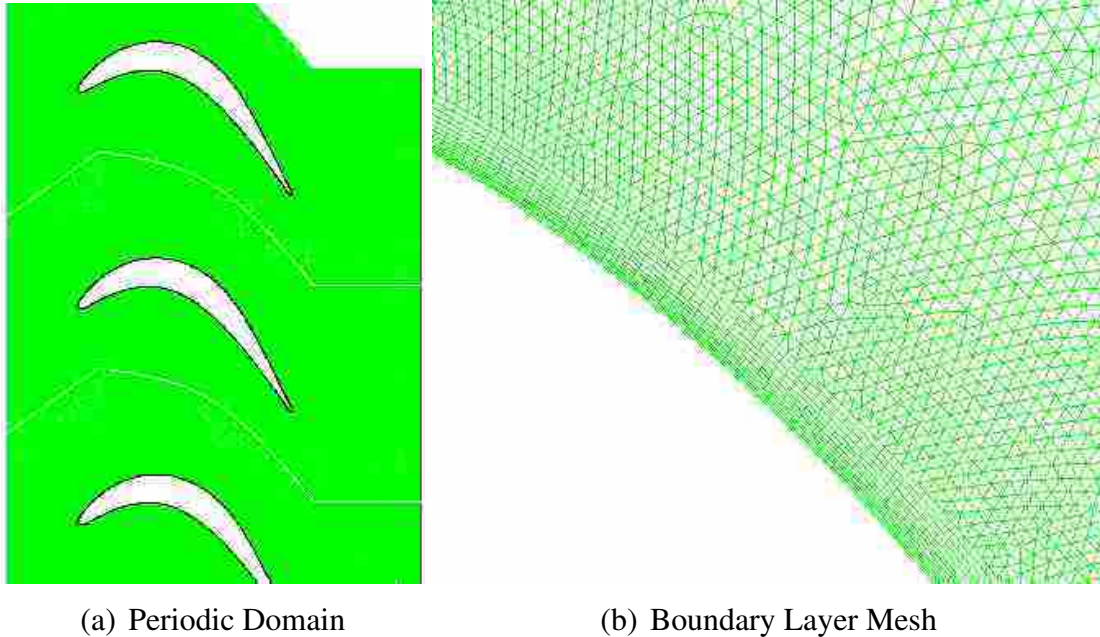


Figure 2.2: (a) The periodic computational domain of the Pack B cascade with periodic boundary shown by the white lines, and (b) the boundary layer mesh on the blade.

This boundary mesh had a spacing of $h/c_x = .0005$ for the first point off the wall, and extended approximately $h/c_x = .00516$ from the wall and $y^+ \leq 1$. Outside the bound-

ary mesh, unstructured triangles were used to mesh the remainder of the domain. Approximately 125 points were used along the upper and lower blade surfaces. In total, approximately 40,000 total cells were used in the mesh. A second, finer mesh containing 80,000 cells was used to indicate grid convergence based on the c_p distribution on the suction surface. Figures 2.3 and 2.4 show the pressure coefficient, c_p , distribution for the L1M and Pack B blades respectively. A third grid of 120,000 cells was created and showed the same solution as the 80,000 cell grid. The two solutions were calculated assuming fully turbulent $k - \epsilon$ flow to avoid any complications introduced by separated flow regions that are common on LPT blades. It can be seen from the figure that the two grids, coarse and fine, produced similar results. This indicates that the fine grid used was good enough for the calculations. The parameters of the boundary layer and growth of the grid cells were held constant for all following grids.

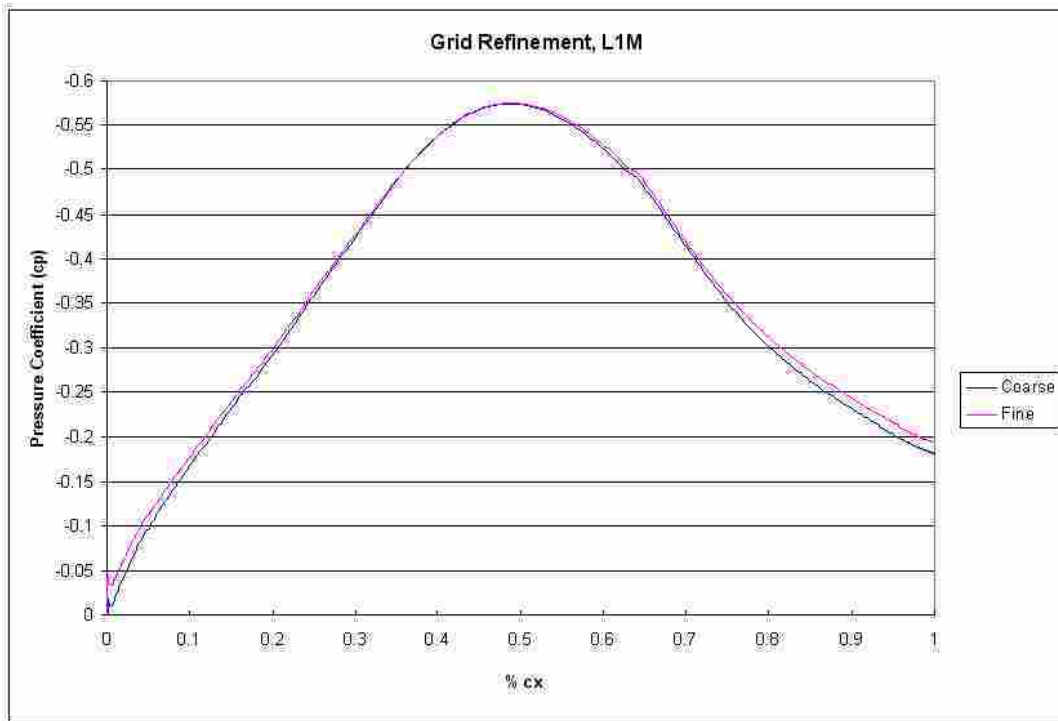


Figure 2.3: Grid refinement study for the L1M blade, showing a coarse and fine mesh c_p distribution.

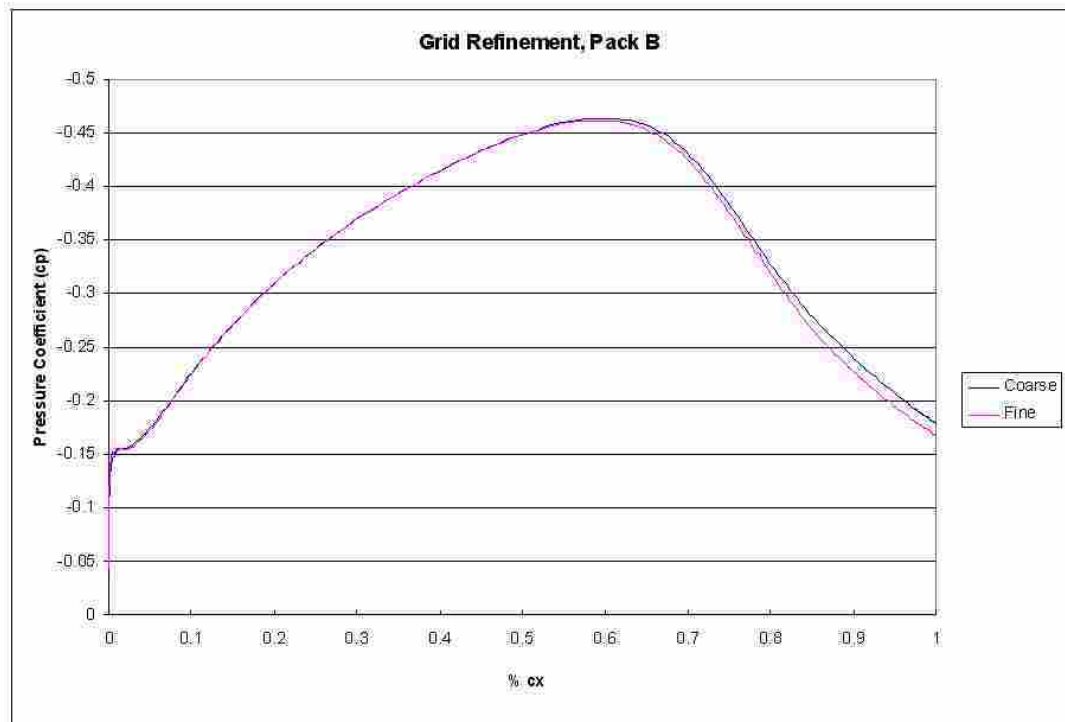


Figure 2.4: Grid refinement study for the Pack B blade, showing a coarse and fine mesh c_p distribution.

2.2 Results-L1M

2.2.1 Laminar Solution

Considering the low Reynolds number and low free stream turbulence levels along with experimentally observed laminar boundary layers, a first attempt was made to model this flow with a simple laminar model. Figure 2.5 shows the stream function of the L1M blade for a steady laminar solution. Note that the assumption of 2D steady flow in the separated regions is not appropriate.

Although the steady equations were solved, a pseudo-unsteady flow field resulted in this region (i.e. a truly converged solution is not obtained). However, the predicted separation points for the Pack B and the L1M blades, as shown in Table 2.1, are found to be in very good agreement with the higher-fidelity simulations of Gross [8] and the experiments of Bons [3]. Additionally, the general trends of separation size in the separation regions were observed to be correct.

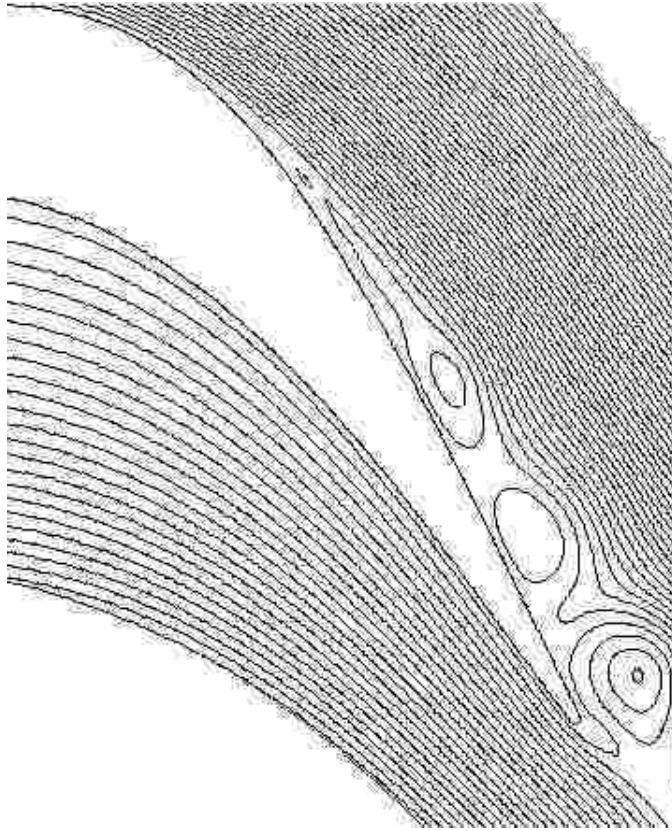


Figure 2.5: Stream function of the laminar solution for the LIM at $Re=20,000$.

Table 2.1: Separation Locations for Various Models and Cases in % Axial Chord

Model	Pack B	L1M	Re	Tu
Fluent	0.73	0.58	20,000	3%
Gross & Fasel [8], [9]	0.73	0.57	25,000	.3%
Bons et al. [12]	0.72	0.59	20,000	3%

Considering that the experimentally observed separation for both the Pack B and LIM blades includes a transition point that reattaches the flow, this model was only accurate for the regime from the leading edge to the separation point, where the modeling of the laminar boundary layer was most appropriate.

2.2.2 Turbulence Model

The experiment of Bons et al. [3] measured a free-stream turbulence level of 3% intensity at the cascade inlet. Based on the 3% inlet turbulence level and the length scale measured by Reimann et al. [12], the turbulent viscosity ratio was calculated to be 64. The free stream turbulence was generated with a square bar grid spaced $5.2 c_x$ upstream of the cascade. Using these parameters, a periodic domain with a shorter inlet length from the experiment to save on computation costs was run using three RANS turbulence models in Fluent; the Spallart-Allmaras, $k - \epsilon$, and $k - \omega$. Neither of these models predicted an accurate flow field compared to the data from Bons et al. [3]. Figure 2.6 shows c_p plots of each turbulent case for the LIM blade. The turbulent models showed no separation at all. The c_p does not show the sudden drop in c_p around $c_x = 0.73$ representing turbulent transition and reattachment. This was because the boundary layer was modeled as turbulent throughout instead of laminar, causing the flow to remain attached throughout the blade passage.

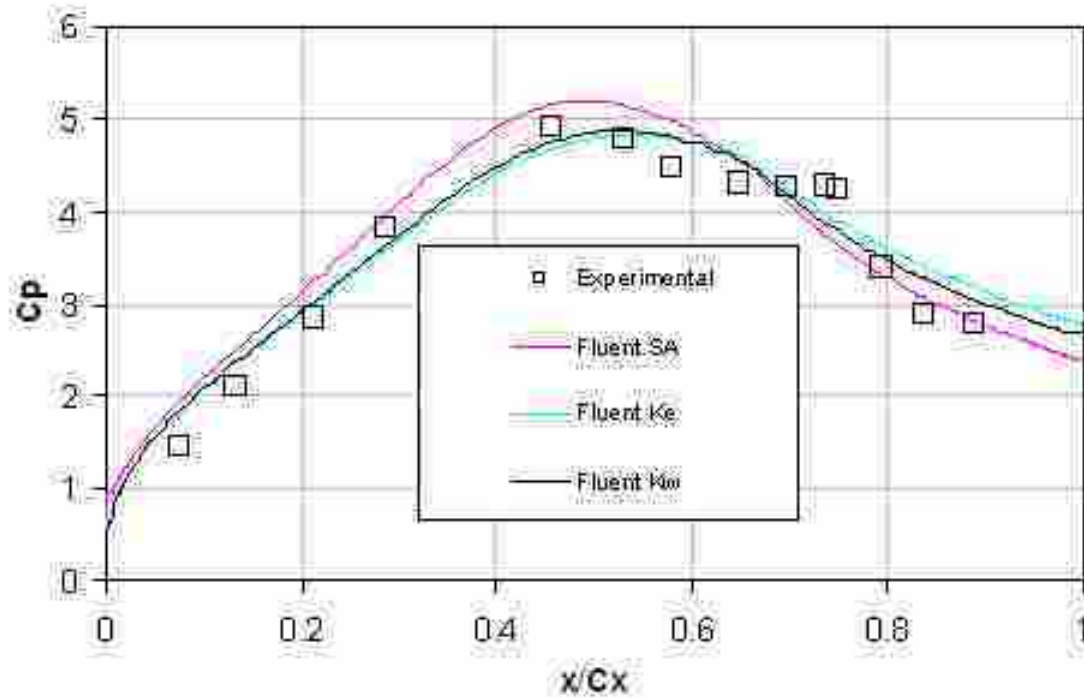


Figure 2.6: Fluent solutions of the LIM cascade using the Spallart-Almaras, $k - \epsilon$, and $k - \omega$ turbulence models compared to data from Bons et al. [3]($Re=20,000$, $Tu=3\%$).

2.2.3 Turbulent Trip

Since fully laminar and fully turbulent simulations did not accurately predict the reattachment of flow on the aft portion of the blade, it was concluded that these models alone could not produce an accurate simulation, but that a method of transitioning between laminar and turbulent flow was necessary. Using the transition point from the experimental data of Bons et al. [3], the domain was split into two regions: a laminar portion upstream of the transition point, and a turbulent portion downstream. Figure 2.7 shows the new domain.

This model also did not predict the correct features of the flow. The separation was not significant. The problem was narrowed down to the geometry of the domain. As can be seen from Figure 2.7, the transition to turbulence was applied to both the suction and pressure surfaces at the same axial location. The now turbulent boundary layer on the pressure surface was larger than the physically correct laminar boundary layer. This pushed the mid-passage flow toward the suction surface causing the separation bubble to completely disappear, even in the laminar zone. This result was somewhat surprising in that it was not expected that the turbulent boundary layer on the pressure surface would have such a strong effect on the overall flow field.

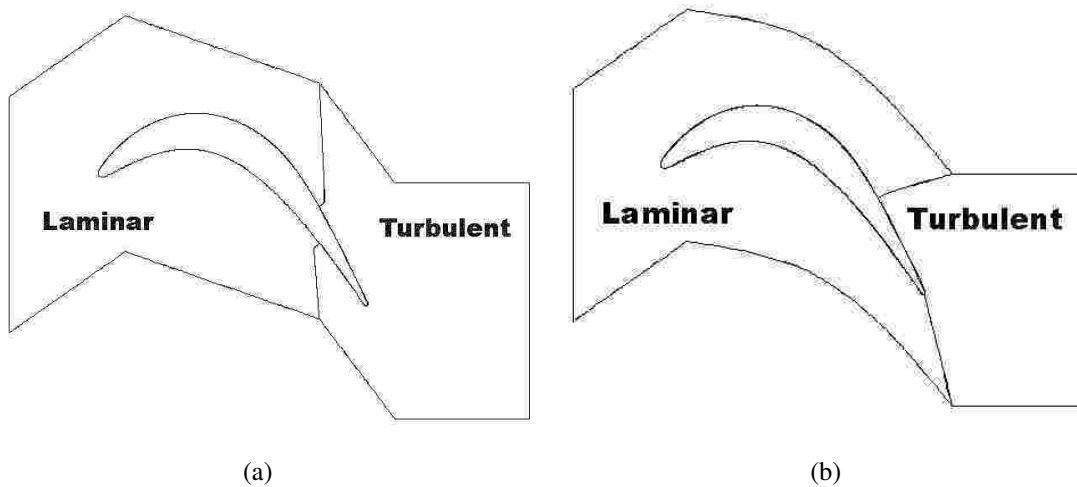


Figure 2.7: The laminar and turbulent zones (a) initial domain, and (b) second attempt .

This was remedied by changing the position of the turbulent zone boundary. The new domain is shown in Figure 2.7. Notice that the turbulent zone on the pressure surface

does not begin until the trailing edge of the blade. This new domain relieved the problem and the CFD data showed the same flow features that were shown in the experimental results of Bons et al. [3]. It must be noted that the trip to turbulence creates an instability at the specified trip location. This is manifested as an oscillation located just before and after the transition location of $c_x = 0.73$ as seen in the c_p data of Figure 2.8. It is believed that the oscillation is caused by a sudden jump in turbulent properties when the domain switches from laminar flow to turbulent. As can be seen from the Figure 2.7, the $k - \omega$ model was more susceptible to this instability than the Spallart-Almaras and the $k - \varepsilon$ models. The susceptibility of the other models may be due to the size of the boundary layer. It can also be seen from Figure 2.9 that the order of solver used also effects the magnitude of the oscillation. The magnitude of the oscillation is much greater for the 2nd order discretization, while the 1st order discretization dampens the oscillation.

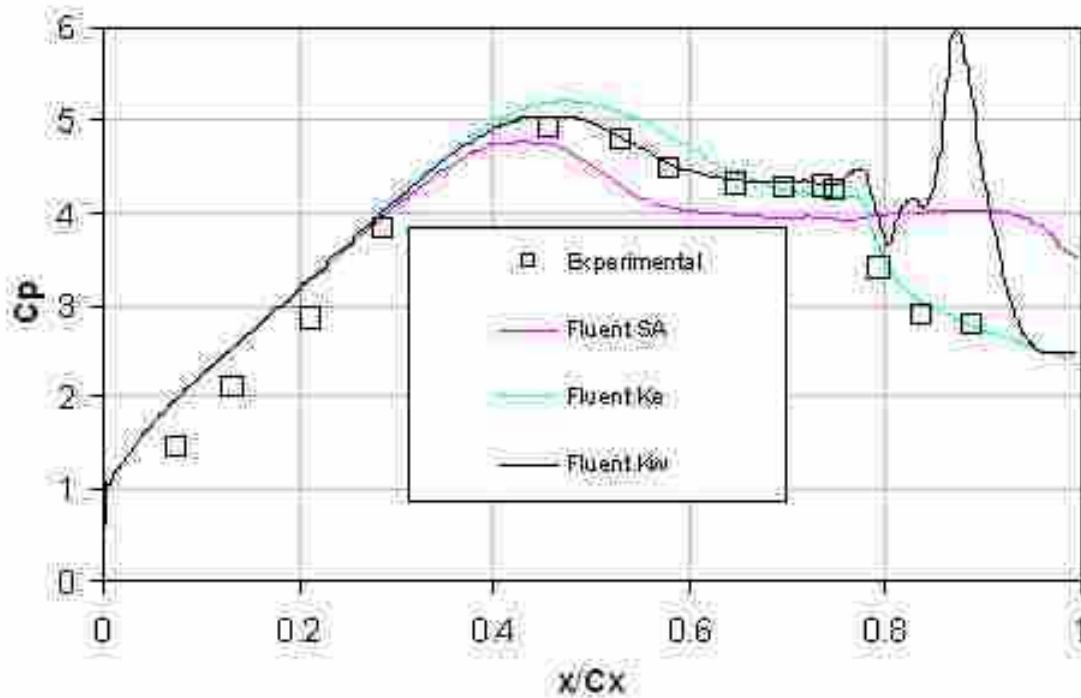


Figure 2.8: The Fluent solutions to the tripped turbulent solutions using the experimental transition data and the Spallart Almaras, $k - \varepsilon$, and $k - \omega$ turbulence models, compared to the experimental data of Bons et al. [12] for the LIM blade at $Re=20,000$.

The desired outcome of these simulations was to match the experimental observations of a separated boundary layer that reattaches at some point downstream. The $k - \epsilon$ and Spallart-Almaras models do show a separation and reattachment, however, compared to the experimental data the size of the separation is much smaller. It was determined that the placement of the turbulent trip has an effect on this unstable behavior. This will also be observed in the discussion of a predictive model for transition in Section 2.2.4.

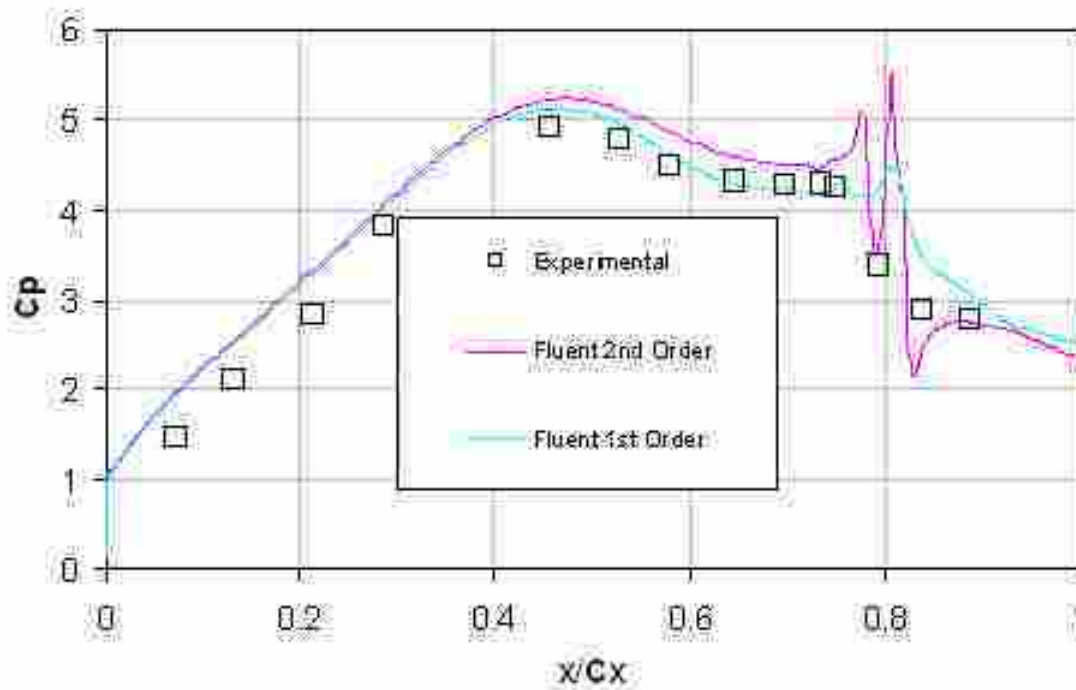


Figure 2.9: The Fluent solutions to the 1st and 2nd order tripped turbulent solutions using the experimental transition data and the $k - \omega$ turbulence model, compared to the experimental data [12] for the L1M blade at $Re=20,000$.

2.2.4 Transition Models

It is not always practical to run an experiment just to find out where the transition to turbulence occurs so that CFD will be able to predict the flow field. Bons et al. [3], [6] compared their experimental transition location for the L1M with a transition model by Praisner and Clark [14] and found that the difference between experiment and the model was 9%. This model was also used to predict the transition location for the L1M model in

the current Fluent study. The form of the model is:

$$\frac{L}{S_{sep}} = CRe_{\theta_{sep}}^D \quad (2.1)$$

where $C = 173.0$, $D = -1.227$, L is the distance between separation and the location of transition, and S_{sep} is the surface distance between the leading edge of the blade where stagnation occurs and the location of separation. $Re_{\theta_{sep}}$ is the momentum thickness Reynolds number at the location of separation. The model used the separation location and boundary layer parameters from the laminar solution, seen in Figure 2.5, to solve for the location of transition. Table 2.2 shows the difference between experimental results and the Praisner and Clark [14] model for both the Pack B and L1M. These values were used in the CFD models and a comparison was made.

Table 2.2: Transition Locations for the Pack B and L1M blades in % Axial Chord

Transition Location	Pack B	L1M
Praisner & Clark [14]	0.87	0.82
Bons et al. (Experiment) [3], [12]	0.84	0.73

Figure 2.10 shows the simulation results when the transition is placed at the predicted value of Praisner and Clark [14]. The figure shows that the same general accuracy of the models before transition matches that of the previous solution. But, the magnitude of the oscillation at the transition location was greatly increased, and was also present with the other two turbulence models. This implies that the position of the transition location makes a significant difference in the stability of the solution. The Praisner and Clark [14] transition locations are further downstream compared to the experimental. It is possible that the boundary layer separation grows too big before the the turbulent transition can reattach the flow as observed in the experiment. More studies should be done to more accurately define the source of this instability.

Figure 2.11 shows the velocity magnitude contour plot for the L1M blade with the more accurate two zone domain. This matches well with the experimental data provided by Bons et al. [3].

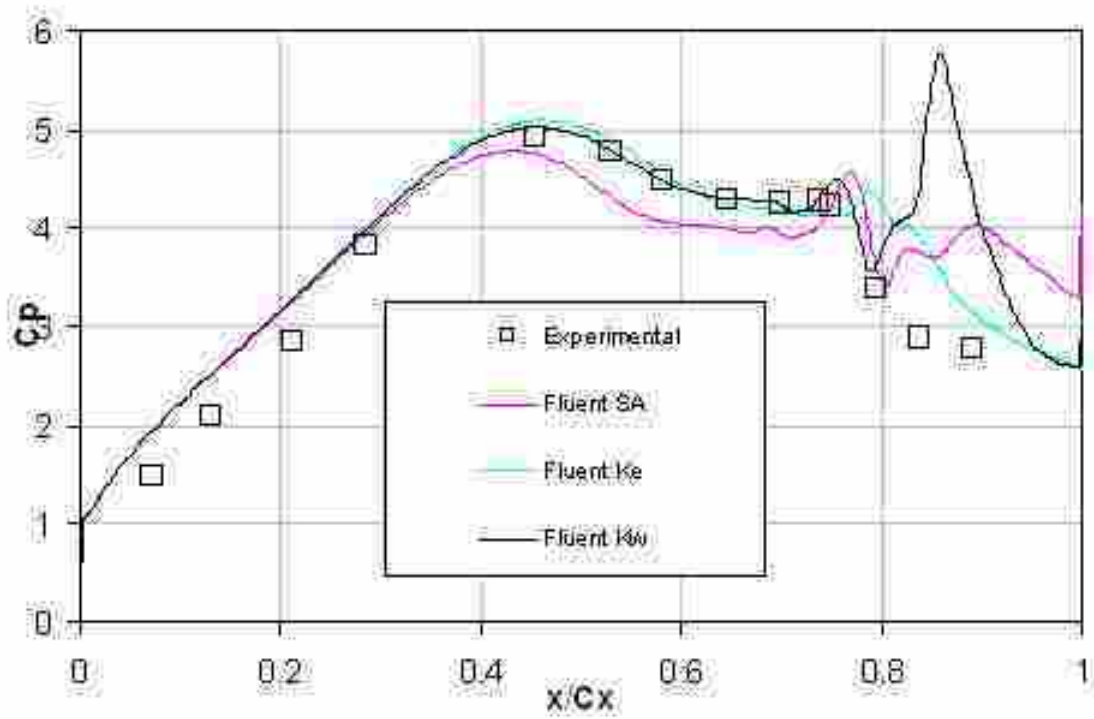


Figure 2.10: The Fluent solutions to the tripped turbulent solutions using the Praisner and Clark [14] transition data, compared to the experimental data for the L1M blade.

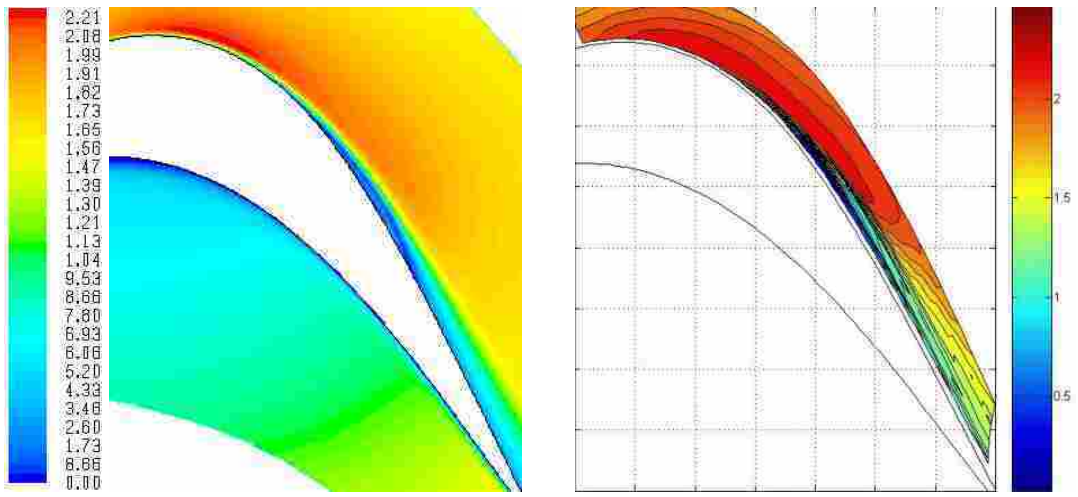


Figure 2.11: Left, computational contour plot using the $k - \epsilon$ turbulence model and $Re=20,000$, right, experimental contour plot of velocity magnitude for the L1M blade (Note: the color scales are not exactly the same).

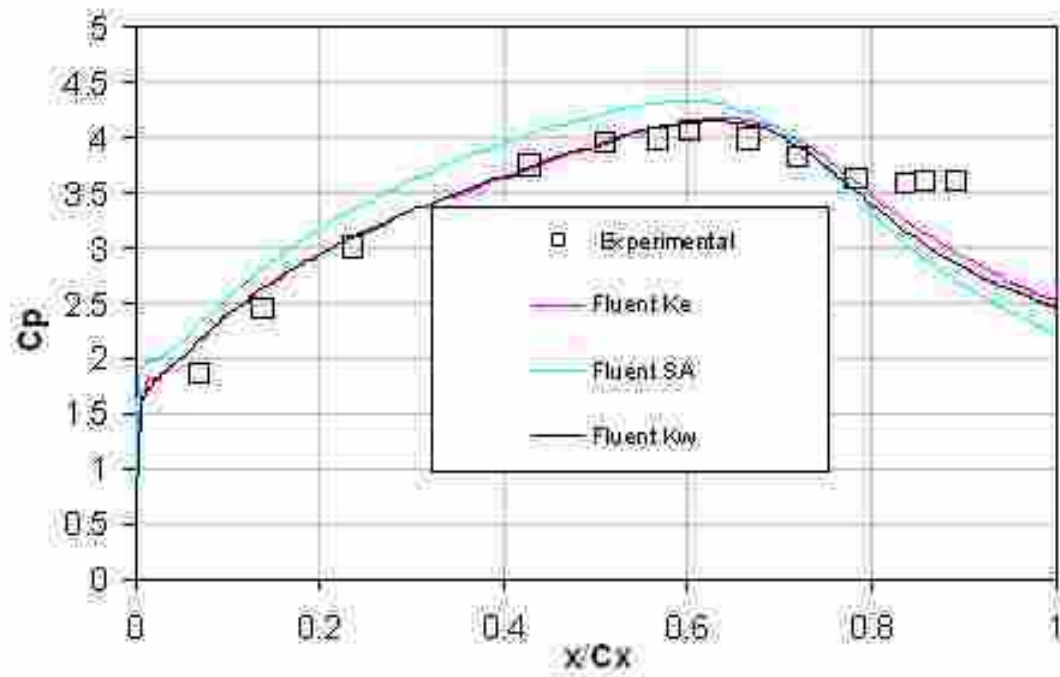


Figure 2.12: The Fluent solutions to the non-tripping turbulent solutions using Spallart Almaras, $k - \epsilon$, and $k - \omega$ models, compared to the experimental data [3] for the Pack B blade at $Re=20,000$.

2.3 Results-Pack B

2.3.1 Pack B Application

The same process as outlined above was used on the Pack B turbine blade at $Re=20,000$. Figure 2.12 shows the prediction from the pure turbulent simulation. The Spallart-Almaras model tends to over estimate the pressure coefficient. The plot also shows that there was no separation region. Just as the LIM, turbulence models without a laminar zone did not accurately predict the flow field.

The Praisner and Clark [14] transition and the experimental transition models showed the same trends for the Pack B as they did for the LIM (see Figure 2.13). The oscillation still exists and it's magnitude increased for the Praisner and Clark [14] model. This implies that the distance downstream was a factor in the occurrence of the instability. However, unlike the LIM, the instability only occurred in the $k - \omega$ model. The boundary layer sep-

aration characteristics of the other two models for the Pack B were the same as the LIM. The separation was not significant.

2.4 Conclusions from CFD Model Development

Modeling low Reynolds number turbine blades is fraught with challenges that are not easily remedied. A relatively simple method has been presented, although, not without its own obstacles and weaknesses. This method, in short, consists of using a laminar solver to predict the separation location on the blade and the other quantities that are used in Praisner and Clark's [14] turbulence transition model. From this information, the transition location is found and the new domain can be built. The model can then be solved using the most parsimonious method. In the case presented here, this would be the 1st order discretization, with a single equation turbulence model. If the instability still occurs, then it would be advantageous to shift the transition location forward. However, a more thorough investigation of the cause of the instability still needs to be completed.

A new method of solving transition flows, the $k - kl - \omega$ model, has recently been included in a developmental beta version of Fluent, after the development of the presented method. The new $k - kl - \omega$ method could greatly simplify the process if it is found to sufficiently predict LPT flows.

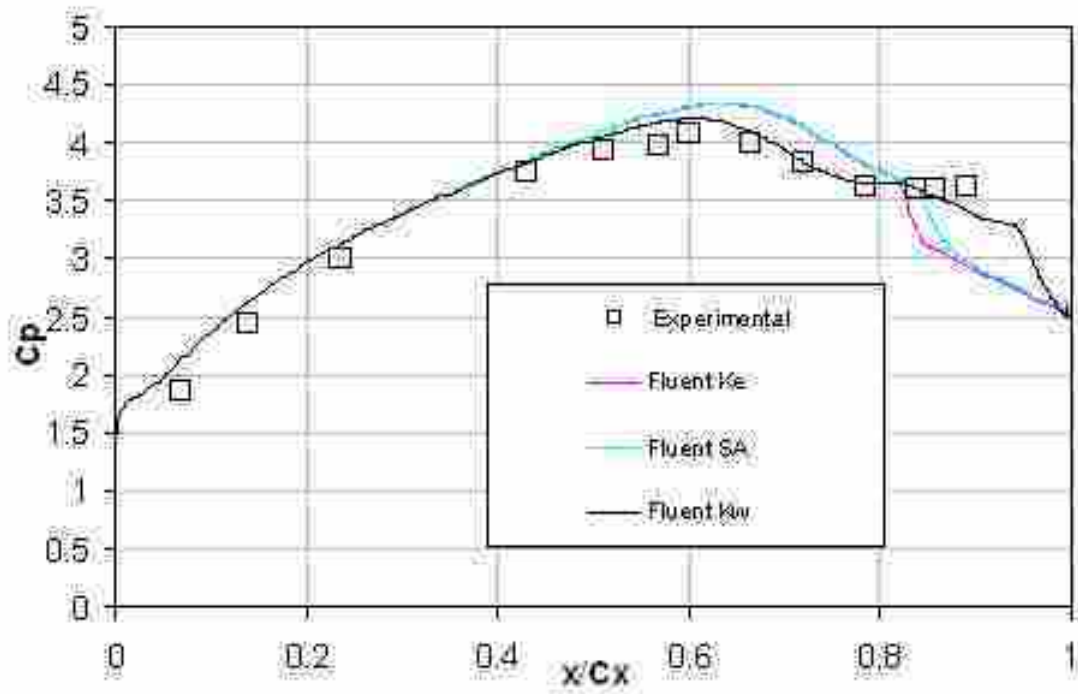
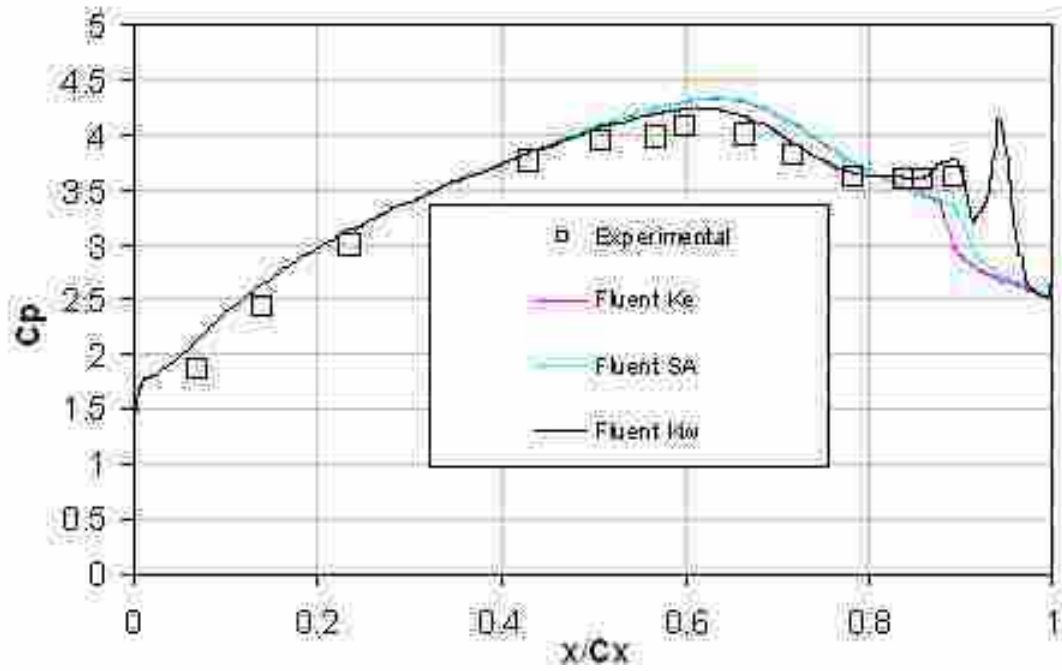


Figure 2.13: The Fluent solutions to the tripped turbulent solutions using Praisner and Clark's [14] (top) method of predicting transition and the experimental values for transition (bottom) compared to the experimental data [3] for the Pack B blade at $Re=20,000$.

Chapter 3

Mesh Manipulation

The design of a wind tunnel significantly affects the success of the experiments performed in the wind tunnel. If the tunnel is designed for one type of experiment it may not be good for another type. Current tunnel configurations may not be the best designs and could introduce extra error in the experiment in the form of boundary layer effects and a lack of periodicity. Types of experiments that include boundary layer suction and a manipulation of tailboards are not ideal. Suction of the boundary layer requires knowledge of the amount of mass evacuated from the tunnel which is hard to measure. Tailboard movement is not exact and could introduce variation from moving the tailboard multiple times. Hence, a tunnel geometry that could remove these inconsistencies is desirable. The geometries for this experiment are described in this chapter, as well as the effect certain aspects of the geometry have on the flow field.

3.1 Original Experimental Configuration

The wind tunnel configuration used to make the computational and experimental comparisons is partially described by Eldredge et al. [15]. The tunnel is an open loop facility driven by a centrifugal fan with an output capacity of 3 kg/s. After the flow leaves the blower it enters a heat exchanger with adjustable heating and cooling elements capable of maintaining constant air temperatures. The tunnel after the heat exchanger is shown in Figure 3.1. The flow then passes through 9m of 0.67m diameter ducting before expanding to 1.83m of 1.07m diameter conditioning plenum. At this point the flow has low turbulence and is uniform in nature and enters 1.83m of 0.381m wide square ducting before entering the test section. Prior to the test section a square grid turbulence generator is placed $5c_x$ upstream of the cascade inlet to define the turbulent intensity of the flow. The turbulence

generator produced a turbulence intensity level of 3%, which has been shown to be a typical free stream intensity level for low Reynolds number flows [12].

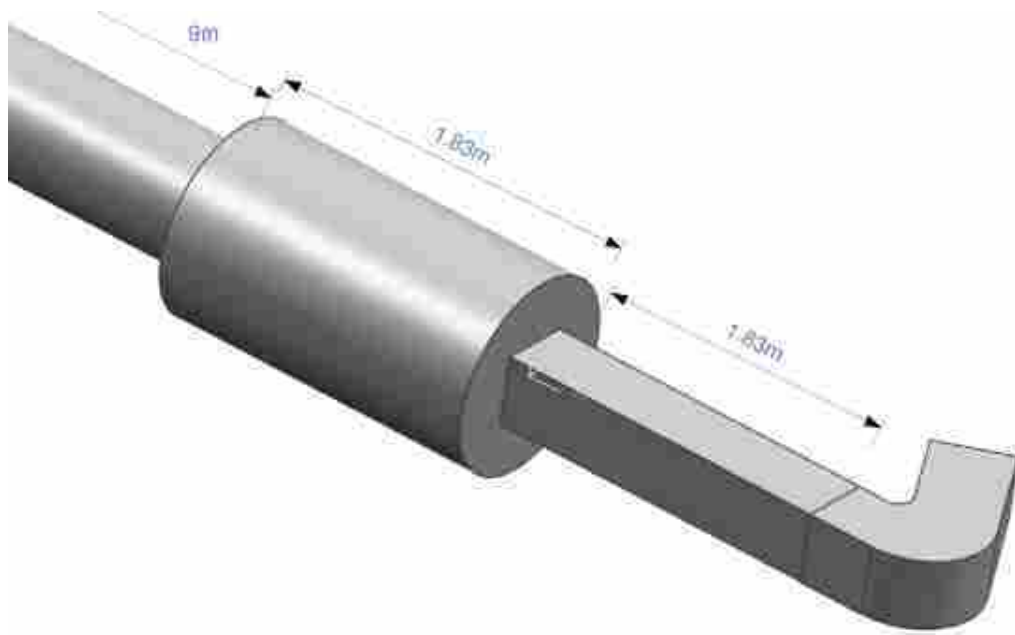


Figure 3.1: Original experimental tunnel configuration showing the last portion of the 9m section to the outlet of the test section.

Eldredge et al. [15] found that the modular design of the wind tunnel allows for only the test section to be adjusted. It is the geometry of this test section that is the focus of this research. It was decided that the test section would consist of three passages, requiring the manufacture of two identical blades and two wall sections to be determined from the numerical work. A sample test section geometry can be seen in Figure 3.2. This geometry is the original used by Eldredge et al. [15].

3.1.1 Experimental Methods of c_p Matching

The original experimental test section, shown in Figure 1.6 and 3.2, was a dual passage design with a single blade placed in the center of the tunnel. The tunnel walls were based on the blades suction (top wall) and pressure (bottom wall) surfaces. The spacing between the blade and the walls was determined from the design solidity of blade. This configuration required that something be done with the boundary layer developed along the

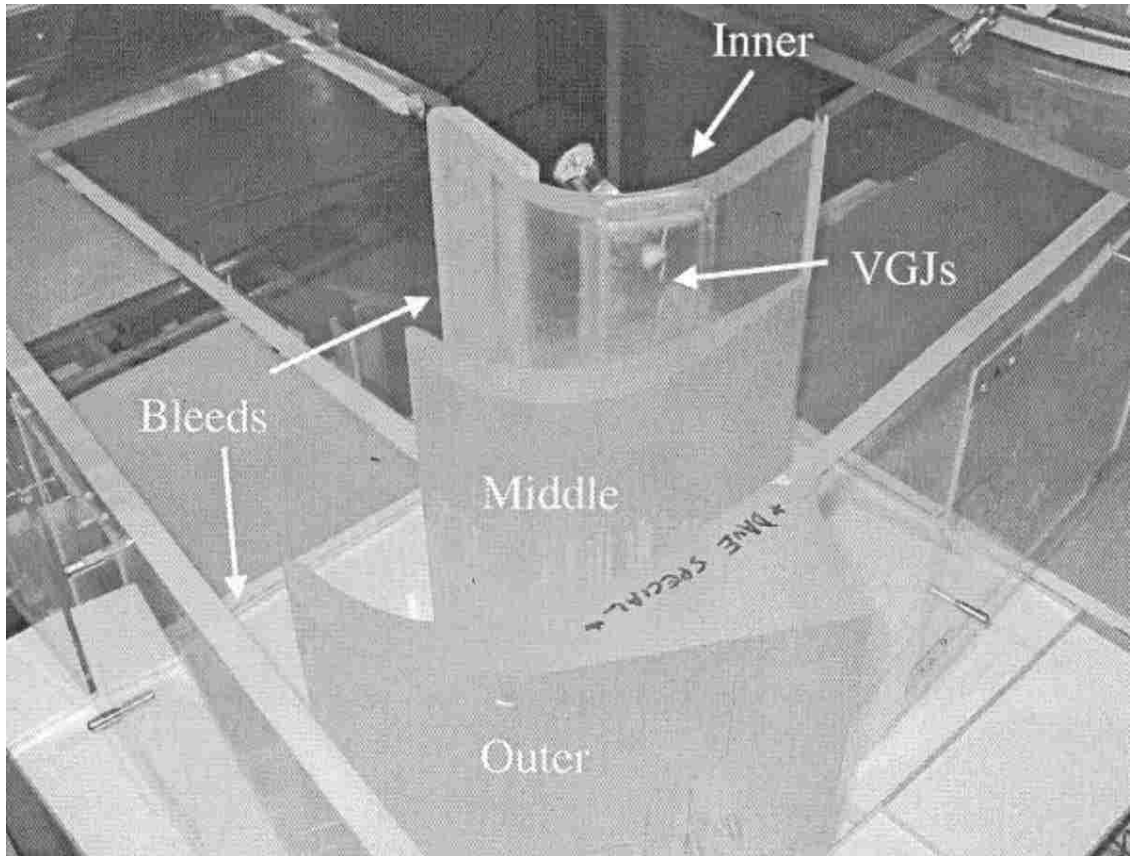


Figure 3.2: Original experimental tunnel test section configuration [15].

1.83m section of square ducting. To remove the boundary layer a bleed on both walls was placed just in front of the curved sections. The exact amount of air bled was undetermined due to the inability to measure it. This removal of mass from the flow also has an effect on the Reynolds number of the flow at the inlet plane of the blades. A tail board was also made to adjust the c_p distribution. By altering the size of the bleed and the position of the tail boards it was possible to match the c_p of the dual passage test section to the c_p distribution that was found using an eight blade cascade.

3.2 New Test Section Configuration

A new three-passage experimental test section was designed to allow the tunnel end walls to be manipulated through optimization runs. This was done by slightly reducing the size of the blades so that the spacing between end walls and blades was 9.9% larger. The magnitude of this change was based on an estimation of the boundary layer thickness of

the flow entering the test section. The estimation was based on previous boundary layer experiments using the same tunnel of Bons et al. [15]. By changing the blades, the rest of the tunnel did not need to change. So at the end of the 1.83 square duct of the tunnel as described previously, only the test section was adjusted.

The test section consisted of two L1A blades placed in the center of the test section. The L1A is another research design blade by the Air Force Research Laboratory. The L1A is a modification of the L1M, designed to move the maximum lift to the aft portion of the blade. The correct spacing between the blades was maintained based on the design solidity for the L1A blade of $\sigma = 0.99$. The dimensions of the tunnel walls were left to be determined from the optimization runs. The end wall geometry for the initial computations was the same as the blade surfaces, but shifted to match the tunnel inlet width of $2.655c_x$. The domain extended $1.6 c_x$ upstream of the leading edge of blade 2 and $2.2 c_x$ upstream of the leading edge of blade 3. The domain extends at least $3.3 c_x$ downstream from the trailing edge of the blades. The nozzle extends $0.42c_x$ upstream in the horizontal direction. Figure 3.3 shows the initial domain.

Near the blade, a structured quad mesh was generated to capture the boundary layer as shown in Figure 3.4. This boundary layer mesh had a spacing of $h/c_x = .0005$ for the first node off the wall, and extended approximately $h/c_x = .0158$ from the wall, with a growth rate of 1.1. Outside the boundary mesh, unstructured triangles were used to mesh the remainder of the domain. Approximately 330 nodes were used along the upper and lower blade surfaces. In total, approximately 350,000 cells were used in the mesh. This mesh is an extension of the mesh created in Chapter 2, and uses the same boundary layer parameters and growth rates. The results of a grid refinement study were used to prove the grid configuration was sufficient and are shown in Figure 2.3 and 2.4.

3.2.1 Model Definition

The details of the numerical methods used to solve the problem are the same as specified in Chapter 2. A two dimensional computational model was created for simplicity and speed of calculation. 3D effects should be minimal as the wind tunnel was created to simulate a two dimensional flow field [15]. The domain was bounded by end walls with the no-slip condition applied. The blades also used the no slip condition. The domain

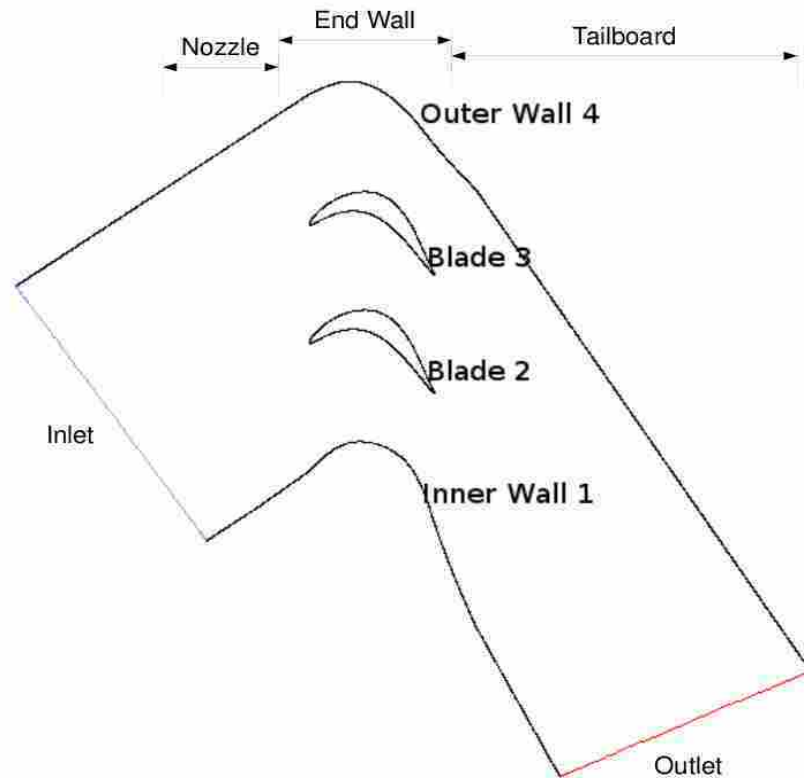


Figure 3.3: The computational domain based on the geometry of the original wind tunnel.

outlet was defined to be an outflow boundary. Because the model only extends a couple chords upstream the inlet conditions require a boundary layer profile along the inlet. The boundary was defined as a velocity inlet and a velocity profile of the boundary layer was used as the inlet velocity. The velocity profile was obtained from a numerical simulation of a 1.83m by .381m two dimensional duct, with inlet conditions of a uniform velocity and the blades design Reynolds number of 20,000. The uniform velocity profile was used to best match the experimental tunnel at the location just after the conditioning plenum where the flow should be uniform. The $k - \epsilon$ turbulence model was used to solve the turbulent characteristics of the flow. Also included in the inlet conditions of the test section were an inlet free stream turbulence intensity level of 3%, and a turbulent viscosity ratio of 64 to match the experimental turbulence characteristics produced by the generator [12].

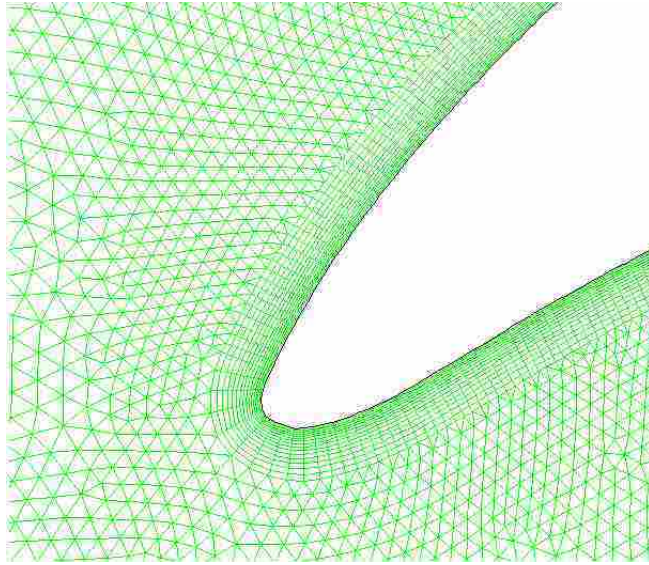


Figure 3.4: Structured boundary layer mesh transitioning to unstructured triangular grid.

3.3 Parametric Study of Design Variables

To produce a good design of the end wall geometry of the tunnel, it was important to understand what effects different geometrical parameters have on the flow field. This knowledge is needed to make important design decisions and when using an optimization technique to generate a feasible periodic solution. The main geometric factors that can be changed to influence the flow field, outside of changing the blade geometry, are solidity, inlet conditions and outlet geometry. In this case, end wall geometry could also be changed. To define the basic guidelines only the solidity (distance between the wall and the blade surface), inlet geometry and outlet geometry were changed. The curvature of the wall directly above and below the blades was constant and identical to the pressure surface and suction surface of the blades respectively.

3.3.1 The Variables

The first variable examined was solidity. More specifically for this case, the distance from the end walls to the nearest blade. The spacing between blades was fixed and did not change. The inlet tunnel width was also fixed and therefore the spacing must be changed between the end of the tunnel and inlet of the test section. This was done by placing a nozzle at the entrance of the test section. Figure 3.5 shows the three domains used to test

how this spacing affects the flow field, and more specifically the c_p distribution. The design spacing is the center configuration. The other spacings are 10% larger and 9% smaller than design.

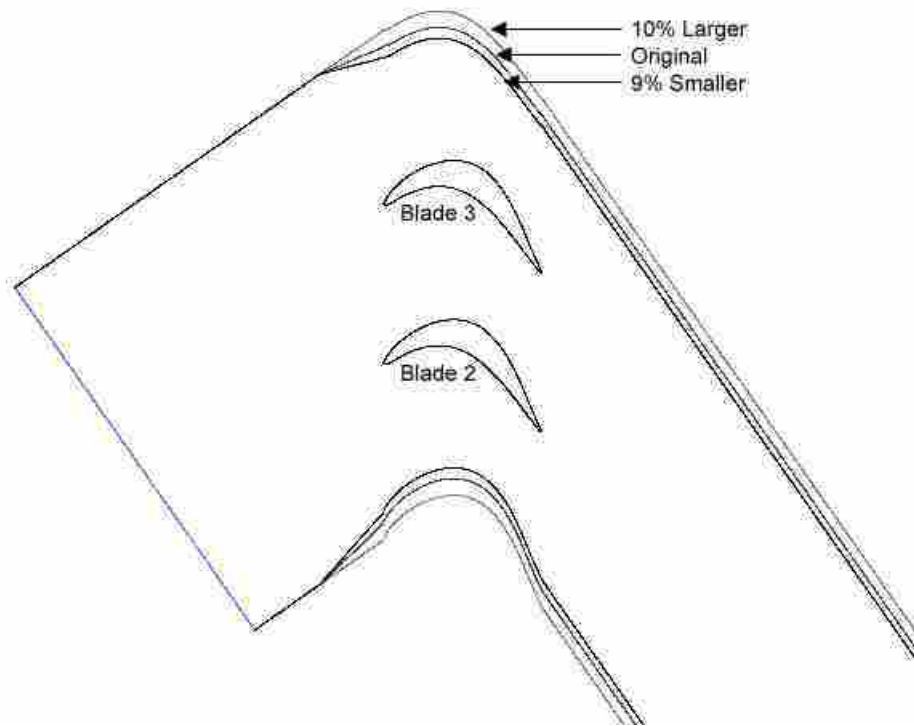


Figure 3.5: Changes in spacing between the walls and the blades for three cases, 9% smaller than design, design spacing, and 10% larger than design.

The second variable is the tail board. The tail board section begins just after the trailing edge of the blades and extend to the outflow boundary. This section could be moved into the flow field to create a nozzle or out of the flow to create a diffuser. The tail board was shifted for all cases of wall spacing, as shown in Figure 3.6. The change was rapid at trailing edge location and transitioned to a more gradual diffusion. This was done to make the top end wall more like a true periodic case where the end of the blade results in an instantaneous expansion.

The third variable is shifting the blades. The blades were shifted up and forward in the domain, maintaining the spacing between the blades as well as the spacing between blade 3 and the top wall. By shifting the blades forward it was expected that the location

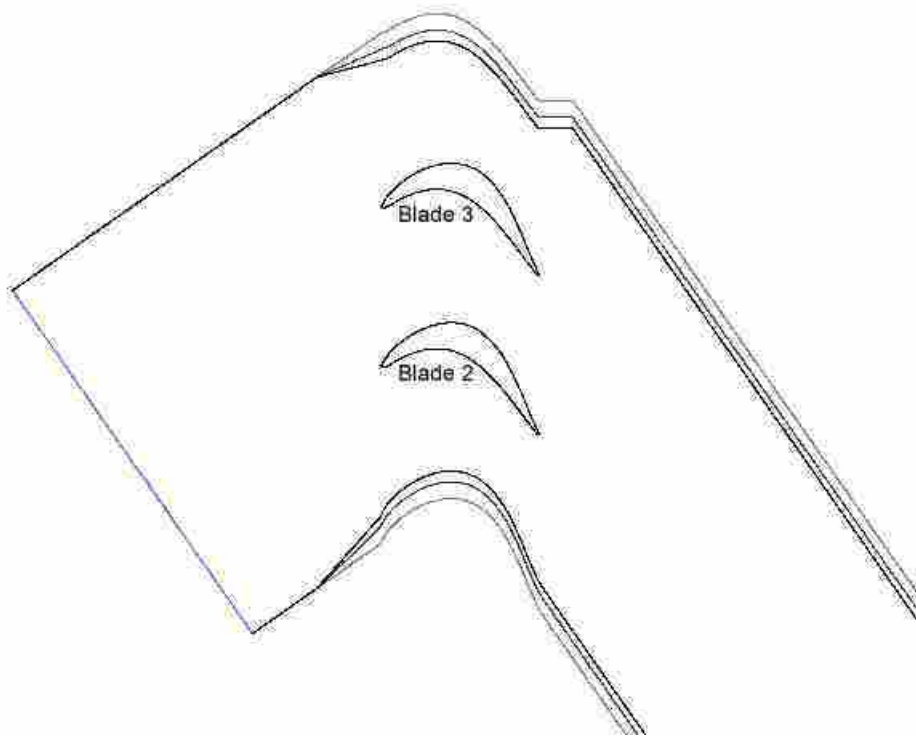


Figure 3.6: Tail boards shifted out for each case of pitch.

of the peak c_p on the blades would be pushed forward. The shifting up was expected to have a similar effect to changing the end wall spacing in that decreasing the spacing would increase the peak c_p of blade 3, while maintaining the magnitude of the c_p for the lower blade 2. Figure 3.7 shows the shifted blades compared to the original domain. The spacing between the top blade and the straight portion of the wind tunnel has decreased, making the tunnel wall boundary layer closer to blade 3. This decreased distance between blade and boundary layer plays a significant role on the blade c_p .

3.3.2 Parametric Study

The effect of wall spacing on the c_p distribution can be seen from Figure 3.8. In general, the smaller spacing caused a higher magnitude of c_p . Interestingly, the suction surface c_p of blade 2 also increased even though the spacing between the blades was not changed. This indicates that the Reynolds number at the inlet plane of the blade changes depending on the wall spacing, which is influenced by the nozzles upstream. For the cases

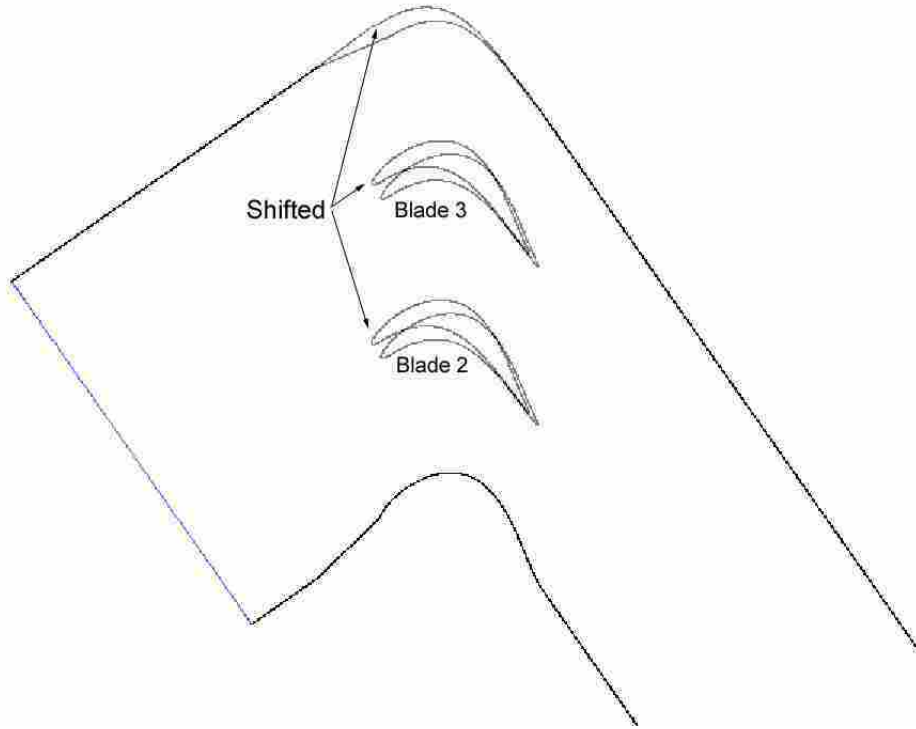


Figure 3.7: Blades shifted up and forward compared to the original domain.

of smaller wall spacing the Reynolds number increases, making the c_p increase. The case of a larger wall spacing has the smallest magnitude of c_p .

In all simulations except the original, the location of peak c_p of blade 3 was farther downstream than for blade 2. The location of the peak moved farther downstream as the wall spacing decreased. It was also noticed that the peak c_p location for blade 2 was the same for all the cases, indicating that the velocity changes created by diffusion and the inlet nozzle did not effect the maximum c_p location. Therefore, variables that altered the location of the peak c_p were the blade inlet plane flow angle, which can be altered by the inlet nozzle, and the wall boundary layer.

Figures 3.9 - 3.11 shows the suction surface c_p distributions of the shifted tail board runs. The plots show that the shifted tail boards reduced the magnitude of the pressure coefficient significantly. This was done by diffusing the exit flow which reduced the velocity. It also shows that the peak c_p of blade 2 did not shift significantly. However, the peak c_p of blade 3 shifted substantially forward for the case of increased wall spacing. The forward shift of the peak can also be attributed to the diffusing nature of the tailboard, increasing

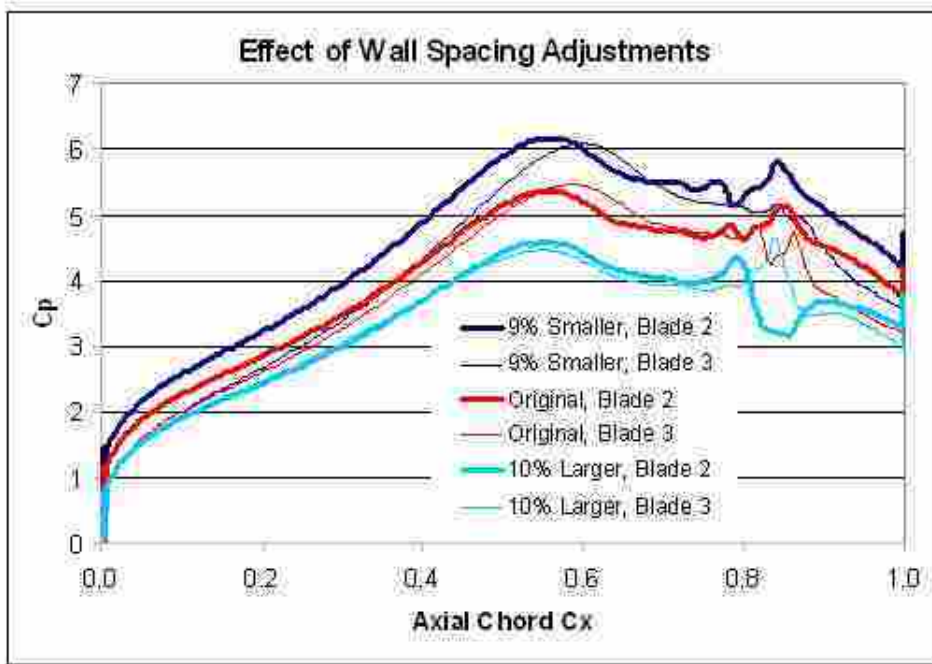


Figure 3.8: Comparisons of the c_p distribution for variations in wall spacing.

the incoming velocity angle. An increased velocity angle results in the forward shift of the maximum c_p location. The lower c_p created from the diffusion rolls the peak down the existing c_p curve, moving the peak to a more forward position.

The shifting of the blades inside the tunnel domain created three significant changes to the c_p distribution. These changes can be seen in Figure 3.12. The peak c_p increased for both blades, only the location of the peak c_p for blade 2 shifted, and the oscillations that were discussed in Chapter 2 are much smaller. The increase in c_p shows that the velocity of the flow increased. This increased velocity also reduced the oscillation or unsteadiness of the flow. Because the blades were shifted, the spacing between the boundary layer on the interior wall and blade 2 also increased. This increase reduced the effect of the boundary layer on the flow and a more uniform flow entered the blade passage, thus moving the location of peak c_p to better match blade 3.

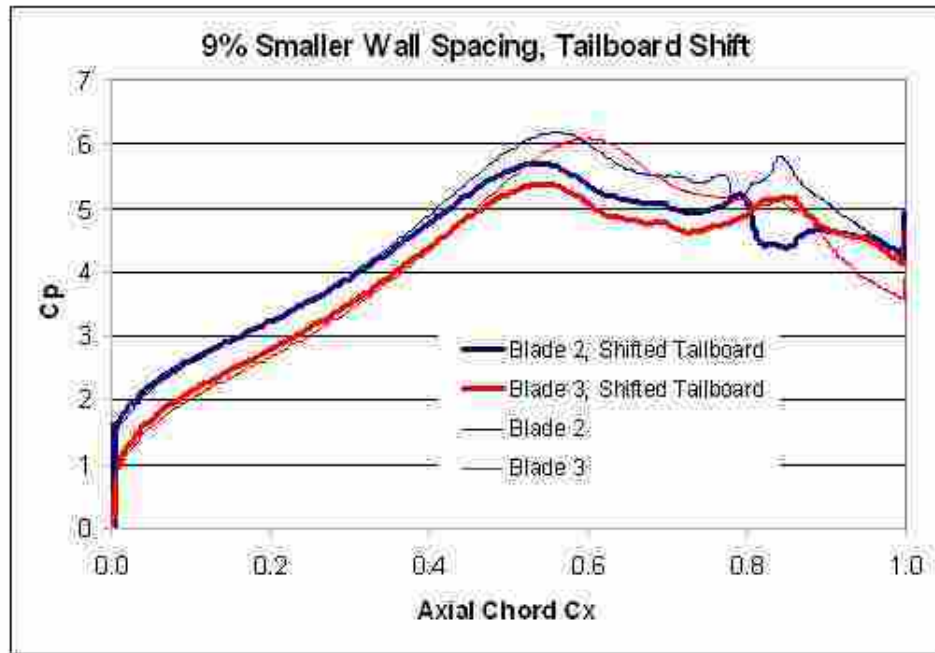


Figure 3.9: Comparisons of tail board shift compared to original configuration for the smaller wall spacing.

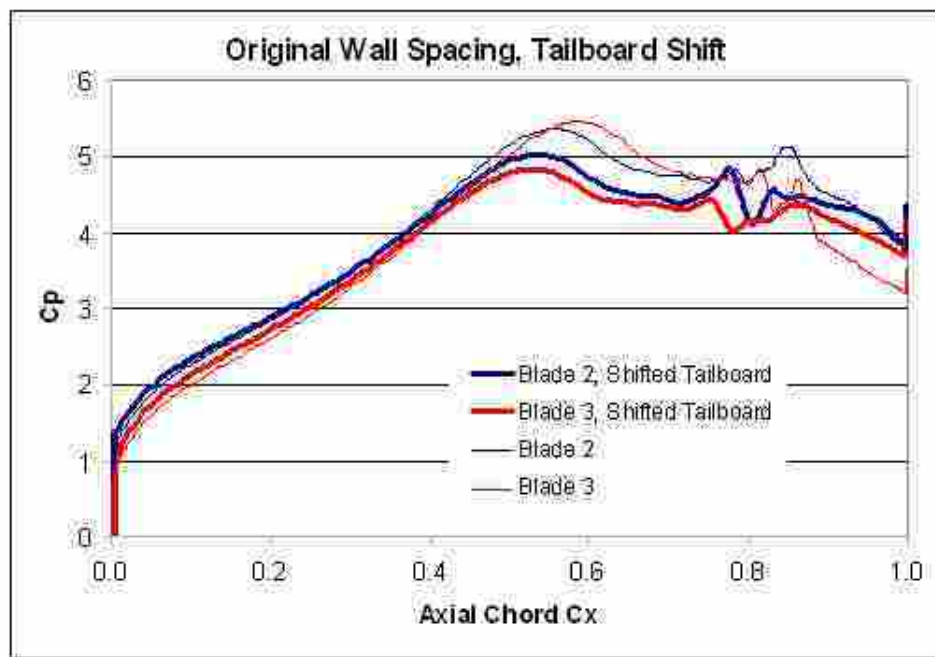


Figure 3.10: Comparisons of tail board shift compared to original configuration for the original wall spacing.

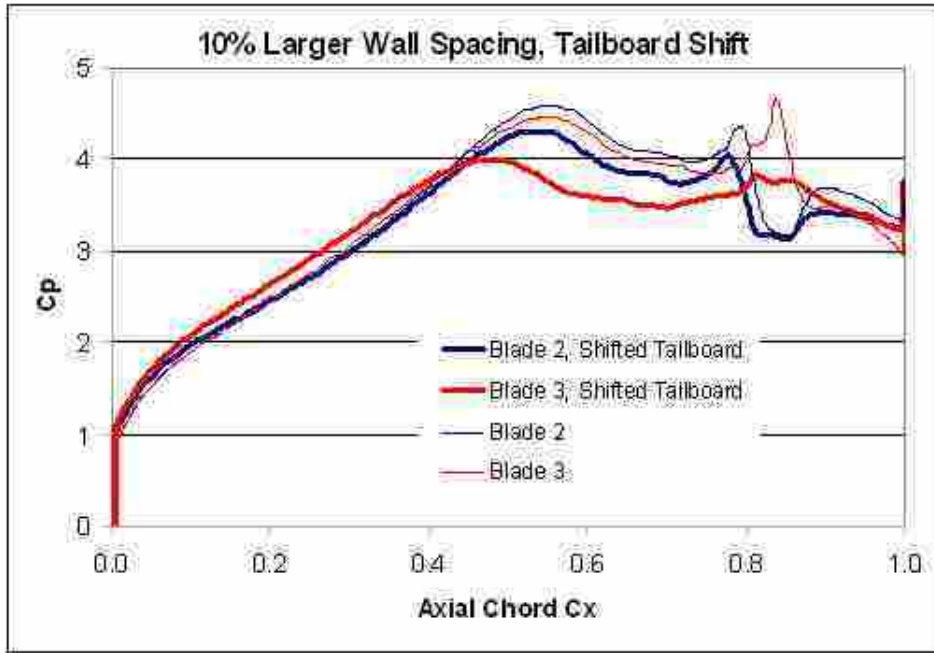


Figure 3.11: Comparisons of tail board shift compared to original configuration for the larger wall spacing.

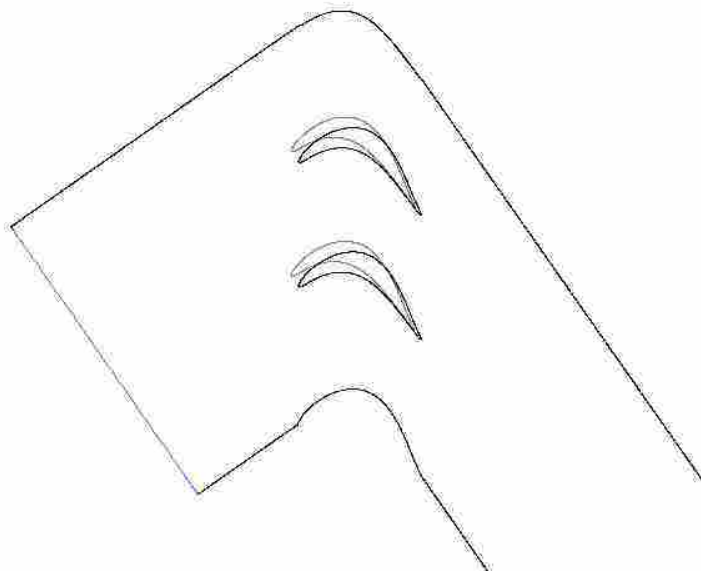


Figure 3.12: Comparisons of c_p for shifted blade compared to original configuration.

3.4 Summary

Based on this parametric analysis, basic rules can be created to improve the optimization process used to define the wind tunnel geometry. The domain changes should be considered when designing the computational experiment. In general, a wider tunnel will decrease the magnitude of the peak c_p , while the narrow tunnel will increase it. Increased diffusion from the trailing edge of the blades to the outlet also decreased the maximum c_p . A sudden diffusion, like the models shown in Figure 3.6, did improve periodicity between the 2 blades in the tunnel. Shifting of the maximum c_p location is considered to be due to flow direction and wall geometry. A forward shift indicated an increased velocity angle, and rearward shifts indicated a decreased velocity angle. The only way for the location of maximum c_p to change for blade 2 was to alter the inlet flow angle due to the wall boundary layer effects and the nozzle portion of the tunnel, turning the flow. Blade 3 maximum c_p could change due to changing the end wall geometry as well. Thus, the c_p distribution of blade 3 was easier to move than blade 2.

Chapter 4

Optimization

4.1 Introduction

The objective of this study was to create a periodic linear cascade by optimizing the end wall geometry using CFD. Optimization techniques have successfully been used to design airfoils and turbine blades. These optimizations were highly non-linear with computationally expensive objective functions and many constraints [16]. Ray et al. [16] discussed the ability of using a swarm algorithm capable of handling single- and multi-objective airfoils. The swarm algorithm was also able to handle constrained and unconstrained problems. The algorithm uses a simulation of social behavior to communicate to each flier in the swarm what adjustments are being made, so that each flier can adjust accordingly. This algorithm was used in accordance with a PARSEC geometry representation and euler solver to compute the flow around the airfoil. A known airfoil c_p distribution was used as the design goal. The objective function used was $f = \sum_{i=1}^M (c_{pi} - c_{pi}^T)^2$ where c_{pi} is the pressure coefficient at the i th location of the airfoil and c_{pi}^T is the target pressure coefficient at the i th location. The optimization resulted in a decrease of f from 2.567 to 0.0737. Another inverse design optimization performed by Ashihara and Goto [17] used an objective of performance efficiency to define the characteristics of 3D pump impellers. The design variables were the blade loading parameters and the 3D grid consisted of 500,000 cells, which was a borderline minimum acceptable grid size to reduce computation time. The flow field was solved using a Dawes code for incompressible flows and Baldwin-Lomax turbulence model. Four optimization algorithms were used to maximize the efficiency, Sequential Linear Programming, Exterior Penalty, Simulated Annealing, and Genetic Algorithm. Each optimization method resulted in a efficiency increase of about 2%.

To design the desired wind tunnel so that manual suction and tail board movement was not needed, as discussed in Chapter 3, to match the flow fields of the theoretical periodic predictions, the tunnel walls were iteratively manipulated until an optimal solution was produced. Recent studies by Laskowski et al. [10] have shown the successful application of optimization techniques in solving the wall boundary geometry of an experimental wind tunnel with turbine blades for a transonic flow. Laskowski's application was based on computational fluid dynamics (CFD) using a RANS $k - \epsilon$ model, and an iterative approach to solve for the tunnel walls. The initial wall geometry chosen by Laskowski was a streamline extracted from an infinite cascade simulation. This initial geometry was then altered until the 2D CFD simulations predicted the desired surface isentropic Mach number (SIMN). The solution was then modified using the separating streamline (due to a separation on the upper end wall) as the end wall. This domain was then built and tested in an experiment. Laskowski et al. [10] continued to improve their design by inserting a shear stress penalty on the end wall to avoid the recirculation zone. The main difference for this research was the extension of the idea to low Reynolds number flows, which as discussed in Chapter 2, introduces different physical characteristics and challenges. The experimental validation of the optimized tunnel domain will be conducted by another research group.

The experimental facility was designed to account for the boundary layer created along the walls of the the wind tunnel. To accomplish this the spacing between the blade and the wall simply increased instead of using the actual blade row solidity. This was done by decreasing the size of the blades, making the needed width for the dual blade configuration smaller. By changing the blade size, the original tunnel was able to be used thus avoiding a tunnel rebuild. The amount of space added was $9.9\%c_x$, which was based on an estimate of the size of boundary layer at the inlet plane of the blades. The baseline geometry for the optimization was based on the test section of the experimental tunnel. This section included a three-passage, two blade cascade. The blades used for this optimization were the L1A research blades developed by John Clark at the Air Force Research Laboratory. This blade is a modified version of the LIM blade previously discussed in Chapter 2, where the "A" signifies aft loaded. The initial tunnel wall geometry was the pressure and suction surfaces of the blades.

4.2 Method

The optimization was done using a program called iSIGHT by Engineous Solutions, along with Gambit, Fluent, and Matlab. Gambit is a program from ANSYS that creates the domain and grid for the numerical simulation based on user defined parameters. Fluent is a numerical solver, also developed by ANSYS, that can solve a wide variety of fluid flow and heat transfer problems. Matlab is a math program based on matrix mathematics. iSIGHT can distribute jobs to different programs and extract the needed data from the program's output files. It then takes the information and either passes it on or uses it with the optimization algorithms already programmed into the software.

The flow chart shown in Figure 4.1 shows how the optimization for this paper was achieved. First iSIGHT assigns to Gambit the wall geometry parameters and Gambit created the grid as defined by a pre-written journal file. Once Gambit completed the mesh it was sent to Fluent to solve for the flow features and extract the needed data. In this case the data taken was the coefficient of pressure along the suction surface of the blades. This data was then used by Matlab to calculate the residual sum. The residual sum was calculated by subtracting the c_p of blade 2 and 3 from the periodic solution calculated by the CFD model of Chapter 2 and squared at intervals of 1% along the blade chord. The squared differences from each location was then summed. Equation 4.1 shows how to calculate the residual.

$$R.S. = \sum ((c_{p1i} - c_{p2i})^2 + (c_{p1i} - c_{p3i})^2). \quad (4.1)$$

iSIGHT then used this $R.S.$ as the main variable in the cost function with a goal of minimizing the $R.S.$. As the $R.S.$ decreases, the c_p distributions should become similar to the periodic solution found by the methods of Chapter 2. Figure 4.2 shows the periodic solution of the L1A LPT blade used for the optimization runs. This periodic solution was used for the calculation of the $R.S.$ and the percent error plots.

Using this definition of residual sum, the $R.S.$ of the models from Chapter 2 are 0.00065 and 0.0002 for the L1M and Pack B blades, respectively. Due to the discrepancy in number of calculation points between the experimental solutions of Bons et al. [6], the residual sum values were altered to a average residual per calculation point and multiplied by the number of points (100 per blade) used in this residual sum calculation. The new

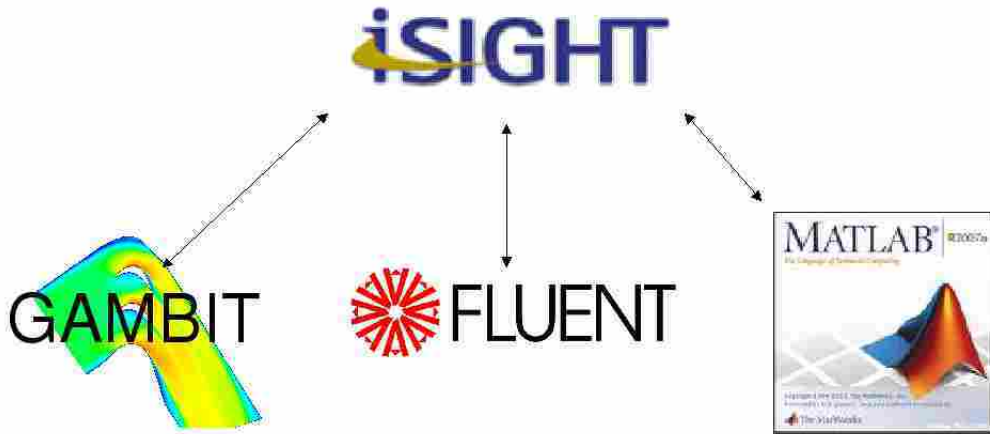


Figure 4.1: Flow chart of steps in the global iteration process.

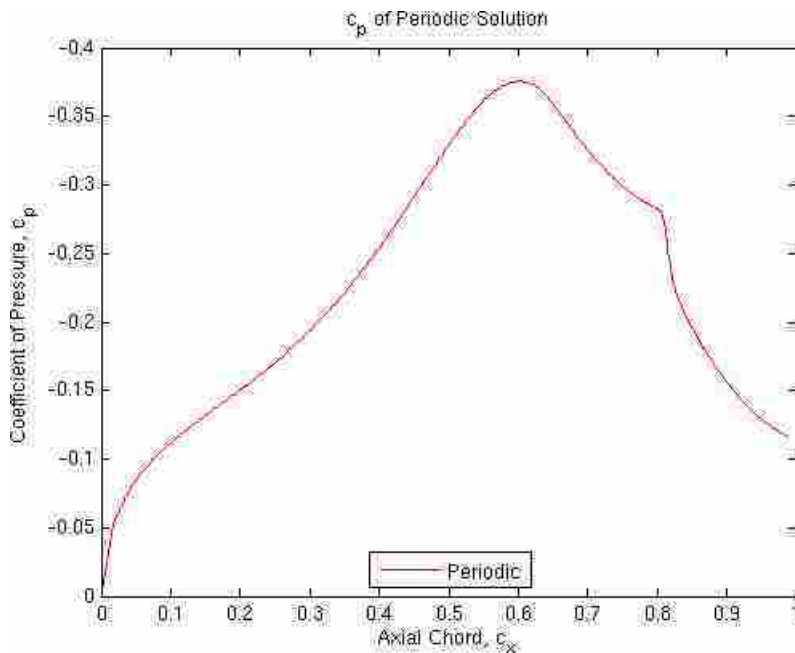


Figure 4.2: c_p distribution for the L1A LPT blade calculated from the CFD model of Chapter 2.

values of R.S. were 0.1299 and 0.0399 for the L1M and Pack B blade respectively. As discussed in Chapter 2, an oscillation in the c_p occurred at the turbulent transition location. This oscillation could potentially reduce the accuracy of the optimization results. As long as the oscillation does not occur in the desired periodic solution, the optimization can still be effective because manipulating the end wall geometry was able to constrict the flow and remove the oscillation. Based on the accuracy of the CFD model from Chapter 2 the

design goal could be $R.S. \leq 0.13$. If the optimization could predict the periodic solution exactly, the potential error would be the same as the accuracy of the periodic solution. If it was not exact the error of the optimization adds to the error of the periodic solution, potentially driving the solution farther from what physically happens. For this reason the closer the solution can get to the predicted periodic solution the better. The error of the CFD model drives the total error of the optimization. The root of the sum of the squares of the CFD model error and the optimization error shows that if the optimization error was small enough, the final error would be marginally higher. Therefore, the design goal was set at $R.S. \leq 0.01$ to have as little effect on the final error as possible. Because the root of the sum of the squares decreases slowly, the returns diminish and the cost of the iteration was no longer worth the improvement in R.S.. As can be seen in the following data where the solutions of R.S. were less than 0.03, the accuracy was visually better. The goal was stated as $R.S. \leq 0.01$, however any $R.S. \leq 0.03$ was acceptable.

The computational model was made using control points on both the top and bottom tunnel surfaces (see Figure 4.3). The nozzle portion located just before the inlet plane was defined as a straight line. The points along the middle of the domain were used to make cubic splines. These points were located at fixed x locations and could only be modified in the y direction to reduce the amount of variables in the optimization routine. The last section, or tail board section, was limited to a straight line as well. The straight line sections were intended to simplify the production of the test section and to easily provide for future design alterations. All the points after the nozzle portion of the test section were allowed to change. In total 12 points were considered as control points, six for the top surface (A-F) and six for the bottom surface (1-6).

The original optimization method used for the runs was the Successive Approximation Method. This method, as described by the iSIGHT documentation, is based on the LP-SOLVE technique developed by M. Berkelaar and J.J. Dirks [18]. It is a direct numerical technique that is gradient based, or based on the derivative of the design curve. This derivative is minimized until it is equal to zero indicating an optimum. Based on previous work on designing turbine and compressor blades, as well as wind tunnel walls, it has been found that gradient based techniques can be used successfully in optimizing a desired

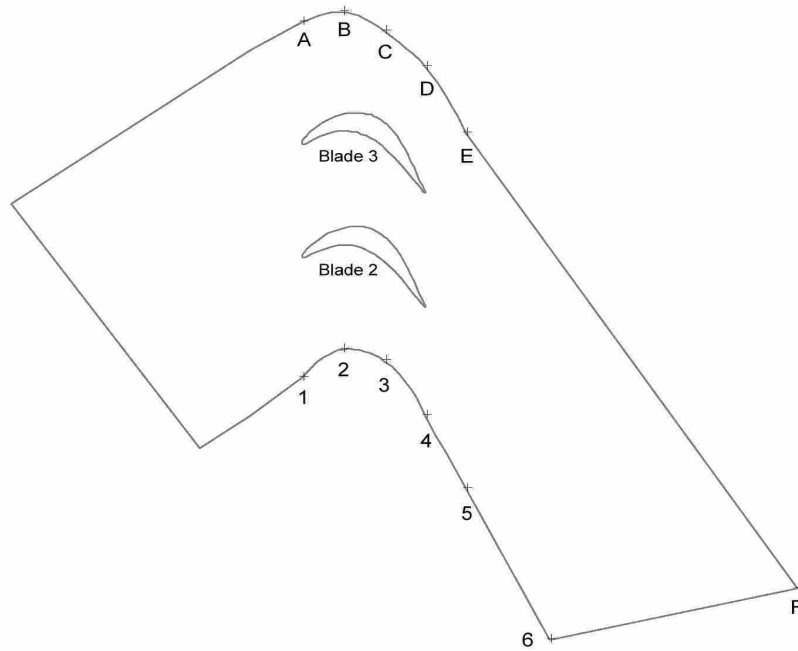


Figure 4.3: Tunnel domain with the variable control points on the top and bottom surfaces.

flow field [16]. An example of this success was shown by Laskowski et al. [10] where the method of steepest descent was used to optimize the wind tunnel geometry of a transonic turbine blade. The successive approximation method uses a Simplex algorithm and sparse matrix calculations for linearized problems. This method was included in the software iSIGHT used for this computational experiment.

It will be seen from the results that the successive approximation method was not completely satisfactory in creating an optimum periodic blade design. Thus two other optimization methods were used to further reduce the *R.S.* of the c_p curves. The methods used were the adaptive simulated annealing and the Hooke-Jeeves method and are both included in the iSIGHT software.

The adaptive simulated annealing, as described in the iSIGHT documentation, was designed to resemble the annealing process of solid materials. Unlike the successive approximation method, this method is not gradient based. This technique is an exploratory technique that can distinguish between local optima to find a global optimum. The simulated annealing method considers the neighbors of a current state and probabilistically determines whether to stay at the current state or move to the neighboring state. The algo-

rithm moves in the direction of "lower energy" until the desired state is achieved or until the computational budget has been exhausted.

A local optimum is where the design curve reaches a maximum or minimum that is not the true/global optimum. For example, in the search for the highest point on earth, a local maximum would be Mt. McKinley, or any other mountain in the world besides Mt. Everest. The only global maximum and the highest point on earth is Mt. Everest. It is not designed for long running simulations due to the time it takes to do the necessary calculations and the large number of iterations required. However, the number of possible local optima is very large because of the number of control points. A method that best overcomes these local optima to find the global optimum is preferable to a method resulting in an incomplete optimization.

The Hooke-Jeeves method is a direct penalty optimization method that is not gradient based. It works by creating a stencil of the objective, and calculating different points on the stencil. The points calculated are defined by the exploratory movements in the finite number of directions on the stencil. Unlike other methods, the Hooke-Jeeves method does not use quantitative information about the function values, it uses only qualitative information [19]. This method is also not well-suited for long simulations due to possibility of repetition in calculating points on the objective stencil. This method is susceptible to finding local optima, and should be used carefully to avoid the local optima.

Five differing test section domains were optimized using the successive approximation method. The domains include the original test section with a $0.41c_x$ nozzle leading the blade row inlet plane, a narrow tunnel case where the width of the original tunnel domain was reduced by $0.1c_x$, an extended nozzle case where the length of the nozzle was doubled, a variable Re case that was the same geometry as the extended nozzle with an added optimizing variable Re, and a full tunnel case, increasing the number of control points by 2, that included the full length of the tunnel and not just the test section. The narrow tunnel case was chosen because the original case was too wide. The extended nozzle case allowed for a simple change that could improve the incoming flow field. Variable Re was tested to simplify the domain without changing the domain parameters. The full tunnel was tested to

prove that the incoming boundary layer profile, defined by the user, was not the limitation of optimization, and allowed more control of the flow entering the blade passages.

The *R.S.*'s were calculated and the effectiveness of the domains were compared using the *R.S.*, domain geometry and velocity magnitude contour plots, c_p comparison between the domain blades and the periodic blades, and the percent error distributions of the blades' c_p . Further investigations were made on two other optimization methods, the simulated annealing and Hooke-Jeeves, to find whether local optimums were found using the successive approximation method. The narrow tunnel and variable Re cases were used with the simulated annealing method. While the extended nozzle and full tunnel were run with the Hooke-Jeeves method.

4.3 Results

The first runs used in the optimization used the gradient based successive approximation method of optimizing. The 12 control points were changed one at a time as defined in the optimization algorithms. A method of reducing the number of variables was to run the optimization for the top surface only, then run the bottom surface later. The optimization was then finally run with both surfaces to refine the results.

4.3.1 Original Domain

The optimization of the original domain resulted in a *R.S.* of 0.054. The *R.S.* was a good measure of how close the whole c_p distribution matches the periodic. However, a more descriptive measure was needed to analyze the results more effectively. Percent error was chosen to analyze the flow where

$$\%error = \frac{c_{pli} - c_{pni}}{c_{pli}} \quad (4.2)$$

where i = axial location and n = blade number. The advantage of using the percent error is that a profile of error can be plotted along the axial chord of the blades, enabling a more detailed assessment of the accuracy of the solution. The percent error of the c_p 's compared to the periodic blade solution of Section 4.2, as seen in Figure 4.4 had a maximum error of 80% near the leading edge and after 50% axial chord reduced to below 5%. The reason for the high error at the leading edge will be discussed in Section 4.3.2 This however created

a wall geometry that was not desirable as shown in Figure 4.5. The nozzle, as defined the Figure 3.3, reduced the area so much such that the downstream area bulged out to create a recirculation zone. A recirculation zone is where the fluid flows in a circular pattern, against the direction of the bulk flow. When the wall points were constrained to not allow that behavior the $R.S.$ increased to 0.079.

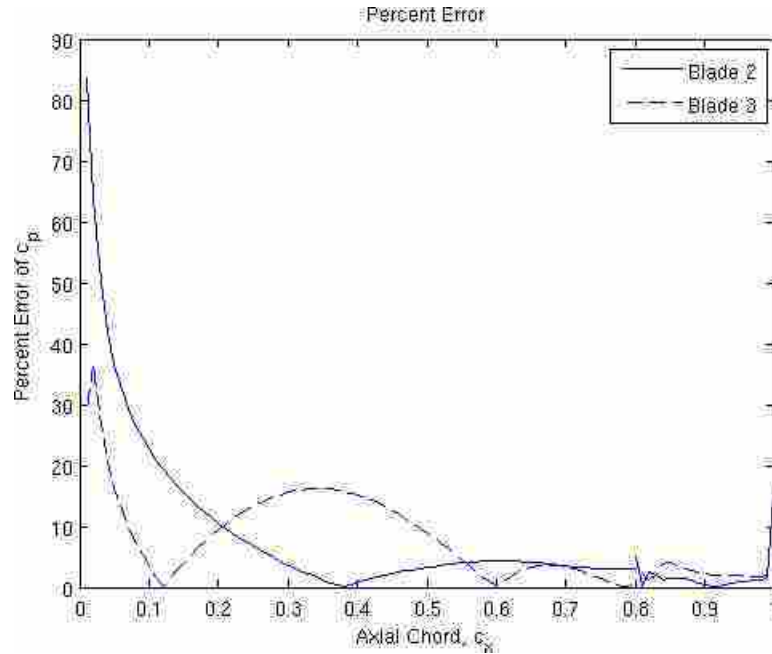


Figure 4.4: Percent error of both tunnel blades compared to periodic solution for the original optimization domain.

Two correlating effects were believed to cause this odd solution to the wall geometry. First, because the distance between the blade and end wall was larger than the blade design spacing, the blade tended to have a lower pressure along the suction surface, increasing the size of the blade separation region. To compensate for the larger spacing and resulting lower velocity, the nozzle section constricts the flow which then increases the velocity and the c_p . This constriction is an attempt to better match the c_p distribution along the front section of the blade. The bulge acts similar to a bleed, removing some of the momentum from the flow, and thereby reducing the pressure coefficient along the mid-section suction surface of the blade. Figure 4.6 shows the c_p distributions of the blades for this optimized solution.

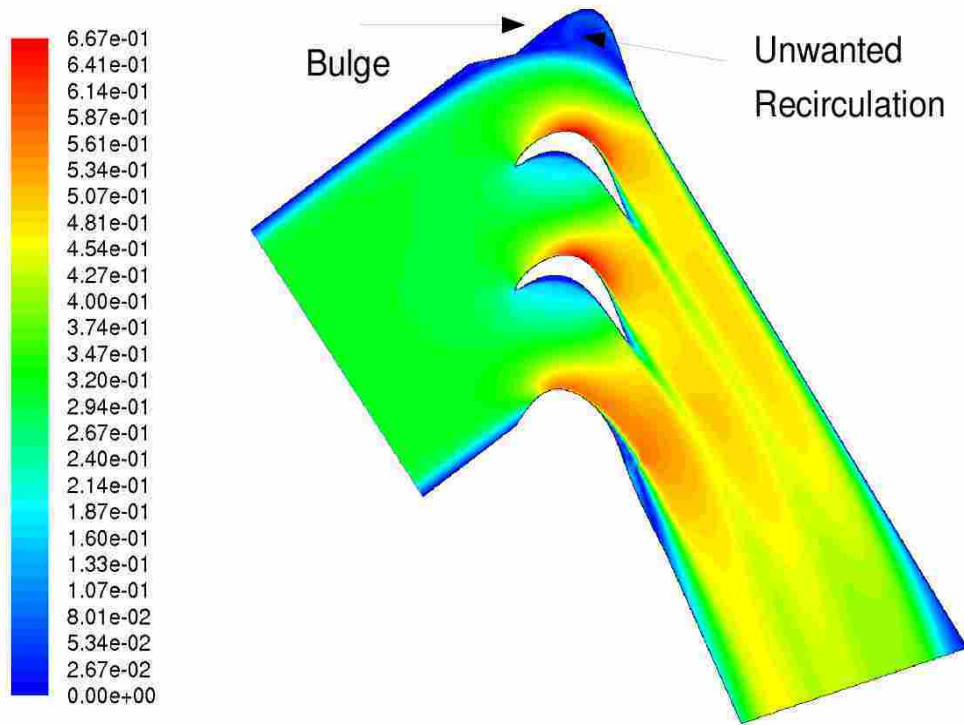


Figure 4.5: Tunnel geometry showing the large bulge on the pressure wall of the tunnel and the velocity magnitude contours for the original optimization domain.

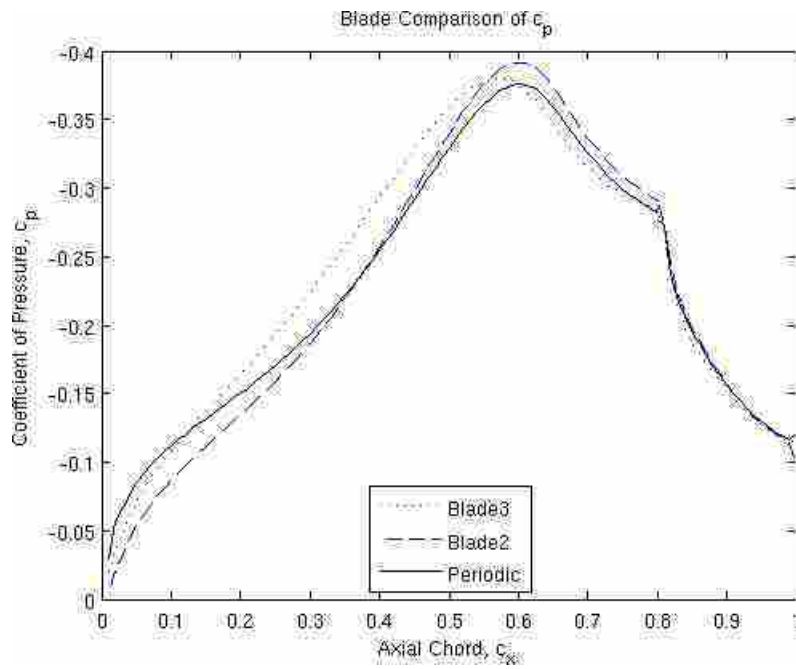


Figure 4.6: c_p of both tunnel blades compared to the periodic solution.

These two effects can both be remedied by changing the computational domain or boundary conditions. Two ways were hypothesized to improve the solution by overcoming the issues of the tunnel being too wide. One was to change the width of the tunnel and the other to decrease the blade Reynolds number. These were both tested as to their effectiveness. These changes are presented in the following section. The unrealistic geometry seen in the optimization shows up in many of the subsequent experiments. Laskowski et al. [10] provided a method of eliminating the bulges once the optimization has been completed. This method uses the streamline between the circulation and bulk flow as the wall geometry. While attempts were made to obtain an optimized geometry without nozzle contraction and recirculation zone, in the end it will be shown that the method of Laskowski was needed.

4.3.2 Narrow Tunnel

Figure 3.8 shows the effect of wall spacing on the c_p distributions of the the blades. The wide tunnel spacing shows a decrease in c_p , while the narrow spacing increases the c_p . Because the tunnel was designed to be wide to allow the existence of a boundary layer the c_p is smaller than it should be. Figure 4.5 also shows the need for the tunnel to be narrower because of the obvious nozzle constriction on the top end wall, increasing the velocity and c_p . The optimization was run with a narrow tunnel configuration to further reduce the $R.S.$.

The optimization of the wind tunnel was run after the width of the tunnel was changed by 0.6 inches or 0.1 axial chord. This change improved the optimization by 38% to a $R.S. = 0.03368$, and the bulge created by the previous optimization run was less significant but the recirculating region was still present, indicating the continued need for a decrease in flow momentum over blade 3. Figure 4.7 shows the geometry of the narrow tunnel and the recirculating region. It was observed that the boundary layer on the lower wall was reduced and the size of the boundary layer on the upper wall constantly increased.

The c_p distributions shown in Figure 4.8 show the difference between the desired periodic solution (the design goal) and the narrow tunnel blades. The maximum c_p was larger and it was slightly shifted downstream. The leading edge of the blade was significantly different, which can also be seen in Figure 4.9, from the percent error of c_p between the periodic blade and the optimized solutions. The region between $0.2c_x$ and $0.5c_x$ for

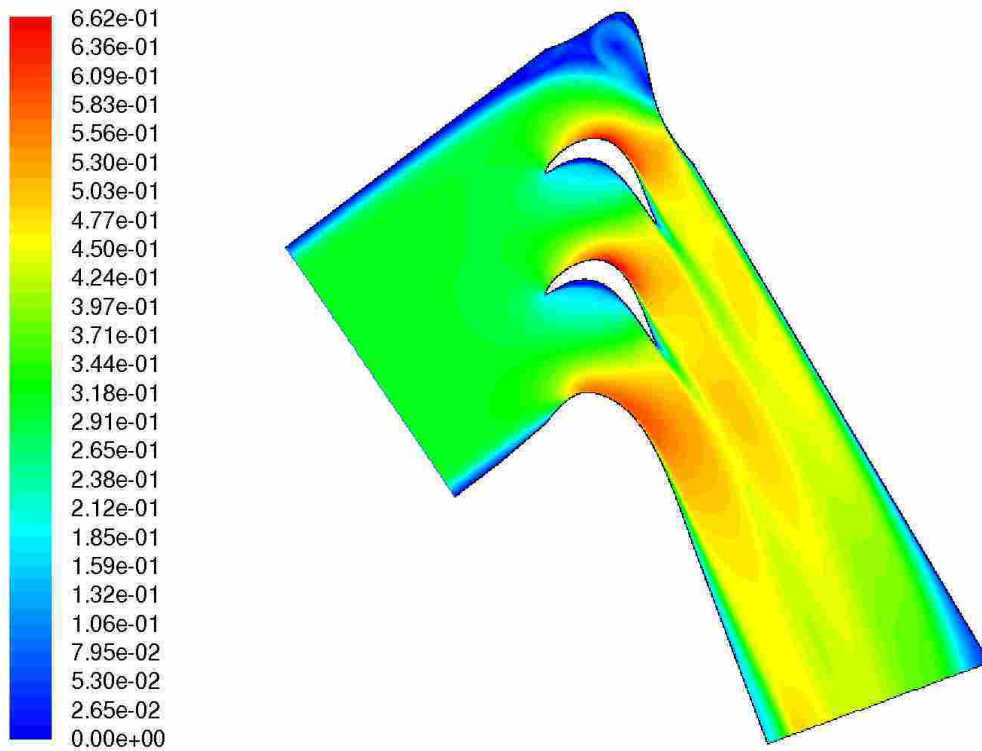


Figure 4.7: Tunnel geometry showing the large bulge on the pressure wall of the tunnel for the narrow tunnel case.

blade 3 shows the largest difference between the original solution and the narrow with the error of the original reaching 20%, while the error of the narrow is reduced to 10%. The percent error was more than 40% at the blade passage entrance, and was reduced to less than 10% as the flow moved along the blade. The disparity of the optimized solutions and the periodic solution near the leading edge of the blade can be partly attributed to the magnitude of the c_p . From the c_p plot of Figure 4.8 the difference between the optimized and periodic solutions are similar. Because of the size of the c_p the percent error is larger. However, the inlet flow characteristics of the c_p are crucial to providing an accurate solution. If something starts with the wrong values, those wrong values will propagate through the domain. The inlet characteristics of the flow, such as velocity and flow angle affect the accuracy of these first crucial c_p values. These characteristics were developed from the boundary layers created by the tunnel walls.

It makes sense that a narrower tunnel would increase the c_p values due to the acceleration of the interior flow caused by the boundary layer thickness on the tunnel walls.

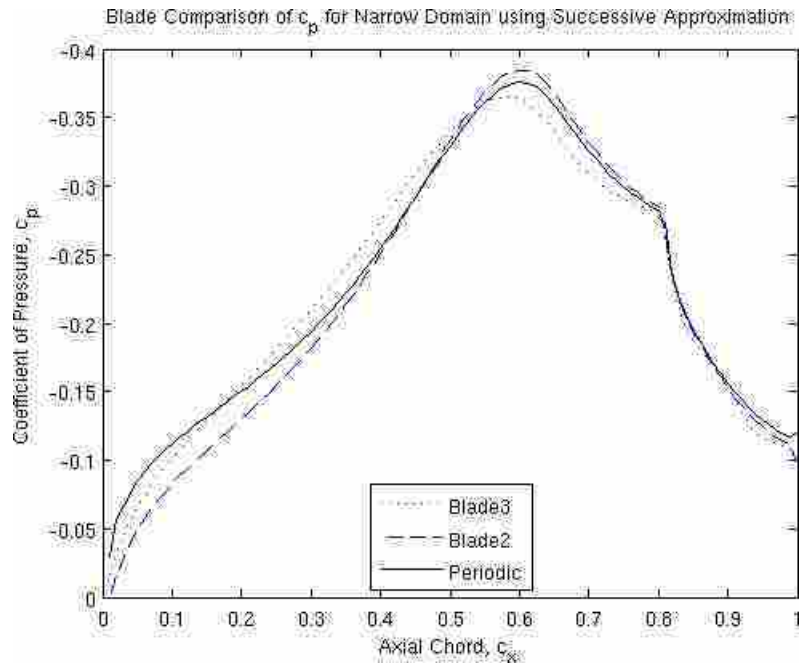


Figure 4.8: c_p distribution of the narrow tunnel using the successive approximation optimization method.

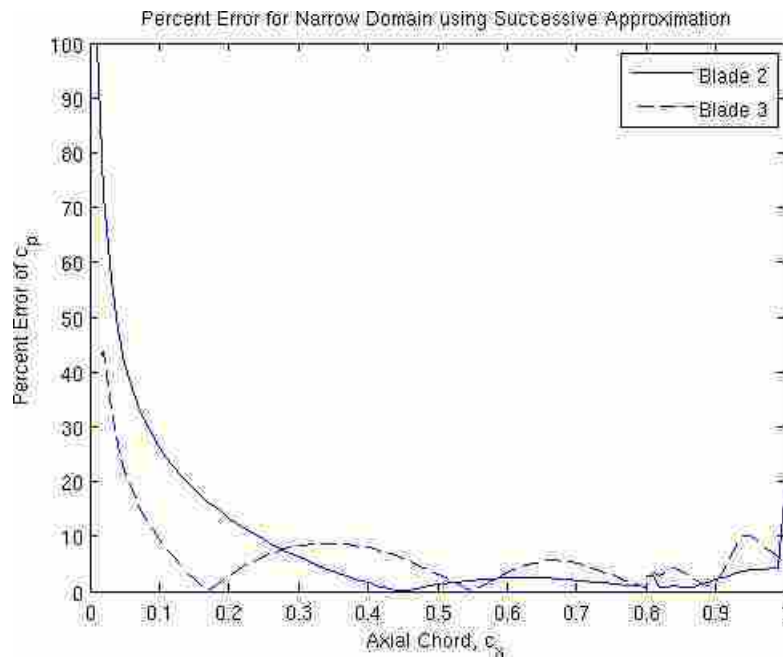


Figure 4.9: Percent error of both tunnel blades compared to periodic solution for the narrow tunnel domain.

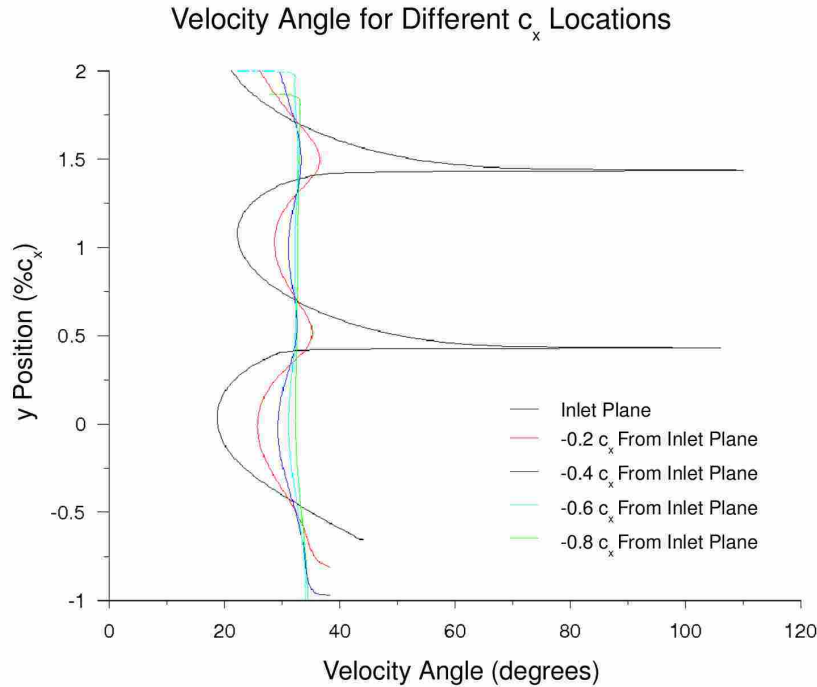


Figure 4.10: Velocity angle of the incoming flow at various c_x locations for the narrow tunnel domain.

In Chapter 3 it was discussed that flow direction had an impact on the c_p of a blade. Figure 4.10 shows the flow angle difference between both blades. The plot shows the flow angle with respect to height along five different vertical lines. It can be seen that the lower half has different flow angles than the upper half. The lower half represents the flow in front of blade 2 while the upper half represent the flow in front of blade 3. This difference in flow angles explains the difference in maximum c_p location for all flow solutions. An increased flow angle will result in the maximum c_p location shifted forward and vice-versa. The flow angles for the upper half of the flow angle plot were larger, indicating that the maximum c_p location for blade 3 was shifted forward, which was also confirmed in the c_p plots of Figure 4.8. It can be seen that the narrow tunnel geometry does not satisfactorily predict the desired flow field, as the $R.S.$ is still too large.

4.3.3 Reynolds Number

Because the blades and the main sections of the tunnel have already been designed and built, making the tunnel narrow is not a desired outcome. Only the test section can eas-

ily be changed. Therefore it was hypothesized that by altering the inlet Reynolds number it would be possible to better match the periodic solution by reducing mass flow and decreasing the need for a bleed/recirculation zone. In the existing domain a velocity profile was needed to account for boundary layer growth through the long tunnel section before the test section. Changing the Reynolds number by changing the velocity profile would be complicated and add much more time to the optimization routine. Hence, it was decided to simply change the viscosity of the fluid to alter the Reynolds number of the flow in the test section. A consequence of this approach was that changing the Reynolds number also changes the velocity profile of the inlet plane of the blade row. However, a sufficient understanding of the effect of the Reynolds number was achieved by doing this simple process.

Figure 4.11 shows the optimized domain achieved by adding fluid viscosity as a variable in the optimization technique. The wall geometry did not dig into the flow as the original case and the end wall became less pointed. This could be considered an improvement, however, the $R.S.$ was only reduced to 0.1143, double that achieved from the original solution. The viscosity for the fluid was increased from $1.7984e - 5$ to $2.3e - 5$, which reduced the Reynolds number, as expected, from 20,000 to 15,550. Even though the bulge on the top wall was not as pointed, it still created a recirculating flow region. This characteristic was undesirable and continued efforts to remove the bulge were made. A separation region can also be seen on the bottom wall of the domain in Figure 4.11. This separation was similar to the separation regions along the blade suction surface, however, much larger. Because this separation exists downstream of the blades, it did not significantly affect the c_p .

The c_p distribution shown in Figure 4.12 shows that the c_p for blade 3 was still close to the periodic solution, and similar to the previous distributions where the wall digging into the flow had the same effect as increasing the Reynolds number. However, it was also obvious that the c_p of blade 2 was very different than the periodic solution. The nozzle section constricts the flow and increases the velocity. The effect of the increase in velocity behaved as expected, increasing the c_p for blade 3, better matching the periodic solution. The increase in velocity increased the c_p distribution of blade 2 as well. The spacing between blade 2 and blade 3 did not change, making the velocity too great for

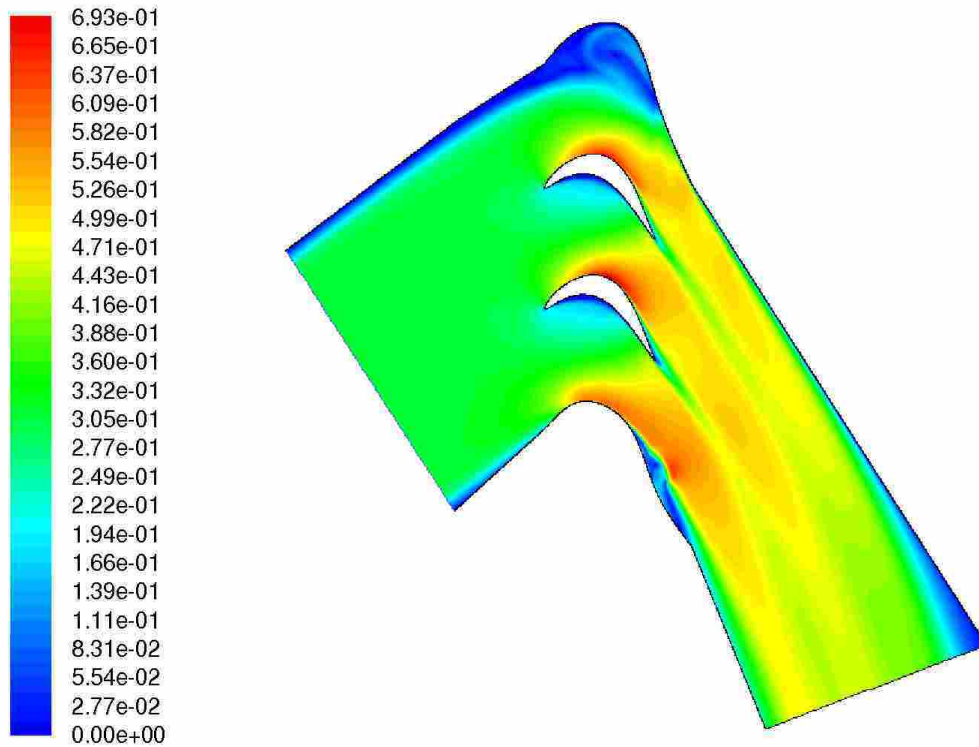


Figure 4.11: Tunnel geometry and velocity contours for the variable Reynolds number case, $Re=15,550$.

that blade spacing. The error plot in Figure 4.13 shows that the error for blade 2 remained unacceptably large. This change of the velocity had a detrimental effect on blade 2 and a positive effect on blade 3. For this reason, changing the Reynolds number of the entire flow was not a good method to optimize the domain, and changing only the wall geometry should be sufficient.

4.3.4 Longer Nozzle

Due to the lack of improvement realized from using the Reynolds number as a variable and the complications involved in making the whole tunnel narrower or wider, another design variable was tested using knowledge gained from the previous results. It was apparent that the narrow tunnel solution was accurate, the only downside being the requirement of rebuilding the whole tunnel. The decreased Reynolds number solution showed that the change in Reynolds number effected the magnitude of c_p . Therefore a way to change the c_p locally, such as flow acceleration or deceleration, instead of globally was desired.

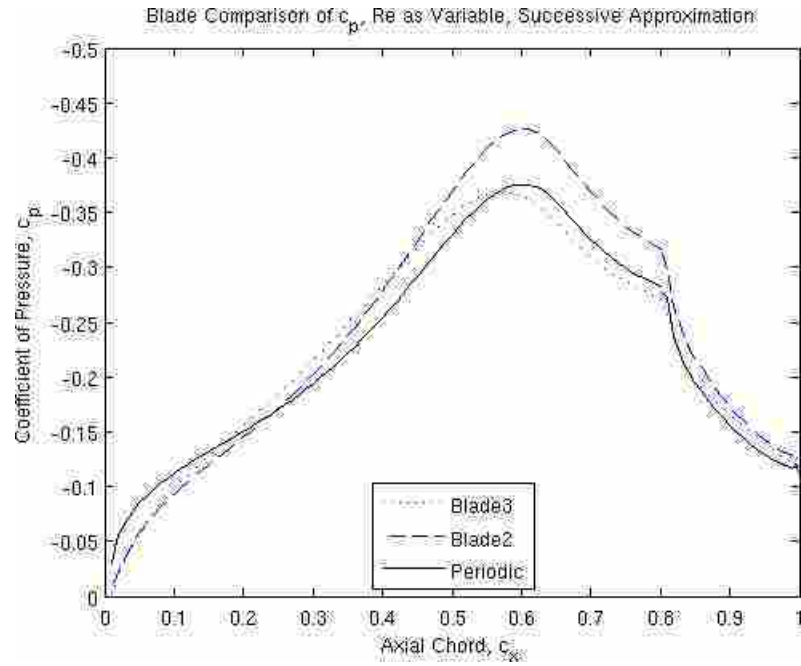


Figure 4.12: c_p distribution of the variable Reynolds number case, $Re=15,550$ using the successive approximation optimization method.

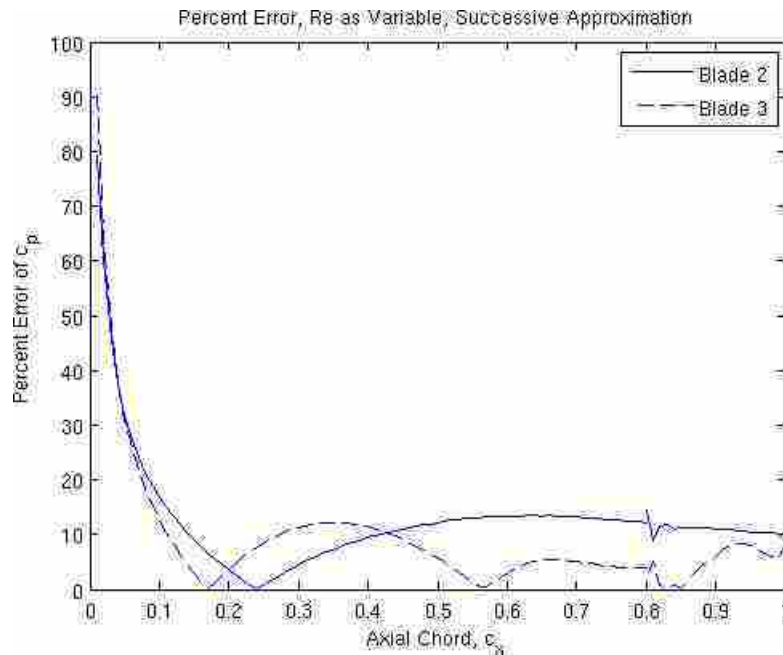


Figure 4.13: Percent error of both tunnel blades compared to periodic solution for the case of variable Reynolds number, $Re=15,550$, using the successive approximation method.

Previous solutions showed that the nozzle had an effect on the results of the optimization runs. The nozzle effectively accelerates the flow as it enters the inlet plane of the blade row. This change took place in such a short distance that the whole flow field may not have been changed before the blade row inlet plane. It was hypothesized that the length of the nozzle would make the needed velocity change more effectively than the original length. Changing the nozzle length was a much simpler change compared to altering the whole tunnel.

The nozzle geometry, as defined in Figure 3.3, was moved forward to $0.8c_x$, from $0.41c_x$ of the original optimization geometry, upstream from the leading edge of the blade. This nearly doubled the original length. The optimization of the extended nozzle did show improvement over all the other cases tested except for the narrow tunnel case. The *R.S.* was calculated to be 0.0498, which was a 8% improvement over the original domain optimization. This improvement showed that a more gradual change of area resulted in a better solution. However, it still did not satisfy the desired minimum of $R.S. \leq 0.01$.

Figure 4.14 shows the optimized solution created by the lengthened nozzle section. The top wall has a sinusoidal shape that digs into the flow then stretches out the flow. Although the geometry is undesirable, the principles it represents are accurate. The constricting portion of the flow increases the fluid velocity and results in an increase in c_p , while the diffusing portion results in a decrease in c_p . The fact that it is occurring was a good sign that the optimization technique was moving c_p in the right direction. This end wall represents the need for greater acceleration (caused by a constriction) and deceleration (caused by diffusion) for the c_p to match the periodic solution. Again, this geometry was not a desired solution.

The c_p distribution for this solution is seen in Figure 4.15. The location of maximum c_p was $0.02c_x$ farther upstream than the periodic solution, a result of the changing blade inlet plane velocity angles as was observed from the optimization run of the narrow tunnel. The maximum c_p of blade 3 was very near the periodic solution while the maximum for blade 2 was much larger. This larger c_p was a result of the accelerating flow entering the unchanged spacing between blade 2 and blade 3. This distribution was very similar to the case where Reynolds number was added as a variable.

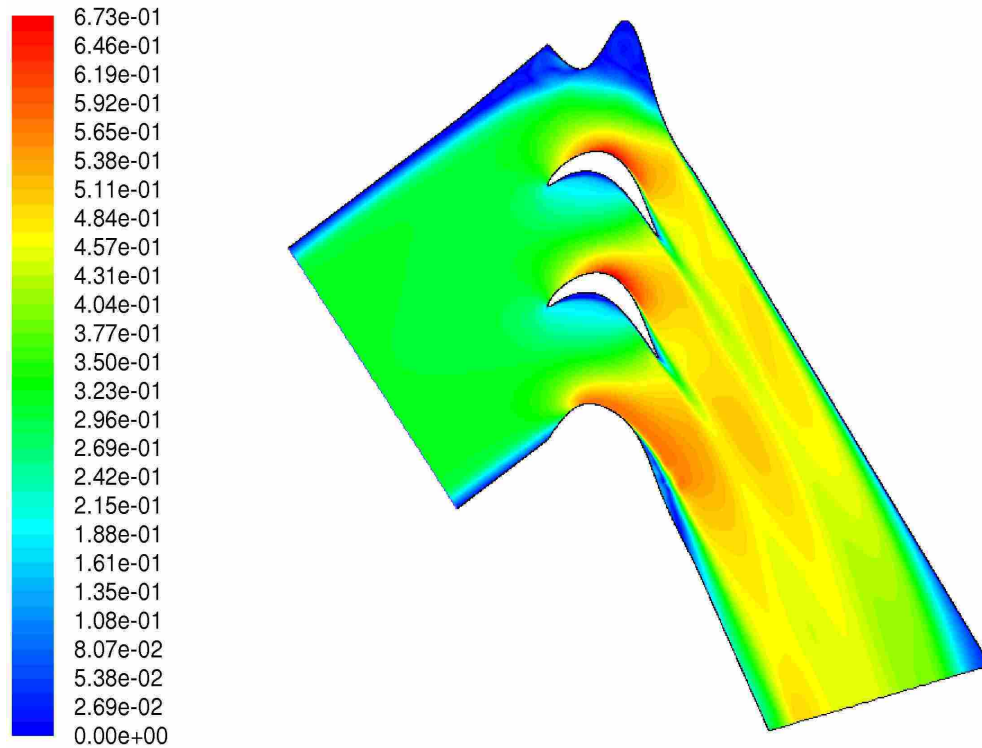


Figure 4.14: Optimized end wall geometry and velocity magnitude contours for the case of extended nozzle length.

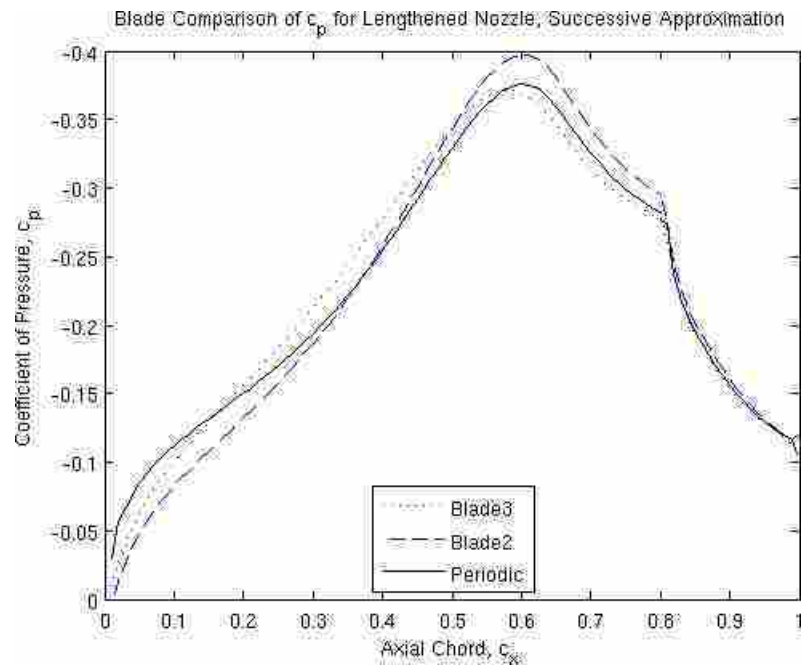


Figure 4.15: c_p distribution of the extended nozzle length case using the successive approximation optimization method.

The percent error of the extended nozzle run, shown in Figure 4.16, also shows similarities to cases where the Reynolds number was added as a variable. The error was very large near the beginning of the blade and decreased as it moved downstream, as shown in all the optimization runs. The error for blade 2 was about half of what the variable Reynolds number simulation predicted. This decrease showed that the nozzle had a similar effect on the flow, but was able to predict a closer solution because of local changes to geometry instead of a global Reynolds number change.

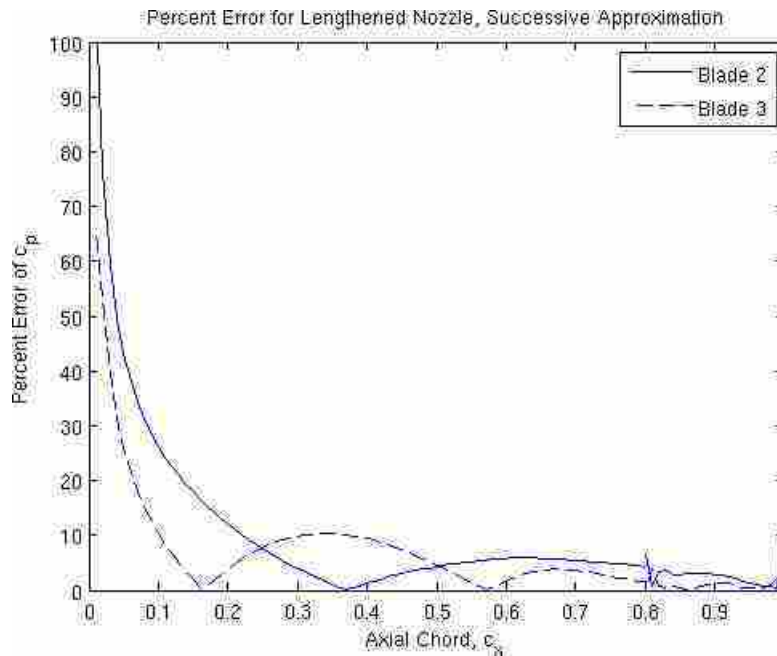


Figure 4.16: Percent error of both tunnel blades compared to periodic solution for the case of extended nozzle length entering the test section.

4.3.5 Full Tunnel

Because none of the methods resulted in the desired minimum $R.S.$, the whole tunnel was modeled to decide whether the inlet conditions of the smaller domains were the reason for the higher than desired $R.S.$. The full tunnel also allowed more control of the domain, increasing the ability to alter the flow field. Modeling the whole tunnel also allowed for changes in tunnel width without having to redefine the inlet velocity profile.

However, the simplicity of applying this design to the experimental hardware of Bons [6] was diminished, since a new tunnel would need to be built.

The full tunnel domain adds $12c_x$ onto the front of the previous domains. Figure 4.17 shows where two control points were added, now named B1 and TA. A boundary layer mesh was placed on the walls of the new section of tunnel to match the already existing boundary layers. The boundary layer mesh had a spacing of $h/c_x = .0005$ for the first node off the wall, and extended approximately $h/c_x = .0158$ from the wall, with a growth rate of 1.1. The values for the mesh were determined from the grid refinement study of Chapter 2. Outside the boundary mesh, unstructured triangles were used to mesh the remainder of the domain. Adding the new length of tunnel onto the domain doubled the number of cells from 344,806 to 687,256. Because the new domain had the same boundary layer and unstructured grid parameters as the previous cases, the new grid was deemed sufficient and a grid refinement study was not done. Figure 4.18 shows the extent of the domain.

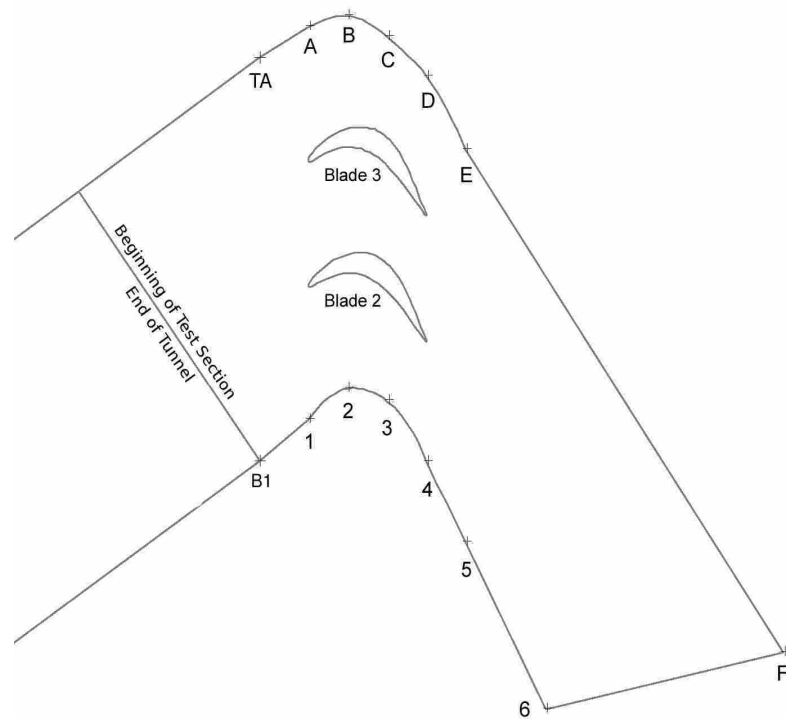


Figure 4.17: Full tunnel control point configuration, where B1 and TA are the added control points.

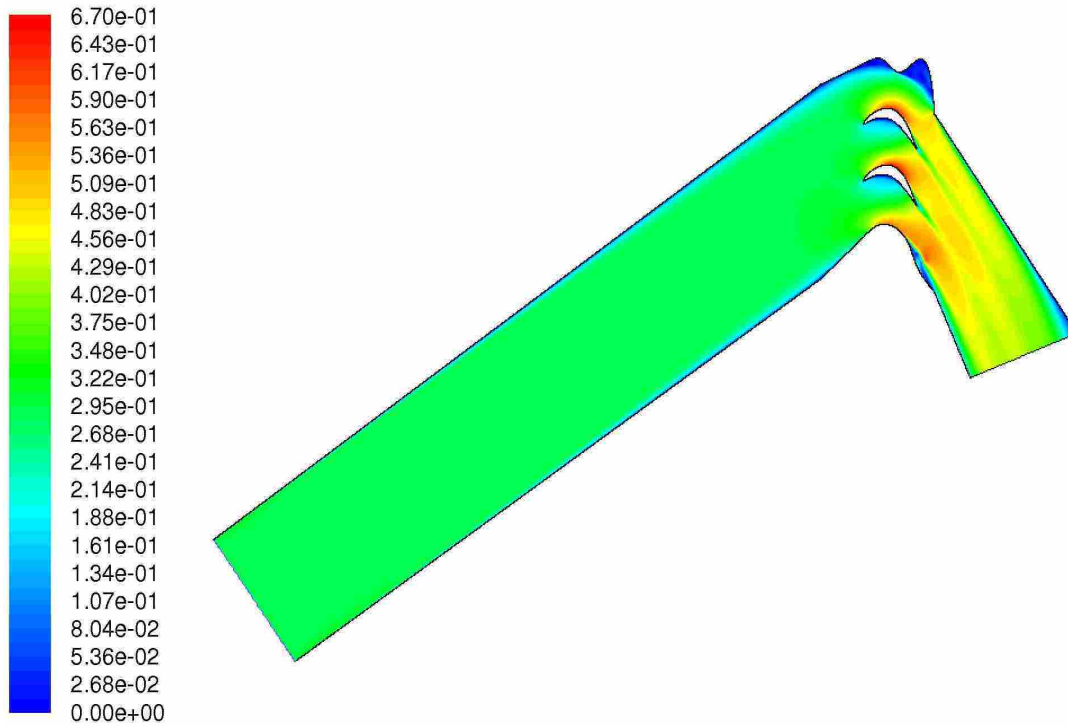


Figure 4.18: Full tunnel configuration including $12c_x$ upstream from the inlet plane of the blade row and velocity magnitude contours.

The optimized solution for the extended domain resulted in a *R.S.* of 0.05656, slightly worse than the original domain. Figures 4.18 and 4.19 show the optimized results for the extended domain runs. Figure 4.18 shows that the large tunnel section before the test section got wider as the flow moved toward the test section. This diffusion allowed the velocity at the test section inlet to be the same and remain flat outside of the boundary layer region. It was observed that the nozzle section constricted the flow after it had passed through the diffusion of the rest of the tunnel. This process of diffusing and constricting seems to remove the effect of the boundary layer on the flow. Figure 4.19 shows a closer view of the wall geometry and the flow features. This wall geometry differed from the other cases in that there were two smooth humps on the upper wall that grew in the c_x direction. The two smooth humps indicated the need for a reduction of c_p in two spots instead of one. The smooth curve abruptly ended at the beginning of the tailboard section. The end wall on the bottom of the domain also had a recirculation zone that mimicked the separated flow of the blades.

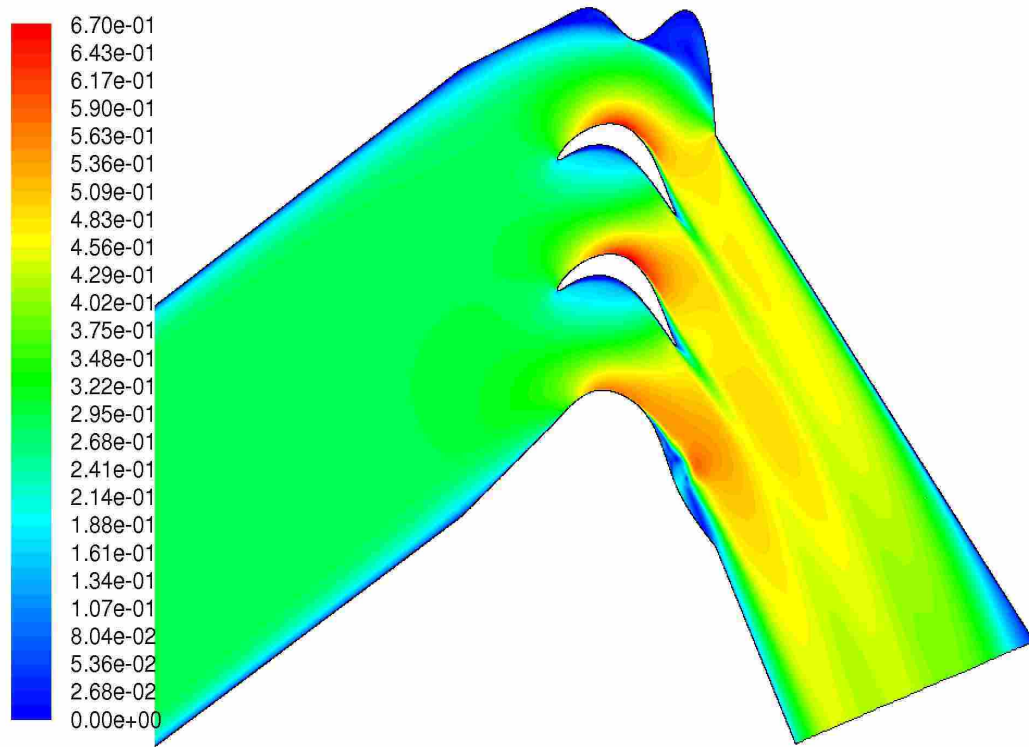


Figure 4.19: Close up view of the tunnel geometry showing the large bulge on the pressure wall of the tunnel and velocity magnitude contours for the full tunnel geometry using the successive approximation optimization method.

The c_p plot of Figure 4.20 shows some interesting features. The maximum c_p for blade 3 was 6% lower than the periodic, which indicated the velocity was not high enough. The c_p of blade 2 was 13% higher than the periodic, indicating the velocity was too high. This is similar to results found in the cases where Reynolds number was added as a variable and where the nozzle length was increased.

As with all other cases, the maximum percent error for this case was near the front of the blade, as shown in Figure 4.21. The maximum error in this case was much smaller compared to the other cases. The original case had a maximum error of over 80%, while the maximum for the extended nozzle was less than 60%. This was likely due to the smoothness of the end wall geometry, whereas the other cases always had an instantaneous change in direction as observed in Figure 4.14. However for this case the percent error did not steadily decrease like the previous cases. The large difference in maximum c_p location for blade 3 and the over-prediction of blade 2 prohibited a reduction in error. It was concluded

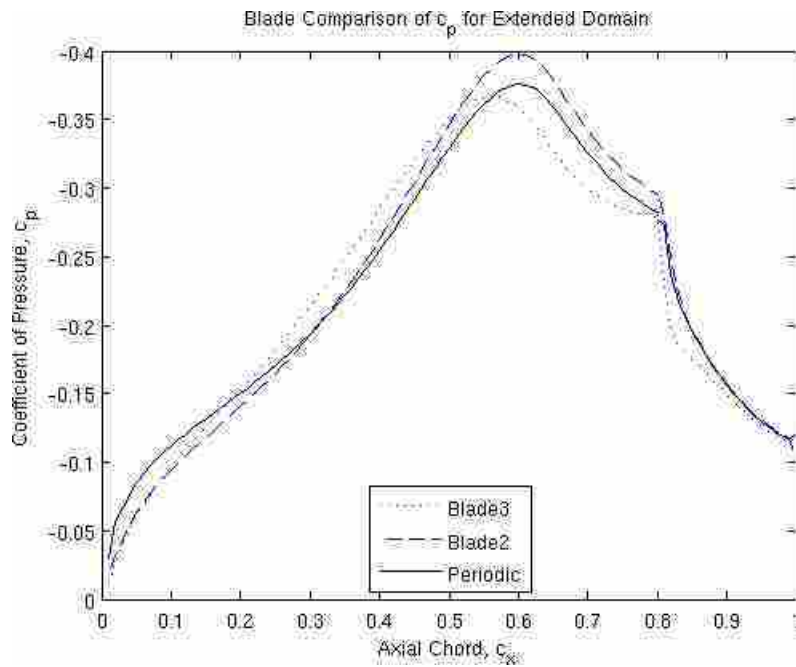


Figure 4.20: Showing the c_p distribution of the extended tunnel using the successive approximation optimization method.

that including the whole tunnel to the domain did not improve the solution, and the abbreviated domain should suffice. However, a test of optimization algorithms for this domain would be interesting because of the greater potential for good results.

4.3.6 Successive Approximation Summary

The successive approximation optimization method has been shown successful in finding improvements to matching the c_p distribution of the periodic blade solution. This method has resulted in the best solution of $R.S. = 0.03368$ for the narrow tunnel case. The results are shown in Table 4.1. Although the improved results did not meet the desired criteria of $R.S. \leq 0.01$, they were all as accurate as the CFD model itself from Chapter 2. The error of the solutions obtained by the successive approximation method can add to the error of the CFD model. Therefore less error is desired in the optimization solutions. Gradient based methods, such as the successive approximation, have been found to get stuck on local optima [20]. This may be the case for the successive approximation method used here. The only way to find out if a global maximum was found is to continue the

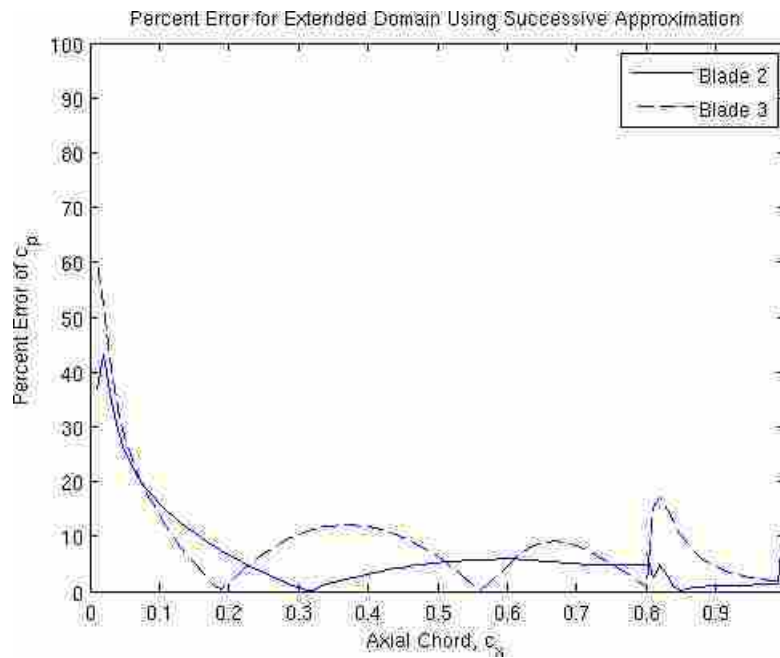


Figure 4.21: Percent error of both tunnel blades compared to periodic solution for the extended tunnel case.

Table 4.1: *R.S.* for Successive Approximation Method

	Successive Approximation	Comments
Extended	0.05656	flat incoming velocity profile, smooth end walls, potentially more accurate
Narrow	0.03368	Best solution, requires tunnel rebuild, good for blade 2, bad for blade 3
Nozzle	0.0498	easy to build, improved <i>R.S.</i> over original by 8%, dual hump end wall
Original	0.054	easy to build, large recirculation near end wall, too wide
Reynolds	0.1143	reduced <i>Re</i> , increased constriction, good for blade 3, bad for blade 2

search for an optimum using a different initial condition or other techniques. The next section discusses other optimization methods to improve the error of the solutions.

4.3.7 Optimization Method Change

The inability of the successive approximation method to reach a desired minimum suggested a re-evaluation of the optimization methods used. Based on previous experiments by Laskowski et al. [10] and conversations with other engineers that had done similar optimizations, it was decided gradient based methods were sufficient. However further investigation into gradient based methods shows that they are easily susceptible to finding only local minimums and require a very good initial guess to achieve a global minimum [20]. The following section will show that the successive approximation method used was finding only local minima and was not able to find a global minimum. One of the recommended methods given by Miyata et al. [20] for optimizing turbomachinery was a simulated annealing method. This method, as described in Section 4.2, prevents the optimization from getting trapped in regions where a local minimum exists. The method was also used by Ashihara and Goto [17] in a pump impeller design. Another method tried was the Hooke-Jeeves, a direct penalty method, that could help remove the recirculation caused by the end wall.

All previous optimization domains, other than the original, were used to test the effectiveness of the two new optimization techniques. Two cases each were run with the simulated annealing and Hooke-Jeeves optimization methods. The two domains run with the simulated annealing were the narrow tunnel and the variable Reynolds number cases. The Hooke-Jeeves method was run with the lengthened nozzle and the full tunnel. The cases were run simultaneously.

Simulated Annealing Narrow Tunnel

The narrow tunnel showed the best results for the successive approximation method, and has proven that narrowing the tunnel positively affects the solution. Because of the ability for this domain to achieve good results, a good comparison of the optimization methods can be made using this domain. The difference in results between the successive approximation and the simulated annealing for the narrow tunnel can be seen in Figures 4.22, 4.23, and 4.24. The *R.S.* was calculated to be 0.021 for the simulated annealing solution. This was a 38% improvement over the successive approximation method.

The differences in geometry, as seen in Figure 4.22 are the top end wall. The successive approximation predicted the single large bulge in the top wall while the simulated annealing predicted the more complex dual hump wall. The recirculation zones exist in both solutions. These humps allow the geometry to directly change the c_p distribution to match the periodic c_p . For this narrow tunnel case, the nozzle section actually becomes a diffuser section, and the velocity decreases. The bottom wall transition to the tailboard section shows another separation. This section has little effect on the upstream blades, and is likely an insignificant feature of the solution. However, this method still did not reach an acceptable minimum value of $R.S.$, and the end wall geometry did not show the simplicity desired.

The improvements in c_p and percent error are shown in Figures 4.23 and 4.24 respectively. The c_p curves of blade 3 for the simulated annealing case showed an improvement in predicting the maximum c_p location from $0.57c_x$ of the successive approximation method to $0.59c_x$. The periodic value of the maximum c_p location is $0.6c_x$. The magnitude of the maximum for blades 2 remained the same, while blade 3 improved from -0.365 to -0.37 , where the periodic maximum is -0.375 still over predicted. The entrance region of both blades also matched better. The improvement of the entrance region is clearly observed in Figure 4.24. Notice the maximum error, that had previously been very high, started out lower at 0.6 . The region between $0.5c_x$ and $0.82c_x$ showed a large decrease in percent error, indicating that the solution optimized this region of the blade very well. The ability to optimize the last half of the blades suggested that despite the blade row inlet conditions, the end wall geometry effectively manipulated the c_p distribution to overcome the negative effects of boundary layer and flow angle present at the blade row inlet.

Simulated Annealing Reynolds Variable

The variable Reynolds number case was also re-run using the simulated annealing optimization method. This method decreased the $R.S.$ from 0.1143 to 0.07928 , a decrease of 31% . However, this value of $R.S.$ did not reach the desired value of 0.01 . The bulges on the end wall were still present, seen in Figure 4.25. Another difference was the bottom wall nozzle geometry. The new simulated annealing solution produced a geometry on the bottom wall that did not constrict in the nozzle section of the domain, as well as a

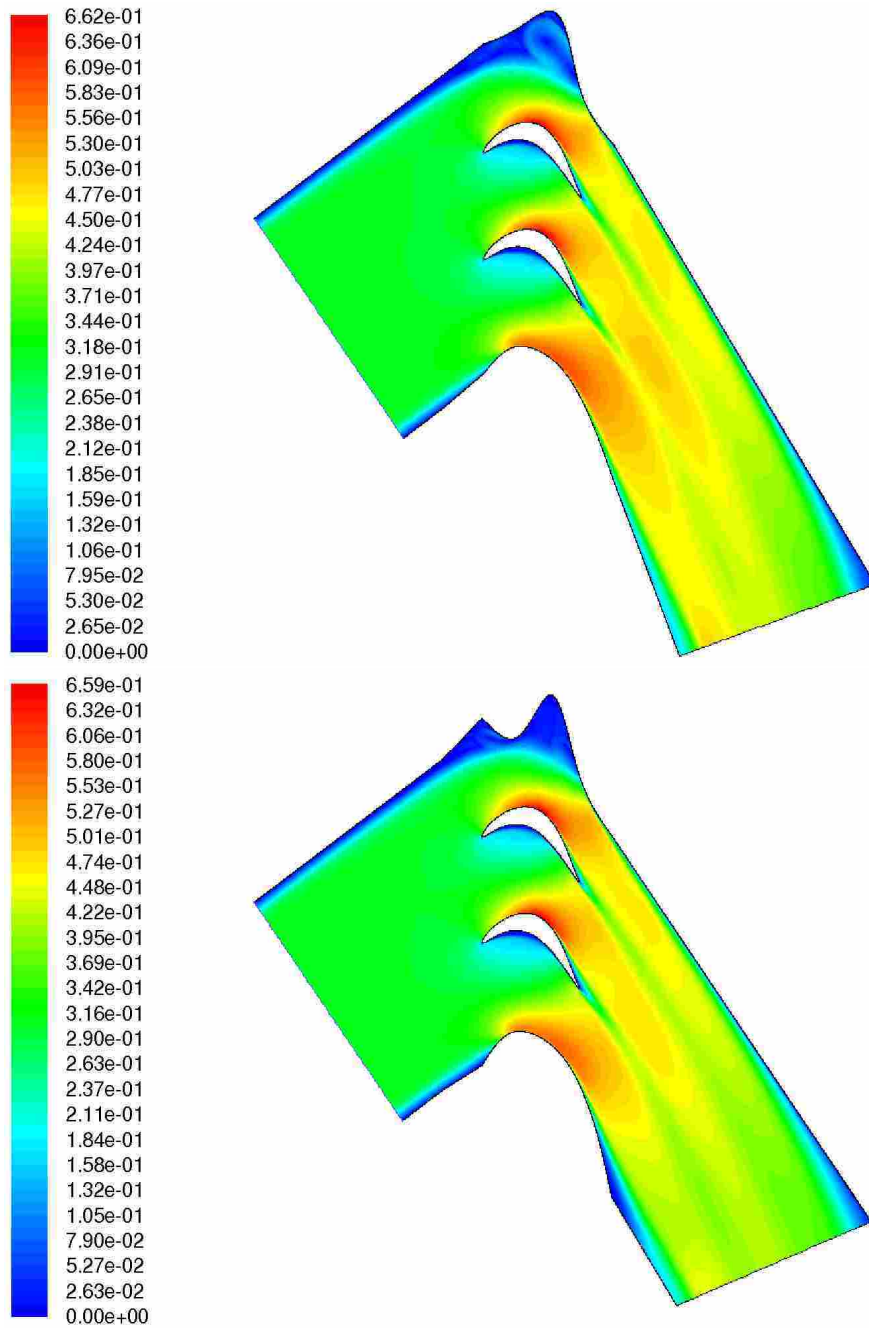


Figure 4.22: Tunnel geometry showing the end wall geometry of the tunnel and velocity magnitude contours for the narrow domain case using (top) the successive approximation, and (bottom) the simulated annealing optimization method.

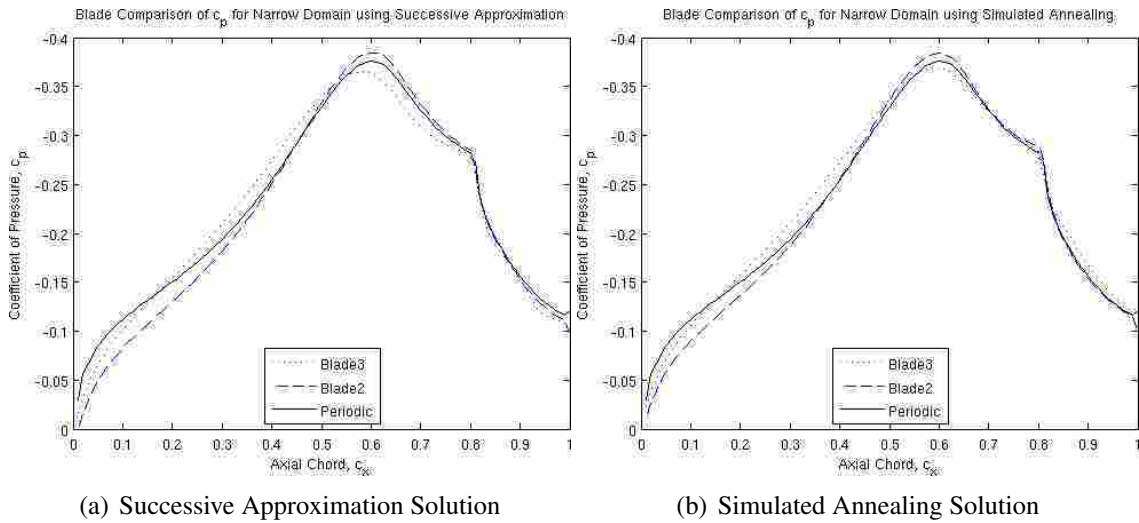


Figure 4.23: c_p distribution of the narrow domain using (a) the successive approximation optimization method and (b) the simulated annealing method.

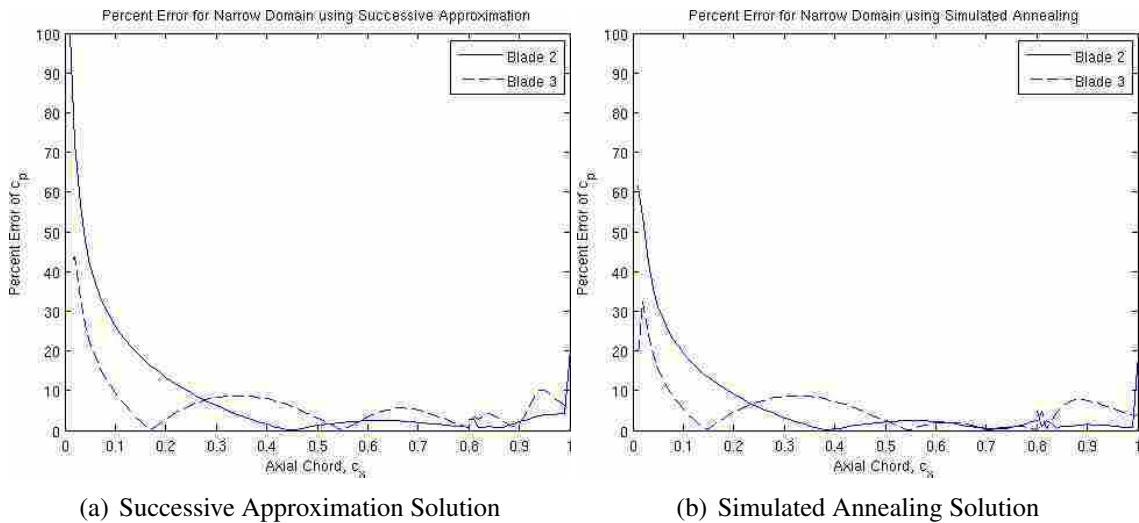


Figure 4.24: Percent error of both tunnel blades compared to periodic solution for the case of reduced width of the tunnel for (a) the successive approximation and (b) simulated annealing methods.

less pronounced separation zone at the transition from end wall to tailboard. It was also important in this case to compare velocity magnitude because of the direct relationship between Reynolds number and velocity. The simulated annealing had a lower magnitude of velocity resulting in lower c_p for both blades. This effect of the lower velocity can easily be seen in Figure 4.26

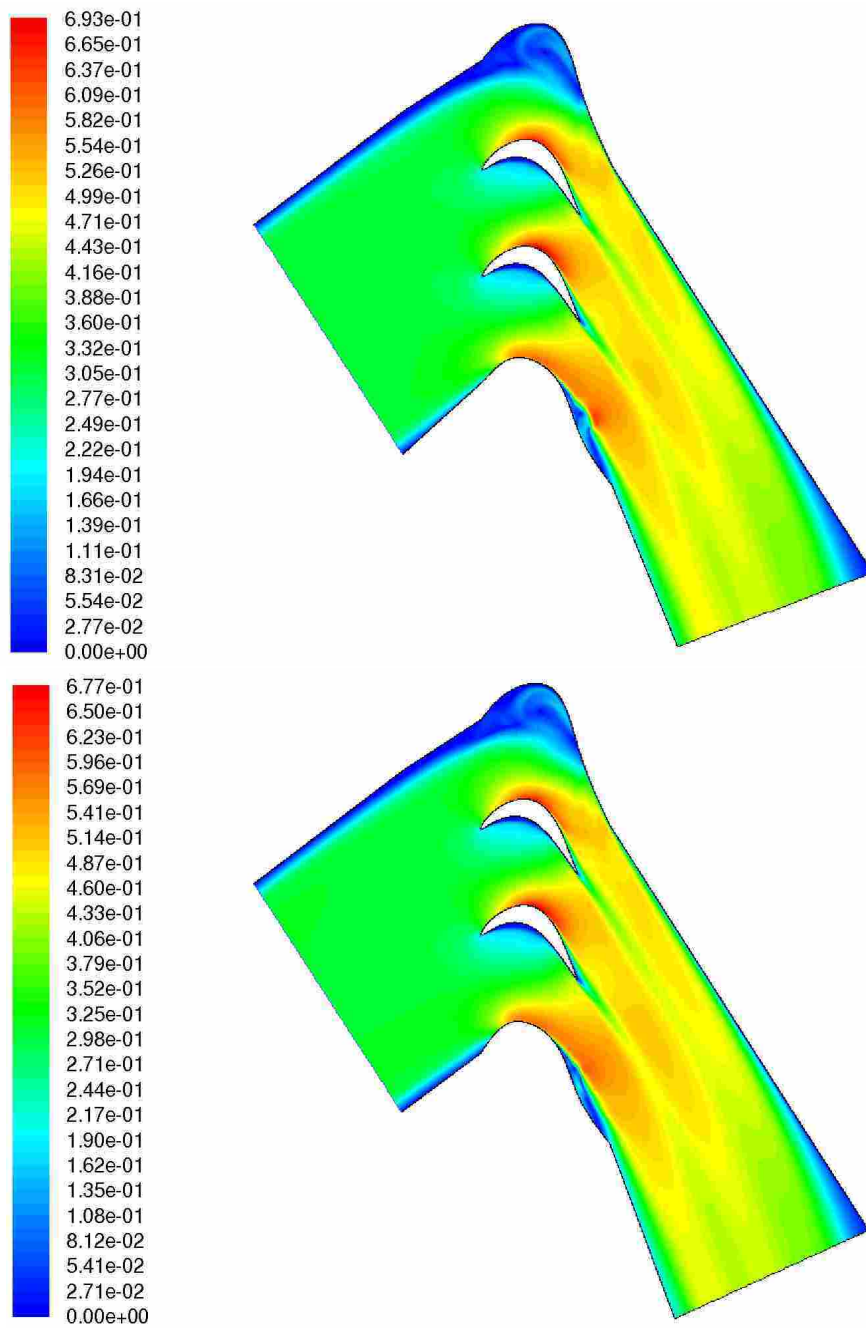


Figure 4.25: Tunnel geometry showing the large bulge on the pressure wall of the tunnel and velocity magnitude contours for the variable Reynolds number case for both the (top) successive approximation and (bottom) simulated annealing optimization solutions.

Both c_p distributions for blade 2 and blade 3 were reduced, blade 2 by 3.5% and blade 3 by 3%. The location of maximum c_p did not change from the successive approximation method. The percent error plots were very similar, however the simulated annealing generally had lower error over the domain with the exception of the entrance region of the blades. Based on these two simulations, simulated annealing was demonstrated to be an effective method for optimizing LPT flow fields. The results were very near to the desired $R.S.$, although not quite reaching the minimum threshold.

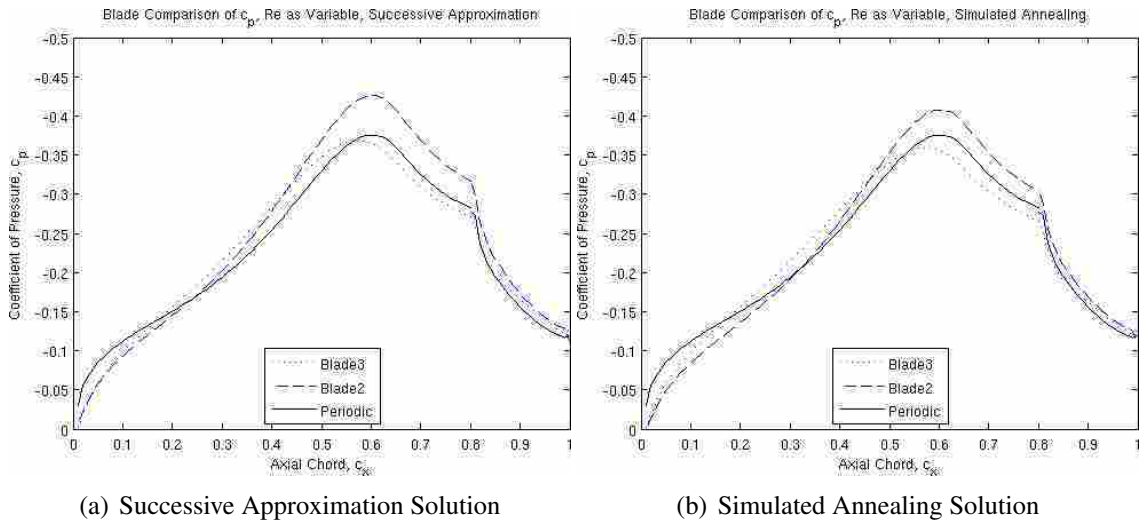


Figure 4.26: c_p distribution of the variable Reynolds number using (a) the successive approximation and (b) simulated annealing optimization methods.

Hooke-Jeeves Lengthened Nozzle

The wind tunnel configuration with the lengthened nozzle would be the simplest to implement in the actual tunnel because the inlet width is the same as the tunnel configuration and no other modifications would need to be made. For this reason, this domain was run using the Hooke-Jeeves optimization method. This method may still find local minima, however if care is taken to avoid local minima, this model can be very good in defining the domain geometry. The $R.S.$ was reduced to 0.0461 from 0.0498, only a 7.5% improvement. This improvement was barely visible in the associated plots. Figure 4.28 shows the domain and velocity magnitude contours. The main difference observed was the separation bubble located at the transition from end wall to tailboard was reduced.

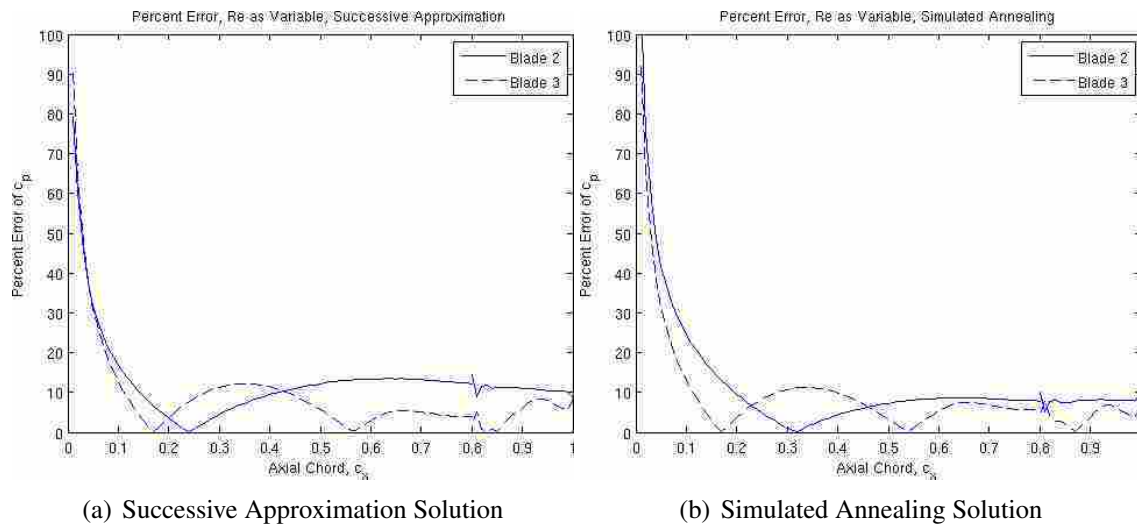


Figure 4.27: Percent error of both tunnel blades compared to periodic solution for the case of variable Reynolds number using (a) the successive approximation and (b) simulated annealing methods.

The c_p distribution for both blades improved in magnitude. Blade 3 matches the maximum exactly, while blade 2 improves by 0.01, as shown in Figure 4.29. The percent error also showed a slight improvement in the region from $0.5c_x$ to $0.82c_x$, shown in Figure 4.30. From 6% to 5% for blade 2 and 5% to 2.5% for blade 3. Again, the improvement gained by this run was not as much desired. It is possible that the solution was a local minimum instead of a global minimum. Further optimization runs would need to be performed when possible, to confirm that it is a local minimum.

Hooke-Jeeves Full Tunnel

The Hooke-Jeeves method was also tested with the full tunnel configuration. Although a minimally improved solution was found for the longer nozzle case using the Hooke-Jeeves method, a much improved solution was found for the full tunnel configuration. The $R.S.$ improved from 0.05656 to 0.017195, and represents an improvement of 70%. This configuration came closest to the desired minimum $R.S.$ of 0.01.

The large portion of the tunnel entering the test section, shown in Figure 4.31, still had a diffusive angle and the nozzle section constricting the flow. The geometry of the top end wall looks more like the previous cases of nozzle length and reduced tunnel width. This was different from the successive approximation solution in that it now has a sharp corner

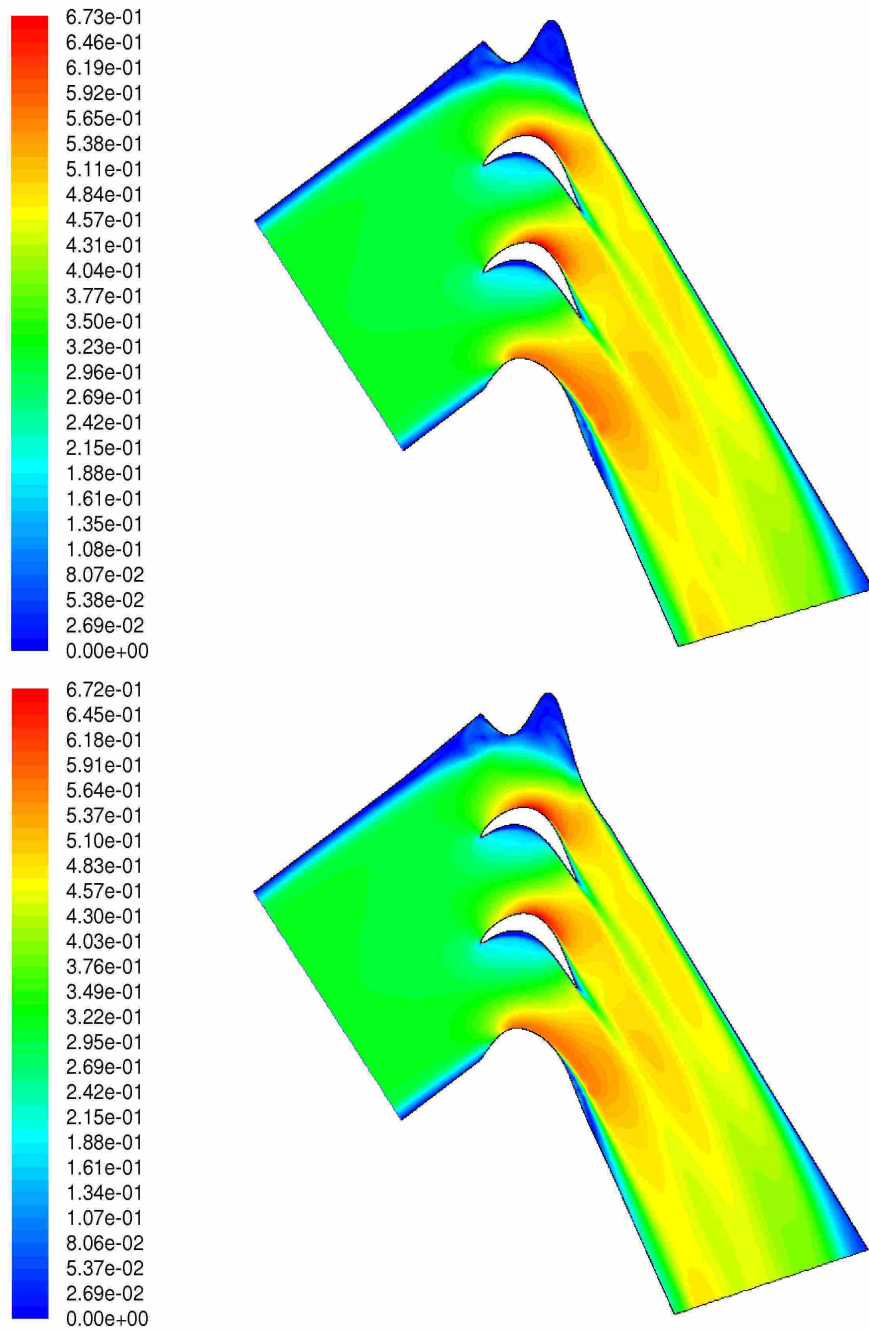


Figure 4.28: Tunnel geometry showing the end wall geometry and velocity contours of the optimized solution for the case of extended nozzle length using the (top) successive approximation and (bottom) simulated annealing optimization methods.

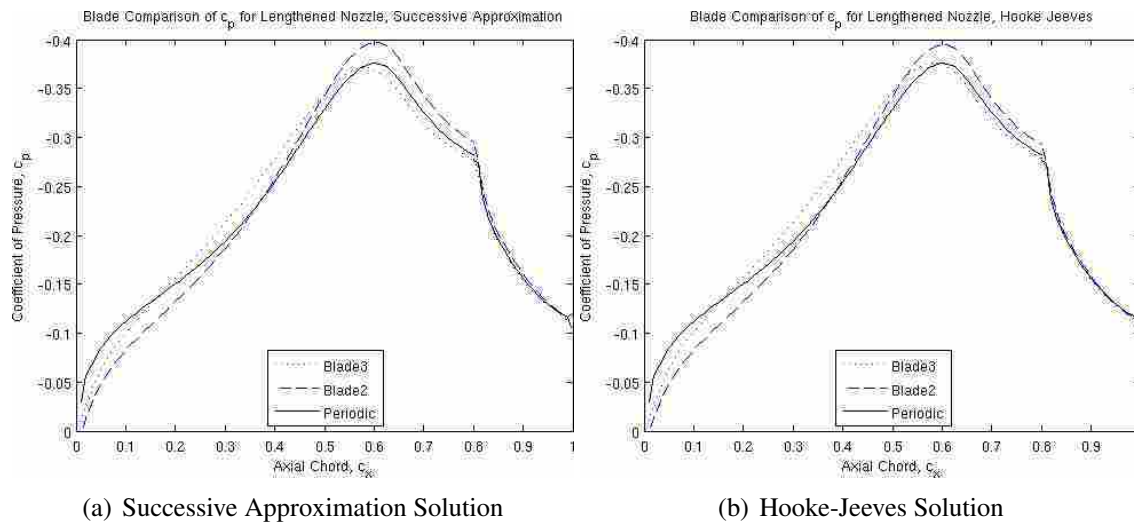


Figure 4.29: c_p distribution of the extended nozzle length case using (a) the successive approximation and (b) the Hooke-Jeeves optimization method.

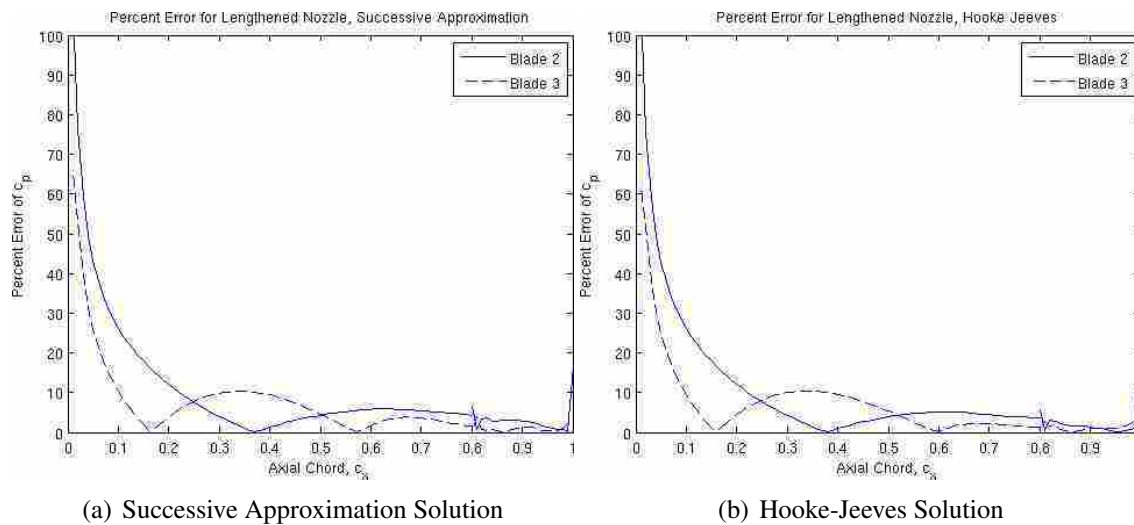


Figure 4.30: Percent error of both tunnel blades compared to periodic solution for the case of extended nozzle length entering the test section using (a) the successive approximation and (b) the Hooke-Jeeves optimization methods.

connecting the nozzle section and the end wall instead of a smooth transition, increasing the possibility of inaccurate results. The separation bubble on the bottom wall near the transition to the tailboard section was also much smaller, more accurately mimicking the momentum deficit left by the blade wakes.

The significant improvement in $R.S.$ was also shown by the c_p and percent error plots of Figures 4.32 and 4.33. The magnitude and location of the maximum c_p were very

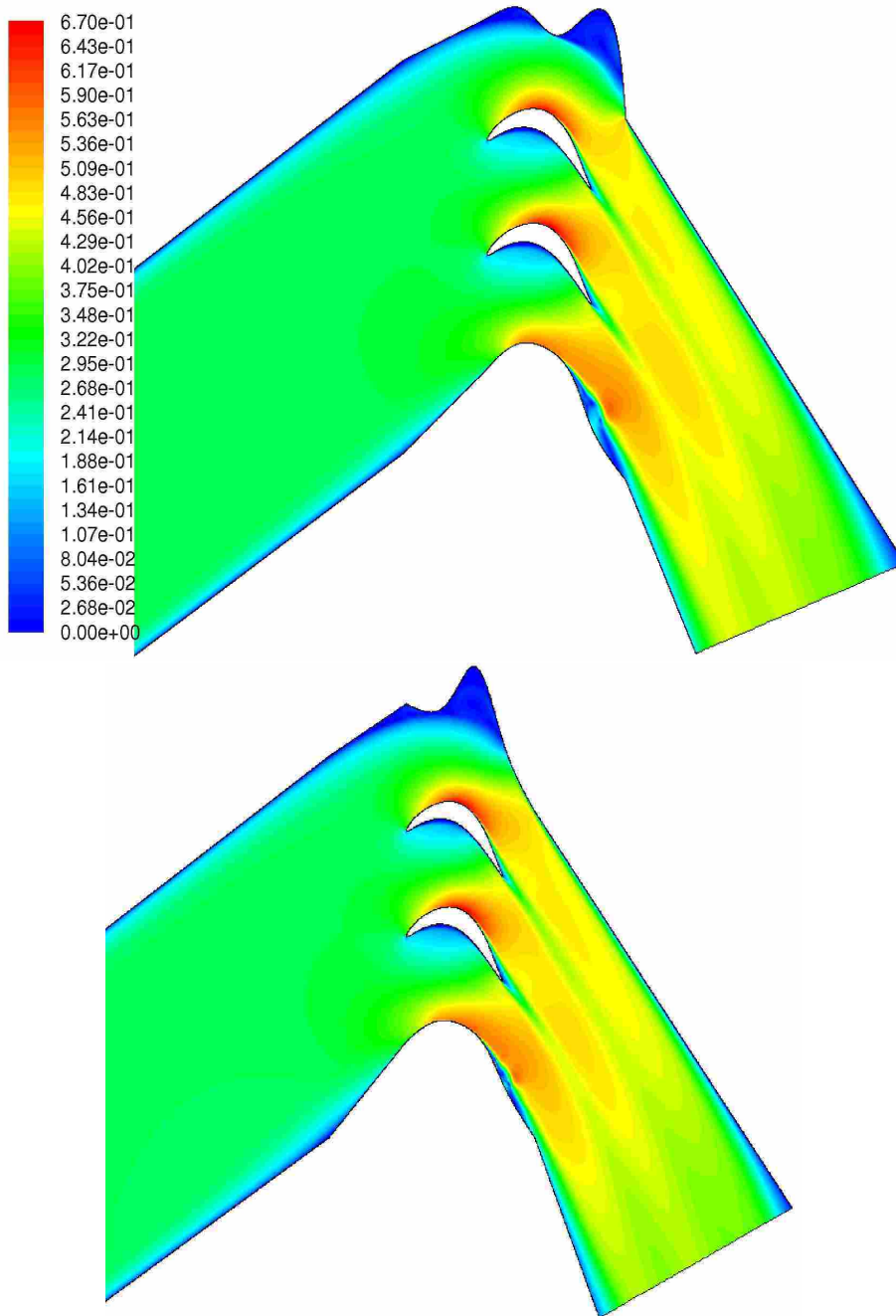


Figure 4.31: Characteristics of the test section geometry and velocity magnitude contours of the full tunnel case for the (top) successive approximation and (bottom) Hooke-Jeeves optimization methods

well predicted. The aft portion of the blade was also very close to the periodic solution. For this solution the only portion of the blade where the c_p was not close to the periodic solution was the entrance portion of the blade. The reason for which was discussed in Section 4.3.2.

The percent error of this section did improve over the successive approximation method, however, the error was still near 50% at the inlet. This improvement is significant, but still not as close as desired. The geometry of the top end wall is also undesirable. This geometry in all the previous solutions has been unavoidable. However, methods for smoothing the geometry were suggested by Laskowski [10].

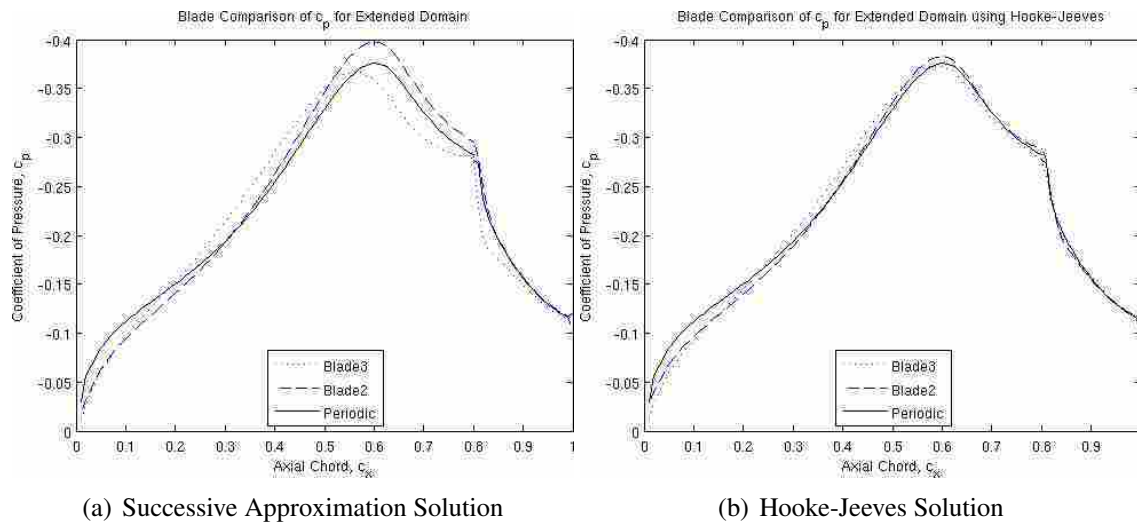


Figure 4.32: c_p distribution of the full tunnel using (a) the successive approximation and (b) the Hooke-Jeeves optimization methods.

4.3.8 Separating Streamline

The top wall geometry was similar to the initial solutions of Laskowski et al. [10] where a large recirculation zone exists in a bulged upper wall. One method presented in his work was to use the separating streamline between the recirculation zone and the remainder of the flow as the wall boundary. This method was implemented by Laskowski to achieve a very good solution and eliminated the undesirable geometry.

Figure 4.34 shows the domain and velocity contours of the full tunnel solution using the separating streamline as the upper wall geometry. In this case the wall geometry was not truly smooth. The dividing streamline was not smooth due to the dual circulation zones of the optimized full tunnel case seen in Figure 4.31. Defining the upper wall geometry with the dividing streamline did not produce the desired flow field. The $R.S.$ for this solution was

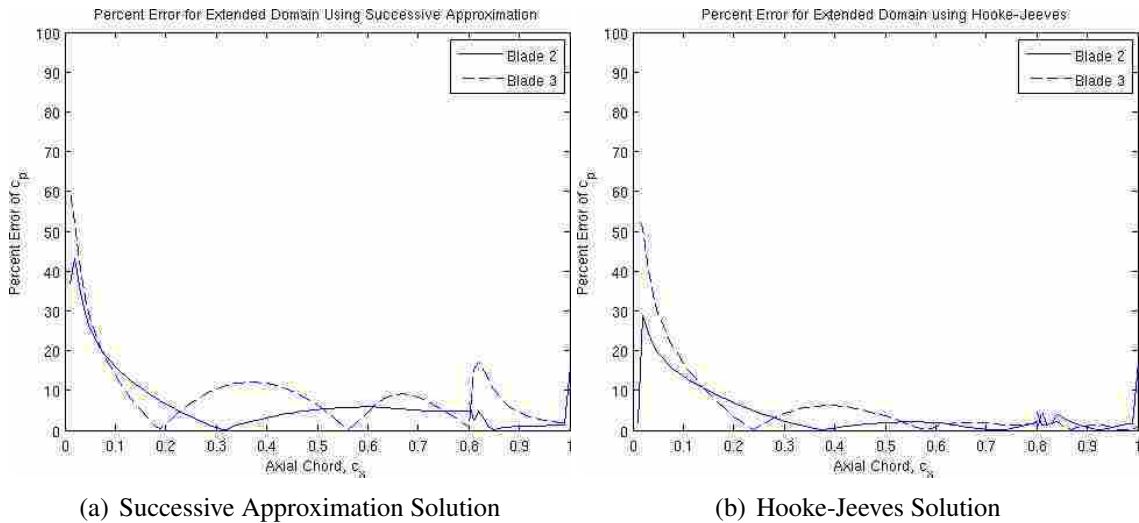


Figure 4.33: Percent error of both tunnel blades compared to periodic solution for the full tunnel case using (a) the successive approximation and (b) the Hooke-Jeeves optimization methods.

0.1281, much larger than all the previous experiments and 745% larger than the optimized solution from which the streamline was taken.

Based on the velocity magnitude contour plot, the results did not show any obvious abnormalities. However, the c_p and the percent error plot in Figures 4.35 and 4.36 show that the results were not acceptable. The c_p plot shows that the distribution was not smooth. This kind of behavior typically indicates an instability or a false flow feature caused by skewed elements of the domain that propagate throughout the domain. Considering there are no skew elements in the grid (checked using the Fluent grid checker), the cause for this unsteady behavior is due to some instability created by the domain geometry. Examples of possible instabilities are reversed flow on an outflow boundary or vortex shedding. Other than this odd behavior only blade 2 predicted the flow accurately at the maximum. The c_p of blade 2 then dropped down to match blade 3 at $0.8c_x$. Blade 3 c_p was 12% smaller than the periodic solution. The percent error plot in Figure 4.36 reiterates the inaccuracy of the solution.

A new end wall geometry was used for the separating streamline. The separating streamline used previously used the exact path of the flow, which unfortunately included rapid or sharp changes in direction. These sharp turns make the geometry unacceptable for manufacturing purposes and produced an unstable flow solution. The same streamline was

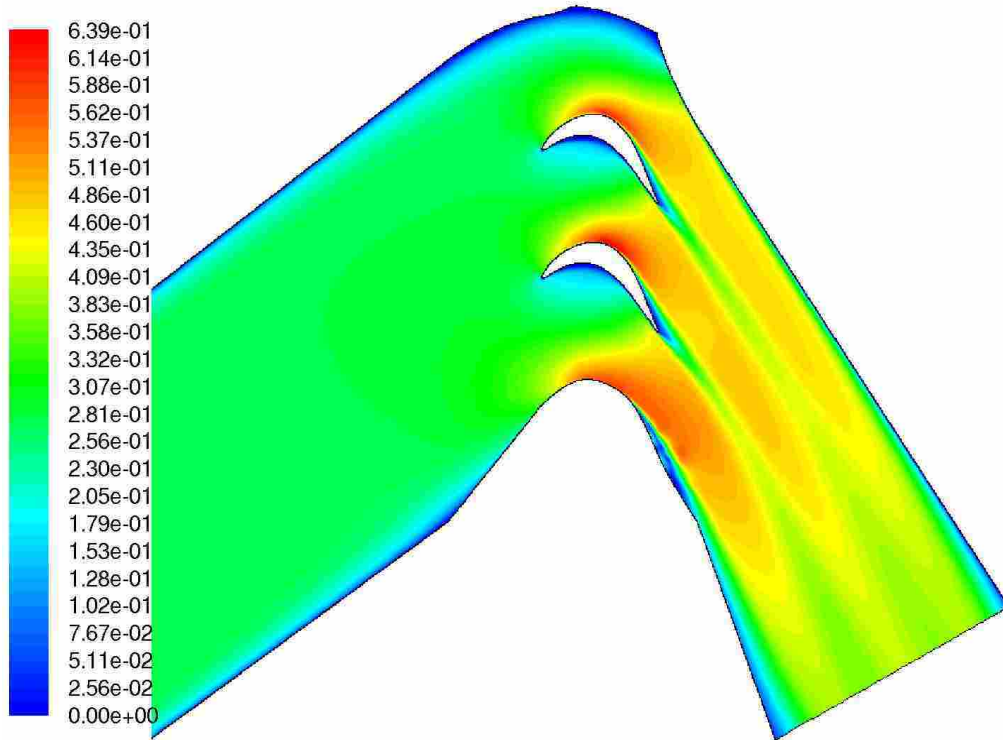


Figure 4.34: Tunnel geometry and velocity magnitude contours using the separating streamline end wall from the best Hooke-Jeeves extended tunnel case.

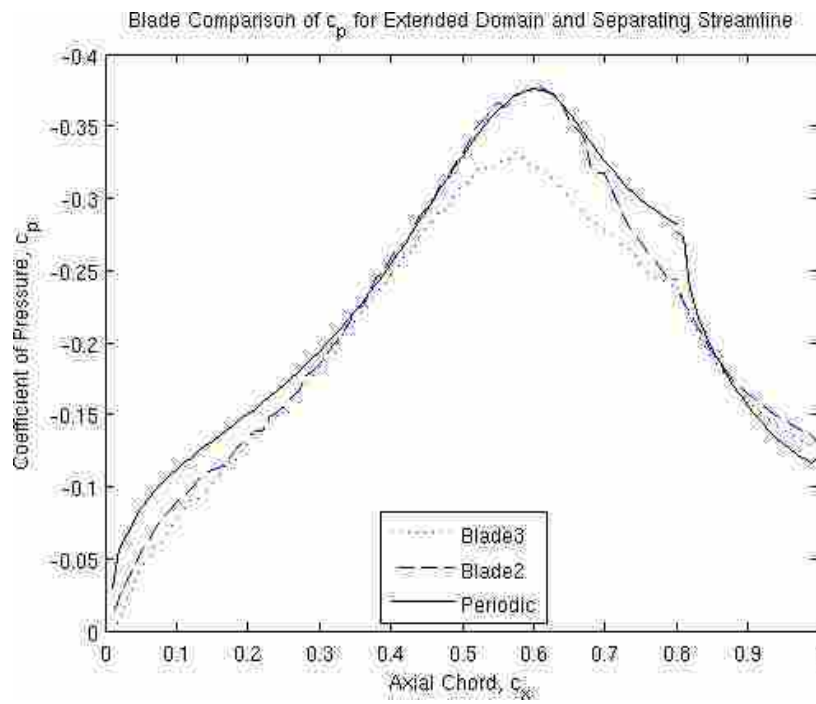


Figure 4.35: c_p distribution using the separating streamline end wall from the best Hooke-Jeeves extended tunnel case.

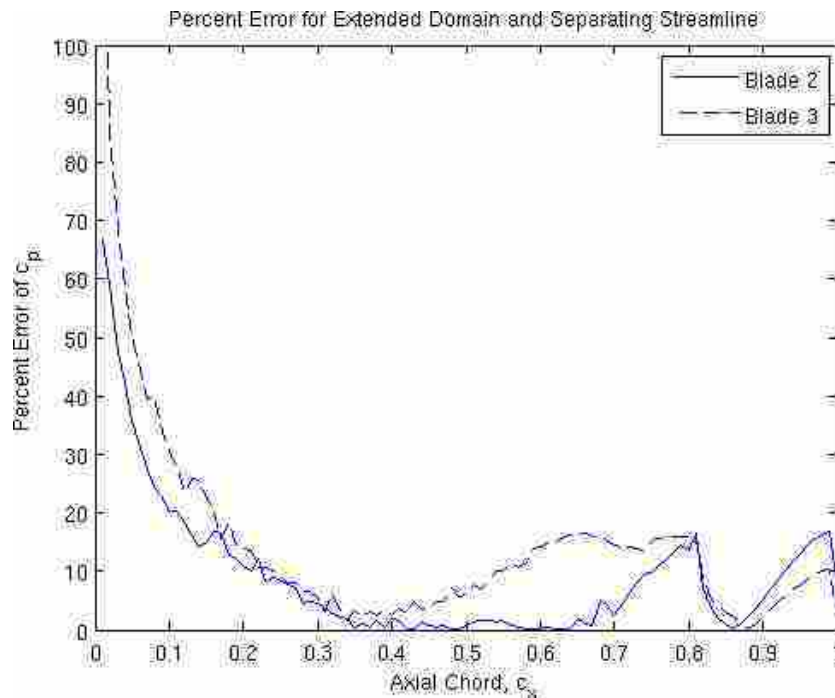


Figure 4.36: Percent error using the separating streamline end wall from the best Hooke-Jeeves extended tunnel case.

used for a second solution of the flow, however, it was smoothed out by fitting a spline to 9 evenly spaced points that were extracted from the original shape. This end wall geometry was then run using the same parameters as the previous solutions. The shape of the end wall can be seen in Figure 4.37. Notice the smoothness compared to Figure 4.34.

The solution of this new smooth domain resulted in a $R.S. = 0.0182$. This is only a 6% increase in $R.S.$ from the Hooke-Jeeves optimized solution of the full tunnel geometry. This is an acceptable increase in $R.S.$ to simplify the end wall geometry of the tunnel. The accuracy can be seen visually from the c_p distribution seen in Figure 4.38 and the percent error shown in Figure 4.39. Both plots show very similar solutions to the full tunnel Hooke-Jeeves optimization. The most evident improvement was the reduction of error introduced at the leading edge of the blades, reducing the error from 55% and 29% of the Hooke-Jeeves full tunnel, to 44% and 24% of the smooth separating streamline. This was another indication that the smoothness of the wall affected flow of the leading edge of the blade. The elimination of the complex end wall geometry is a significant improvement.

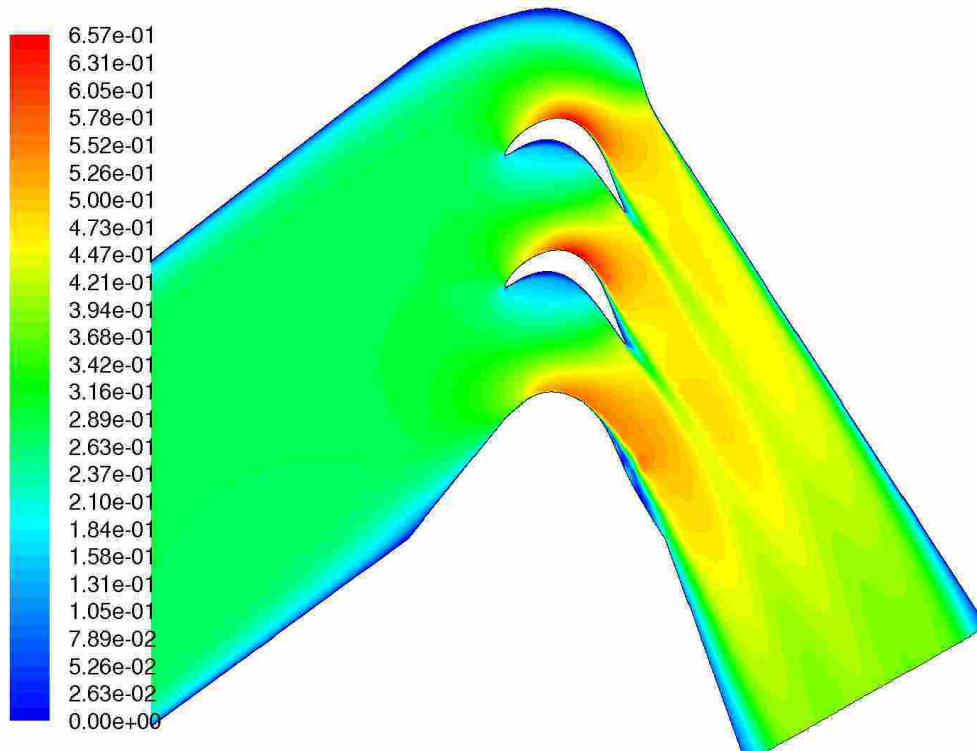


Figure 4.37: Tunnel geometry using the smooth separating streamline end wall from the best Hooke-Jeeves extended tunnel case.

4.4 Summary and Analysis

The optimization of the geometry is dependent on multiple inter-relating factors such as tunnel width, flow velocity, flow angle, blade position, blade spacing, tailboard diffusion, and end wall contour smoothness. All of these factors were controlled by the manipulation of the end walls. The optimization solutions acquired in this study have shown the effectiveness of some optimization techniques and the effect of some parameters on the solution. Table 4.2 shows the results of all the runs made. All the models were run using the successive approximation method of optimization. Four more runs of the same domain types were run using two different optimization algorithms. Optimization runs to complete Table 4.2 were unable to be performed due to computational resource limitations.

Two models, the narrower tunnel and variable Reynolds number models, were run using the simulated annealing optimization method. The improvements made by the simulated annealing method were significant for both models. The narrow tunnel improved

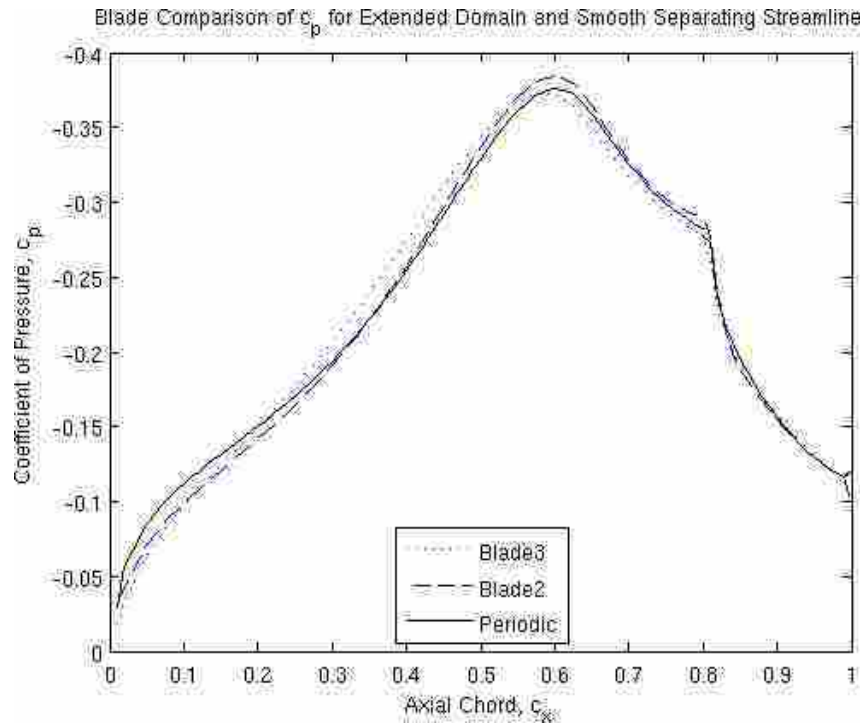


Figure 4.38: c_p distribution using the smooth separating streamline end wall from the best Hooke-Jeeves extended tunnel case.

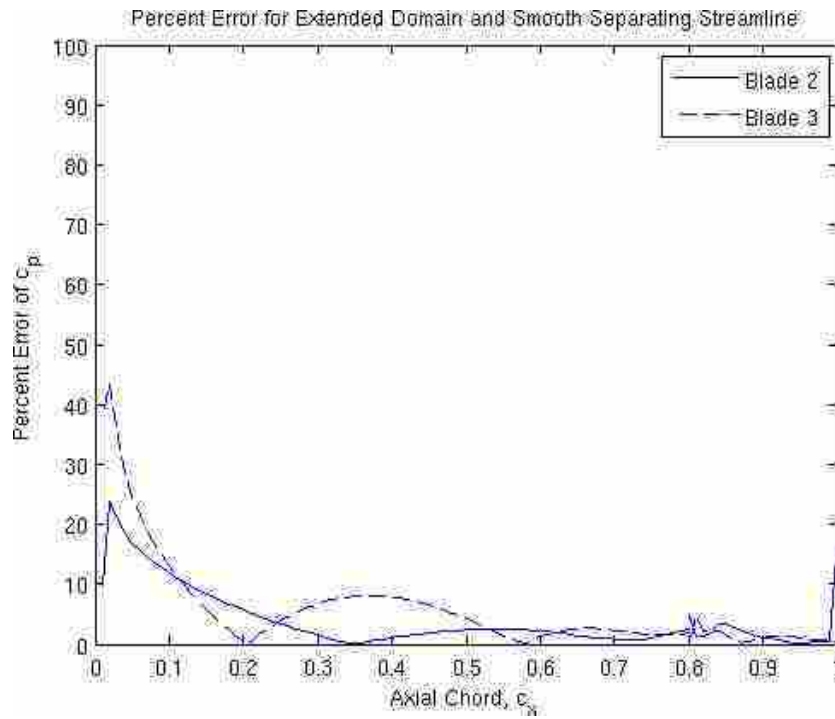


Figure 4.39: Percent error using the smooth separating streamline end wall from the best Hooke-Jeeves extended tunnel case.

by 38% over the original optimization case to a *R.S.* of 0.021 and the variable Reynolds number improved by 31% to a *R.S.* of 0.07928 over the original optimization.

Two models, the full tunnel and the lengthened nozzle domains, were run again using the Hooke-Jeeves method with relative success. The lengthened nozzle only improved by 7.5% over the original optimization and did not get close to the desired $R.S. \leq 0.01$. The full tunnel case improved significantly by 70% over the original optimization, and came much closer to the desired results with a *R.S.* of 0.017195. However, the geometry on the top end wall was not desired and the separating streamline method presented by Laskowski et al. [10] was used to eliminate the recirculation regions near the end wall.

Table 4.2: *R.S.* for All Optimization Cases

	Successive Approximation	Simulated Annealing	Hooke-Jeeves
Extended	0.05656	-	0.017195
Narrow	0.03368	0.021	-
Nozzle	0.0498	-	0.0461
Original	0.054	-	-
Reynolds	0.1143	0.07928	-

The variable Re optimization solution showed that the magnitude of the c_p distributions for the blades was dependant on the Re of the flow, as expected. This solution changed the velocity of the whole domain, instead of smaller portions of the flow throughout the domain. The decrease of the inlet Re from 20,000 to 15,550 reduced the mass flow rate, and reduced the need for the large recirculation. However, the improvement was only effective for blade 3. Blade 2 was not improved due to the fixed spacing between the blades. The narrow domain also decreased the amount of mass flow but kept Re=20,000. This domain resulted in the best solution for the successive approximation.

Improvements in *R.S.* were also made by changing the flow velocity in certain locations. This was demonstrated by altering the end wall geometry to create constricting and diffusing sections along the blade. The velocity changes resulted from an accelerating flow through a nozzle, or a decelerating flow from diffusion. These changes in geometry

are displayed in the complex form of the end walls, as seen in the velocity contour plots of Figures 4.22 4.25 4.28 and 4.31, where the constricting and diffusing sections are obvious.

The full tunnel cases showed that the tunnel got wider as it approached the test section, keeping the interior velocity profile flat and the same magnitude as the inlet. The nozzle then constricted the flow reducing the size of the boundary layer. The end wall solutions still showed a complex geometry, indicating accelerating and decelerating flow. The results were very good for the Hooke-Jeeves method and shows that the more geometry controlled by the optimization results in a better solution, although at three times the computational cost.

The $\%c_x$ location of maximum c_p was only dependent on the incoming flow angle. An increased flow angle shifts the maximum c_p forward, while a decreasing flow angle shifts the maximum downstream. The design of the wind tunnel cascade affects the incoming flow angle. The flow angle changes were due to the boundary layer and nozzle section of the tunnel geometry turning the flow. These flow angle differences can be controlled by manipulating the end walls of the tunnel, more specifically, the nozzle section of the tunnel. The extended nozzle case showed that a more gradual constriction due to the longer nozzle improved results. The farther upstream the flow can be altered, the better the c_p profile will match the periodic solution.

In all the optimization runs the maximum percent error was found at the beginning of the blade and decreased toward the blade trailing edge, making the prediction of c_p 's easier as the flow moves downstream. This was partly due to the size of the c_p being so small at that location making the percent error greater. The limited ability of the nozzle to create the needed flow characteristics at the blade row inlet plane was the main factor for creating error at the beginning of the blades. The longer nozzle and narrow cases showed improvement in minimizing the *R.S.* at the inlet plane of the blades, as did the full tunnel solution. The main differences between these cases was that the changes were made upstream of the inlet plane of the blades. The smooth end walls of the full tunnel solution using the successive approximation method also helped reduce the percent error. Due to the improvement of the full tunnel and the extended nozzle cases, it is hypothesized that if the nozzle portion of the tunnel was included in the end wall spline to create a

smooth transition and extended farther upstream, the c_p of the entrance region would be improved and result in a much better solution. Further numerical simulations would need to be performed to prove this hypothesis.

The three methods of optimization used, successive approximation, simulated annealing, and Hooke-Jeeves, can all be used in the design of LPT components. The successive approximation method, because it was gradient based, often found a local minimum instead of the optimum. This was acceptable if only an improvement in $R.S.$ was needed, which was the case for most commercial applications. To find a true optimum, a different method should be used. The Hooke-Jeeves method was a good method to use because it was less sensitive to local optima, although the possibility of getting stuck on a local optimum still exists. This method proved to be useful in this experiment and provided the best solution. However, in an industrial application where an improvement is desired in the smallest amount of time this method may be temporally expensive. The simulated annealing method showed more consistent improvement than the Hooke-Jeeves. While the Hooke-Jeeves method was still prone to finding only local minima, the simulated annealing was able to distinguish between local minima to find a global minimum. This method was also computationally expensive. In the optimization runs, the Hooke-Jeeves and simulated annealing methods needed three times as many iterations to achieve a solution. All three methods have shown improved results for this turbomachinery case. The adaptive simulated annealing method was the better method between the three discussed for finding a true optimum in this turbomachinery application.

All the optimized solutions resulted in an end wall geometry that was undesirable. A simple end wall geometry is needed to efficiently build a test section using the acquired end wall solutions. It was found that a smooth streamline separating the recirculation caused by the end wall and the bulk flow could be used as a new modified end wall geometry. This change resulted in a 6% increase in $R.S.$ from the Hooke-Jeeves full tunnel solution, where $R.S. = 0.0182$. This was the best solution obtained for this problem due to the low $R.S.$ and the smooth end wall geometry. The optimized domain compared to the initial domain is shown in Figure 4.40. The optimized c_p compared to the initial c_p is shown in Figure 4.41.

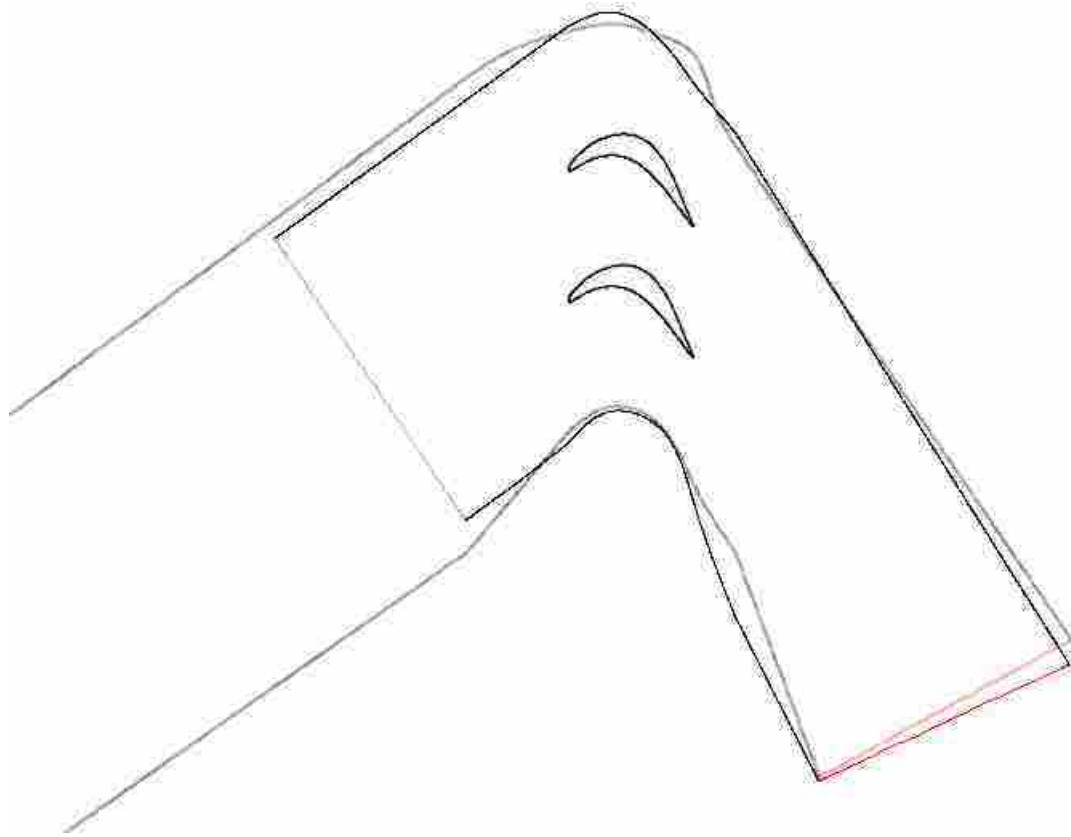


Figure 4.40: Optimized tunnel domain using the smooth separating stream line compared to the initial optimization domain.

The design of experimental periodic linear cascades for low Reynolds number LPT blades can be designed accurately. The combination of CFD and optimization techniques result in varying degrees of design accuracy depending on the methods and domains used. The use of the CFD model of Chapter 2 is limited due to the inherent error of the process as described in Section 4.2, but can be used as the desired result of the optimization. The optimization methods using iSIGHT, Gambit, Fluent, and Matlab have been successful in predicting a solution within the error of the CFD model. These results could be improved by extending the smooth spline end wall section to include the extended nozzle, as well as continuing the optimization process with the adaptive simulated annealing method. The method of using computational methods to design these experimental facilities has shown to be shown to be successful and promising for future experiments.

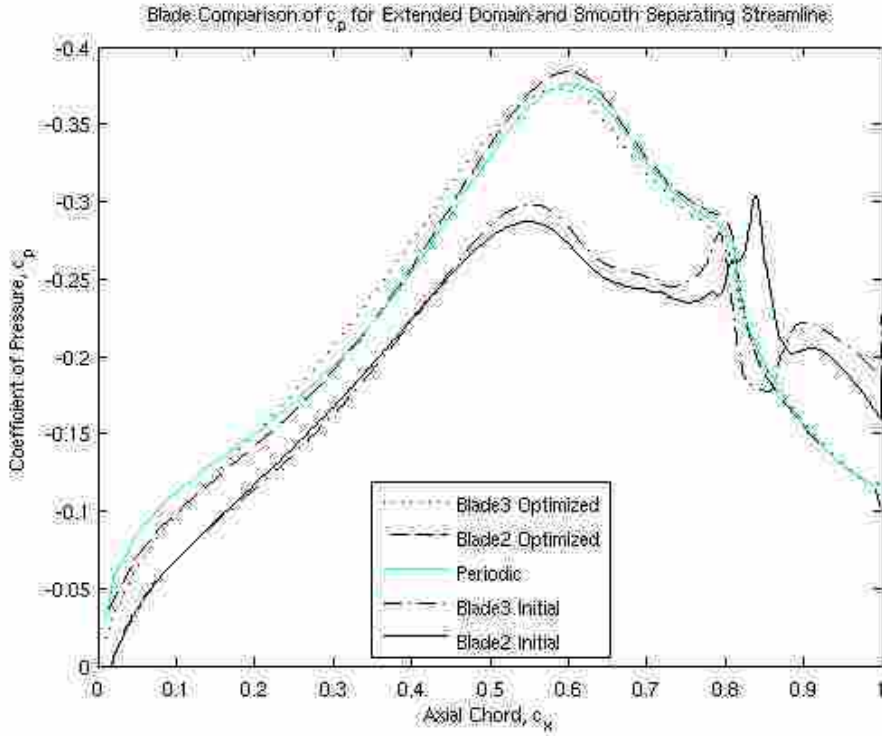


Figure 4.41: Optimized tunnel c_p using the smooth separating stream line compared to the initial domain c_p .

4.4.1 Recommendations

It is difficult to create periodic flow conditions in LPT linear cascades because the tunnel wall boundary layer alters the incoming flow field in such a way that the c_p of the blade nearest the wall changes. Due to the altered velocity profile, the change could increase the c_p if the spacing between the wall and blade is large, or decrease if the spacing between the wall and blade is small. The c_p change in one blade propagates through the rest of the cascade, eliminating any periodicity that may have existed.

This research has shown that the end wall contours of the cascade can be optimized to improve periodic flow through the passage. Specifically, changing the tunnel wall spacing, including a nozzle, and changing the end wall contours can create periodic flow through the passage. Changing the tunnel wall spacing reduces the flow rate through the tunnel. Because less mass flows through the tunnel, not as much mass needs to be bled resulting in a decreased amount of diffusion and recirculation needed to match the c_p distribution. The nozzle increases the velocity of the flow field because of conservation of

mass and a reduced area, and the uneven constriction of the top and bottom nozzle walls turns the flow. The increased velocity caused by the nozzle, increases the c_p distribution. The turning caused by the nozzle changes the blade row inlet flow angle. The increase of inlet flow angle shifts the maximum c_p upstream, and a decreased flow angle shifts it downstream. The wall contours allow more local changes to the flow field. Conservation of mass explains the decreased velocity for diffusion and increased velocity for constriction. The resulting end wall contours of the optimizations showed obvious diffusing and constricting portions of the end wall, increasing and decreasing the velocity where needed to match the periodic c_p distribution.

Future optimization runs should be run to complete Table 4.2. The completion of these runs are expected to further refine the analysis of the optimization methods used. The optimization of the extended nozzle domain could also be improved and a separating streamline for this domain used as the end wall. This would result in a simpler design to build for the wind tunnel experiments. The straight sections of the tunnel, such as the nozzle and tail board sections, could be included in the spline defining the end wall geometry. This could reduce the minimum residual sum of the optimization runs by smoothing the tunnel.

Chapter 5

Summary & Conclusions

5.1 CFD Model

A method of modeling low Re flows over turbine blades that experience separation and a transition to turbulence was obtained. This method involves using an initial laminar solution in a periodic domain to obtain the needed parameters to calculate a turbulence transition location. The location of transition was calculated using an empirical transition model developed by Praisner and Clark [14]. The transition location was then modeled by a physical split in the domain to create laminar and turbulent zones. This method to create a solution for transitioning flow over LPT blades has given results accurate to an $R.S. \leq 0.13$. One downside to this method was the requirement of hand calculations to define the transition location.

5.2 Mesh Manipulation

A set of guidelines were found to better understand how domain characteristics effect the flow field and c_p distributions of the suction surfaces of the blades. The three domain characteristics studied were tunnel wall spacing, tailboard effect, and position of the blades. These three characteristics were believed to be the main factors in altering the flow field. The effects of these characteristics are as follows.

The increase in wall spacing decreased the c_p by reducing the velocity over the blade. Decreasing the wall spacing increased the c_p due to an increased velocity. However, the velocity decreases if the spacing was made too small due to the domination of viscous effects in the flow. Because the flow was a low Re flow, the effect of downstream characteristics can greatly influence upstream flow. The changes made in tail board geometry allowed for only diffusion to occur. This diffusion of a low Re flow resulted in a lower c_p

distribution and moved the peak c_p in the horizontal direction. The shifting of the blades forward and up moved the blades into a cleaner air flow, with less boundary layer effect on the lower blade 2. The velocity was increased for both blades and results in an increased c_p . The location of peak c_p for blade 2 was also pushed downstream due to cleaner inlet flow.

5.3 Optimization

The optimization was done using the CFD method of manually initiating turbulence transition from Chapter 2 to obtain the c_p distribution of the periodic blade. The c_p of the periodic blade was then used as the optimization goal. The program iSIGHT was used to do the optimization with its built in optimization techniques and its capability to use Fluent, Gambit, and Matlab in the optimization routine. The cost function used for the optimization was a residual sum calculation as shown below.

$$R.S. = \sum((c_{p1i} - c_{p2i})^2 + (c_{p1i} - c_{p3i})^2) \quad (5.1)$$

The results of minimizing the residual sum was shown in Table 4.2. The best solution according to the optimization techniques performed was the full tunnel case using the Hooke-Jeeves optimization method. This resulted in a residual sum of 0.017195. However the desired minimum threshold for the residual sum was less than 0.01. Of the three optimization methods, the simulated annealing resulted in a more consistent improvement, reducing the $R.S.$ of both cases run by over 30%. The Hooke-Jeeves method improved the full tunnel case by 70% and the extended nozzle by 8%. The successive approximation resulted in good results, however, it was unable to reach the desired minimum $R.S.$. The simulated annealing was more consistent and would be considered a preferred method, while the Hooke-Jeeves method had the potential to give good results.

Some regions of the blade were easier to match to the desired periodic solution. The tail section of the blades where turbulent flow exists was the easiest to match. The mid section of the blade where the maximum c_p was found was the next easiest. This portion of the blade was more difficult because the difference in incoming flow angles changed the location of the maximum c_p . This difficulty originated from the nozzle turning the flow as it entered the blade passage. The most difficult portion to match was the leading edge of

the blade. The c_p 's never achieved the curvature of the periodic solution. The inability of the optimization to match the leading edge c_p 's to the periodic solution was a result of a straight nozzle. When the smooth separating streamline was used the error of the leading edge of the blade was reduced by 10%.

The optimization of the geometry was dependent on multiple inter-relating factors such as tunnel width, flow velocity, flow angle, blade position, blade spacing, tailboard diffusion, and end wall smoothness. All of these factors were controlled by the manipulation of the end walls. The manner the end walls were manipulated also effected the quality of the results. It was found that smooth end walls and the farther extent of the manipulated region (upstream and down), resulted in better results. The optimized geometry showed complex end wall behavior that was undesirable, creating recirculation regions along the end wall. An extra case was run using a smoothed separating streamline of the best solution as the end wall geometry. This attempt to simplify the end wall successfully provided a smooth end wall geometry that was near the desired threshold of $R.S. \leq 0.01$ at $R.S. = 0.0182$. This has proven to be a successful method for designing experimental periodic LPT linear cascades and the definition of the domain can be found in the Appendix.

This full tunnel geometry would not be an easy change for the current tunnel design as it requires rebuilding the tunnel. Therefore the easiest solution for the current wind tunnel facility, was the lengthened nozzle solution whose minimized $R.S.$ was only 0.0461. A further improvement could be made by including the nozzle section of the tunnel as part of the end wall spline to remove the straight edges and corners. This improvement would still need to be proven. Other runs could be made to improve the understanding of the optimization methods by filing all the spaces in Table 4.2.

This study was limited to only CFD simulations and requires further study and validation. The CFD model developed in Chapter 2 was based on matching simulations to experimental results. For this reason the CFD model cannot be any better than the experiment. The optimization was limited to the accuracy of the results of the CFD model. For this reason it was difficult to know if the optimized result was better than the previous experimental method for obtaining periodic conditions in the two passage cascade. The only way to truly optimize the wind tunnel geometry and improve the experiment would be to

do a higher level of iterations, including the computational optimization and experimental validation of the design. Once the computations result in the same flow field for the experiment the iterations can cease.

5.4 Continuation and Improvement

The CFD model used in this work could be completely replaced with the transition models recently added to the Fluent Beta version 12.0.7. Depending on the accuracy of the models, the pitfalls of the manual turbulence transition could be avoided, and a more accurate solution obtained. Optimization runs to complete Table 4.2 to improve understanding of the different optimization methods. An improvement in the lengthened nozzle domain could also be made. The straight edges of the nozzle and tailboard sections could also be included in the end wall spline to improve the smoothness of the domain. This research includes only computational simulations and lacks validation of the results with experiments. The validation of the results in an experiment should be done.

References

- [1] J. Bons, R. Sondergaard, and R. Rivir, “The Fluid Dynamics of LPT Blade Separation Control Using Pulsed Jets,” *ASME Journal of Turbomachinery*, vol. 124, pp. 77–85, January 2002.
- [2] R. Rivir, R. Sondergaard, J. Bons, and J. Lake, “Passive and Active Control of Separation in Gas Turbines,” no. 2000-2235. Denver, Colorado: AIAA Fluids, June 2000.
- [3] J. Bons, D. Reimann, and M. Bloxham, “Separated Flow Transition on an LP Turbine Blade with Pulsed Flow Control,” no. GT2006-90754. Barcelona, Spain: ASME Turbo Expo 2006: Power for Land, Sea, and Air, May 2006.
- [4] R. Volino, “Passive Flow Control on Low Pressure Turbine Airfoils,” *ASME Journal of Turbomachinery*, vol. 125, no. 4, pp. 754–764, 2003.
- [5] S. V. Patankar, *Numerical Heat Transfer and Fluid Flow*, 1st ed. New York, NY: Taylor and Francis, 1980, vol. 1.
- [6] J. Bons, L. Hansen, J. Clark, P. Koch, and R. Sondergaard, “Designing Low-Pressure Turbine Blades with Integrated Flow Control,” no. GT2005-68962. Reno, Nevada: IGTI, June 2005.
- [7] P. Kodzwa, C. Elkins, and J. Eaton, “Measurements of Film Cooling Performance in a Transonic Single Passage Model.” Zambia: 2nd Intl. Conference on Heat Transfer, Fluid Mechanics, and Thermodynamics, 2003.
- [8] A. Gross and H. Fasel, “Investigation of Low-Pressure Turbine Separation Control,” no. AIAA 2007-520. Reno, Nevada: 45th AIAA Aerospace Sciences Meeting and Exhibit, January 2007.

- [9] ———, “Active Control of Separation for Low-Pressure Turbine Blades,” no. AIAA 2004-2203. Portland, Oregon: 2nd AIAA Flow Control Conference, June 2004.
- [10] G. Laskowski, A. Vicharelli, G. Medic, C. Elkins, J. Eaton, and P. Durbin, “Inverse Design of and Experimental Measurements in a Double Passage Transonic Turbine Cascade Model,” *ASME Journal of Turbomachinery*, vol. Vol 127, pp. 619–626, July 2005.
- [11] J. Clark, “An Integrated Design, Analysis, and Optimization System for Turbine Airfoils,” 2004, AFRL Internal Report.
- [12] D. Reimann, M. Bloxham, K. Crapo, J. Pluim, and J. Bons, “Influence of Vortex Generator Jet-Induced Transition on Separating Low Pressure Turbine Boundary Layers,” *AIAA Journal of Propulsion and Power*, vol. 2007, no. 5, pp. 996–1006, Sep-Oct 23.
- [13] J. Vandoormall and G. Raithby, “Enhancements of the SIMPLE Method for Predicting Incompressible Fluid Flows,” *Numerical Heat Transfer*, vol. 7, pp. 147–163, 1984.
- [14] T. J. Praisner and J. Clark, “Predicting Transition in Turbomachinery, Part 1-A Review and New Model Development,” no. GT-2004-54108. ASME, 2004.
- [15] R. Eldredge, “Active Control of a Separating Boundary Layer with Steady Vortex Generating Jets: Detailed Flow Measurements,” Master’s thesis, Brigham Young University, 2004.
- [16] T. Ray and H. Tsai, “Swarm Algorithm for Single and Multi-objective Airfoil Design Optimization,” *AIAA*, vol. 42, no. 2, pp. 366–373, February 2004.
- [17] K. Ashihara and A. Goto, “Turbomachinery Blade Design using 3D Inverse Design Method, CFD, and Optimization Algorithm,” *ASME*, no. 2001-GT-0358, 2001.
- [18] Staff, “ISIGHT Reference Manual,” 2008, Engineous Solutions Inc. Software Reference.
- [19] C. Kelley, *Iterative Methods for Optimization*, S. E. Board, Ed. Philadelphia, Pa: Society for Industrial and Applied Mathematics, 1999.

- [20] S. Miyata and T. Kato, “Design Optimization with Commercial Software: Example and Issues.” Kobe International Conference Center, Japan: International Conference on Optimization: Techniques and Applications, December 2007.

Appendix A

Resources

A.1 Sample Matlab Code

```
clear all
[x1a,cp1a]=textread('Pressure1a.xy','%f %f','delimiter',' ') ,
'headerlines',4);
[x2a,cp2a]=textread('Pressure2a.xy','%f %f','delimiter',' ') ,
'headerlines',4);
[x3a,cp3a]=textread('Pressure3a.xy','%f %f','delimiter',' ') ,
'headerlines',4);
[x1b,cp1b]=textread('Pressure1b.xy','%f %f','delimiter',' ') ,
'headerlines',4);
[x2b,cp2b]=textread('Pressure2b.xy','%f %f','delimiter',' ') ,
'headerlines',4);
[x3b,cp3b]=textread('Pressure3b.xy','%f %f','delimiter',' ') ,
'headerlines',4);

i1a=length(x1a);
i1b=length(x1b);
i2a=length(x2a);
i2b=length(x2b);
i3a=length(x3a);
i3b=length(x3b);

x1a(i1a)=[];
x1b(i1b)=[];
x2a(i2a)=[];
x2b(i2b)=[];
x3a(i3a)=[];
x3b(i3b)=[];

cp1a(i1a)=[];
cp1b(i1b)=[];
cp2a(i2a)=[];
cp2b(i2b)=[];
```

```

cp3a(i3a)=[];
cp3b(i3b)=[];

x1ai=0.01:.01:0.80;
cp1ai=spline(x1a,cp1a,x1ai);
x1bi=0.8:.01:1;
cp1bi=spline(x1b,cp1b,x1bi);

x2ai=0.01:.01:0.80;
cp2ai=spline(x2a,cp2a,x2ai);
x2bi=0.8:.01:1;
cp2bi=spline(x2b,cp2b,x2bi);

x3ai=0.01:.01:0.80;
cp3ai=spline(x3a,cp3a,x3ai);
x3bi=0.8:.01:1;
cp3bi=spline(x3b,cp3b,x3bi);

figure (1)
plot(x3ai,cp3ai,'b',x2ai,cp2ai,'g',x1ai,cp1ai,'r',x3bi,cp3bi,
'b',x2bi,cp2bi,'g',x1bi,cp1bi,'r');

legend('Blade3','Blade2','Periodic','location','south');
axis([0,1,-.4,0]);
set(gca,'YDir','reverse');
title('Blade Comparison of c_p for Extended Domain');
xlabel('Axial Chord, c_x');
ylabel('Coefficient of Pressure, c_p');

L=length(cp1ai);
l=length(cp1bi);

St3ai=0;
for i=1:L-1
    St3ai=St3ai+(cp3ai(i)-cp1ai(i))^2;
end

St2ai=0;
for i=1:L-1
    St2ai=St2ai+(cp2ai(i)-cp1ai(i))^2;
end

```

```

St3bi=0;
for i=1:l-1
    St3bi=St3bi+(cp3bi(i)-cp1bi(i))^2;
end

St2bi=0;
for i=1:l-1
    St2bi=St2bi+(cp2bi(i)-cp1bi(i))^2;
end

Rsquared=St2ai+St3ai+St2bi+St3bi

percenterror2a=abs(cp2ai-cp1ai)./abs(cp1ai);
percenterror2b=abs(cp2bi-cp1bi)./abs(cp1bi);
percenterror3a=abs(cp3ai-cp1ai)./abs(cp1ai);
percenterror3b=abs(cp3bi-cp1bi)./abs(cp1bi);

figure (2)
plot(x1ai,percenterror2a,'b',x1ai,percenterror3a,'r',x1bi,
percenterror2b,'b',x1bi,percenterror3b,'r');

title('Percent Error for Extended Domain');
xlabel('Axial Chord, c_x');
ylabel('Percent Error of c_p');
legend('Blade 2','Blade 3');

fprintf('FERTIG\n')

```

A.2 Full Tunnel Journals

A.2.1 Gambit

```

import iceminput "L1Apsurf.dat" edge
import iceminput "L1Assurf.dat" edge

edge move "edge.1" "edge.2" offset 0 1.0101010101 0

import iceminput "L1Apsurf.dat" edge
import iceminput "L1Assurf.dat" edge

vertex create "Top_Trip" coordinates .80 0 0
vertex create "Bot_Trip" coordinates .80 3 0
edge create "Trip" straight "Top_Trip" "Bot_Trip"

edge split "edge.2" tolerance 1e-6 edge "Trip" keeptool connected
edge split "edge.4" tolerance 1e-6 edge "Trip" connected

```

```

vertex cmove "vertex.5001" multiple 1 offset .0913545 .0406737 0
vertex cmove "vertex.5002" multiple 1 offset .1813545 .0806737 0

vertex create "Fixed_B_1" coordinates -0.80000 -1.324110 0
vertex create "B_Point_1" coordinates 0.00 -0.5800000 0
vertex create "B_Point_2" coordinates 0.33 -0.3525000 0
vertex create "B_Point_3" coordinates 0.67 -0.4625000 0
vertex create "B_Point_4" coordinates 1.00 -1.0950228 0
vertex create "B_Point_5" coordinates 1.33 -1.5625000 0
vertex create "B_Point_6" coordinates 2.00 -3.0875000 0

edge create "BOTTOM" nurbs "B_Point_1" "B_Point_2" "B_Point_3"
"B_Point_4" "B_Point_5" interpolate

edge split "BOTTOM" vertex "B_Point_4" connected
vertex cmove "B_Point_4" multiple 1 offset .0913545 .0406737 0

vertex create "Fixed_T_1" coordinates -0.80000 2.141800 0
vertex create "T_Point_1" coordinates 0.00 2.5099000 0
vertex create "T_Point_2" coordinates 0.33 2.5998000 0
vertex create "T_Point_3" coordinates 0.67 2.3607000 0
vertex create "T_Point_4" coordinates 1.00 2.5698440 0
vertex create "T_Point_5" coordinates 1.33 1.6221000 0
vertex create "T_Point_6" coordinates 4.00 -2.2933300 0

edge create "TOP" nurbs "T_Point_1" "T_Point_2" "T_Point_3"
"T_Point_4" "T_Point_5" interpolate

edge split "TOP" vertex "T_Point_4" connected

edge create "TopNozzle" straight "Fixed_T_1" "T_Point_1"
edge create "BottomNozzle" straight "Fixed_B_1" "B_Point_1"

edge create "TopDiffuser" straight "T_Point_5" "T_Point_6"
edge create "BottomDiffuser" straight "B_Point_5" "B_Point_6"

vertex create "inletB" coordinates -10.6489 -8.14795 0
vertex create "inletT" coordinates -12.1719 -5.97302 0

edge create "wallB_fore" straight "Fixed_B_1" "inletB"
edge create "inlet" straight "inletB" "inletT"
edge create "wallT_fore" straight "inletT" "Fixed_T_1"
edge create "Outlet" straight "T_Point_6" "B_Point_6"
edge create "Turb_T1" straight "vertex.5001" "vertex.5003"

```

```

edge create "Turb_T2" straight "vertex.5003" "T_Point_4"
edge create "Turb_M1" straight "vertex.5002" "vertex.5004"
edge create "Turb_M2" straight "vertex.5004" "vertex.1238"
edge create "Turb_B1" nurbs "B_Point_4" "vertex.5012" "vertex.3736"

```

```

face create "Laminar" wireframe "BOTTOM" "TOP" "wallB_fore"
"inlet" "wallT_fore" "Turb_T1" "Turb_T2" "Turb_M1" "Turb_M2"
"Turb_B1" "edge.1" "edge.2" "edge.3" "edge.4" "TopNozzle"
"BottomNozzle" real

```

```

face create "Turbulent" wireframe "edge.7" "edge.8" "edge.12"
"edge.10" "Turb_T1" "Turb_T2" "Turb_M1" "Turb_M2" "Turb_B1"
"Outlet" "TopDiffuser" "BottomDiffuser" real

```

```

edge mesh "edge.1" "edge.2" "edge.3" "edge.4" "edge.7" "edge.8"
successive ratio1 1 size 0.003
edge mesh "wallT_fore" "BOTTOM" "TOP" "wallB_fore" "BottomDiffuser"
"TopDiffuser" "TopNozzle" "BottomNozzle" "edge.12" "edge.10"
successive ratio1 1 size 0.003

```

```

blayer create first 0.0005 growth 1.1 total .01588624085 rows 15
transition 1 trows 0 uniform
blayer attach "b_layer.1" face "Laminar" "Laminar" "Laminar" "Laminar"
"Laminar" "Laminar" "Laminar" "Laminar" "Laminar" "Laminar" "Turbulent"
"Turbulent" "Turbulent" "Turbulent" "Turbulent" "Turbulent" edge
"wallT_fore" "BOTTOM" "TOP" "wallB_fore" "edge.1" "edge.2" "edge.3"
"edge.4" "TopNozzle" "BottomNozzle" "edge.7" "edge.8" "edge.12"
"edge.10" "BottomDiffuser" "TopDiffuser" add

```

```

sfunction create sourceedges "wallT_fore" "TOP" "BOTTOM" "wallB_fore"
"BottomDiffuser" "TopDiffuser" "TopNozzle" "BottomNozzle" "edge.1"
"edge.2" "edge.3" "edge.4" "edge.7" "edge.8" "edge.12" "edge.10"
growthrate 1.05 sizelimit 0.03 attachfaces "Laminar" "Turbulent" meshed
sfunction bgrid attachfaces "Laminar" "Turbulent"

```

```

face mesh "Laminar" "Turbulent" triangle size 1

```

```

physics create "Wall1" btype "WALL" edge "wallB_fore" "BOTTOM"
"BottomDiffuser" "BottomNozzle" "edge.10"

```

```

physics create "Pressure2" btype "WALL" edge "edge.3"
physics create "Suction2" btype "WALL" edge "edge.4" "edge.8"
physics create "Pressure3" btype "WALL" edge "edge.1"
physics create "Suction3" btype "WALL" edge "edge.2" "edge.7"
physics create "Wall4" btype "WALL" edge "wallT_fore" "TOP" "

```



```
TopDiffuser" "TopNozzle" "edge.12"
```

```
physics create "Inlet" btype "VELOCITY_INLET" edge "inlet"
```

```
physics create "Outlet" btype "OUTFLOW" edge "Outlet"
```

```
physics create "Laminar" ctype "FLUID" face "Laminar"
```

```
physics create "Turbulent" ctype "FLUID" face "Turbulent"
```

```
export fluent5 "tunnel.msh" nozval
```

```
yes
```

```
save name "MeshCreation.dbs"
```

```
yes
```

```
exit
```

```
force
```

A.2.2 Fluent

```
file/read-case
```

```
"tunnel.cas"
```

```
/grid/smooth-grid
```

```
"skewness"
```

```
20
```

```
.4
```

```
/define/models/steady
```

```
yes
```

```
/define/models/viscous/ke-standard
```

```
yes
```

```
/define/boundary-conditions/fluid
```

```
Laminar
```

```
no
```

```
no
```

```
no
```

```
yes
```

```
0
```

```
0
```

```
no
```

```
yes
```

```
yes
```

no

/define/materials/c-c

air

air

no

no

no

yes

constant

0.000017894000000

no

no

no

no

no

no

/define/boundary-conditions/velocity-inlet

inlet

yes

yes

no

.292

no

.8192

no

.5736

no

no

yes

3

64

/solve/initialize/compute-defaults/velocity-inlet

inlet

/solve/initialize/set-defaults/y-velocity

0

/solve/initialize/initialize-flow

yes

```
/solve/monitors/residual/plot  
yes
```

```
/solve/monitors/residual/c-c  
yes  
no  
no  
no  
no
```

```
/solve/monitors/residual/convergence-criteria  
.00001
```

```
/solve/set/pvc  
21
```

```
/solve/set/ur/p  
.9
```

```
/define/profiles/u-i  
100
```

```
/solve/iterate  
1000
```

```
/plot/plot  
no  
"Pressure2a.xy"  
yes  
yes  
no  
no  
pressure-coefficient  
yes  
1  
0  
(suction2)
```

```
/plot/plot
```

no
"Pressure2b.xy"
yes
yes
no
no
pressure-coefficient
yes
1
0
(suction2:014)

/plot/plot
no
"Pressure3a.xy"
yes
yes
no
no
pressure-coefficient
yes
1
0
(suction3)

/plot/plot
no
"Pressure3b.xy"
yes
yes
no
no
pressure-coefficient
yes
1
0
(suction3:012)

/plot/plot
no
"derivative.xy"
yes
yes

```
no
no
dx-velocity-dy
yes
1
0
(wall4)
```

```
/file/write-case-data
"tunnel.cas"
yes
```

```
exit
yes
```

A.3 Test Section Journals

A.3.1 Gambit

```
import iceminput "L1Apsurf.dat" edge
import iceminput "L1Assurf.dat" edge
```

```
edge move "edge.1" "edge.2" offset 0 1.0101010101 0
```

```
import iceminput "L1Apsurf.dat" edge
import iceminput "L1Assurf.dat" edge
```

```
vertex create "Top_Trip" coordinates .80 0 0
vertex create "Bot_Trip" coordinates .80 3 0
edge create "Trip" straight "Top_Trip" "Bot_Trip"
```

```
edge split "edge.2" tolerance 1e-6 edge "Trip" keeptool connected
edge split "edge.4" tolerance 1e-6 edge "Trip" connected
```

```
vertex cmove "vertex.5001" multiple 1 offset .0913545 .0406737 0
vertex cmove "vertex.5002" multiple 1 offset .1813545 .0806737 0
```

```
vertex create "Fixed_B_1" coordinates -0.80000 -1.2516200 0
vertex create "B_Point_1" coordinates 0.00 -0.689523 0
vertex create "B_Point_2" coordinates 0.33 -0.392354279756546 0
vertex create "B_Point_3" coordinates 0.67 -0.504405438899994 0
vertex create "B_Point_4" coordinates 1.00 -1.07280480861664 0
vertex create "B_Point_5" coordinates 1.33 -1.721563339233400 0
vertex create "B_Point_6" coordinates 2.00 -3.117084741592410 0
```

```

edge create "BOTTOM" nurbs "B_Point_1" "B_Point_2" "B_Point_3"
"B_Point_4" "B_Point_5" interpolate

edge split "BOTTOM" vertex "B_Point_4" connected
vertex cmove "B_Point_4" multiple 1 offset .0913545 .0406737 0

vertex create "Fixed_T_1" coordinates -0.80000 1.9896600 0
vertex create "T_Point_1" coordinates 0.00 2.6075170000000000 0
vertex create "T_Point_2" coordinates 0.33 2.4060000000000000 0
vertex create "T_Point_3" coordinates 0.67 2.7987000000000000 0
vertex create "T_Point_4" coordinates 1.00 2.0962 0
vertex create "T_Point_5" coordinates 1.33 1.5333000000000000 0
vertex create "T_Point_6" coordinates 4.00 -2.56957 0

edge create "TOP" nurbs "T_Point_1" "T_Point_2" "T_Point_3"
"T_Point_4" "T_Point_5" interpolate

edge split "TOP" vertex "T_Point_4" connected

edge create "TopNozzle" straight "Fixed_T_1" "T_Point_1"
edge create "BottomNozzle" straight "Fixed_B_1" "B_Point_1"

edge create "TopDiffuser" straight "T_Point_5" "T_Point_6"
edge create "BottomDiffuser" straight "B_Point_5" "B_Point_6"

vertex create "inletB" coordinates -0.81916 -1.26503 0
vertex create "inletT" coordinates -2.34206 0.909899 0

edge create "wallB_fore" straight "Fixed_B_1" "inletB"
edge create "inlet" straight "inletB" "inletT"
edge create "wallT_fore" straight "inletT" "Fixed_T_1"
edge create "Outlet" straight "T_Point_6" "B_Point_6"
edge create "Turb_T1" straight "vertex.5001" "vertex.5003"
edge create "Turb_T2" straight "vertex.5003" "T_Point_4"
edge create "Turb_M1" straight "vertex.5002" "vertex.5004"
edge create "Turb_M2" straight "vertex.5004" "vertex.1238"
edge create "Turb_B1" nurbs "B_Point_4" "vertex.5012" "vertex.3736"

face create "Laminar" wireframe "BOTTOM" "TOP" "wallB_fore" "inlet"
"wallT_fore" "Turb_T1" "Turb_T2" "Turb_M1" "Turb_M2" "Turb_B1"
"edge.1" "edge.2" "edge.3" "edge.4" "TopNozzle" "BottomNozzle" real

face create "Turbulent" wireframe "edge.7" "edge.8" "edge.12"
"edge.10" "Turb_T1" "Turb_T2" "Turb_M1" "Turb_M2" "Turb_B1"

```

```

"Outlet" "TopDiffuser" "BottomDiffuser" real

edge mesh "edge.1" "edge.2" "edge.3" "edge.4" "edge.7" "edge.8"
successive ratio1 1 size 0.003

edge mesh "wallT_fore" "BOTTOM" "TOP" "wallB_fore" "BottomDiffuser"
"TopDiffuser" "TopNozzle" "BottomNozzle" "edge.12" "edge.10"
successive ratio1 1 size 0.003

blayer create first 0.0005 growth 1.1 total .01588624085 rows 15
transition 1 trows 0 uniform

blayer attach "b_layer.1" face "Laminar" "Laminar" "Laminar"
"Laminar" "Laminar" "Laminar" "Laminar" "Laminar" "Laminar"
"Laminar" "Turbulent" "Turbulent" "Turbulent" "Turbulent"
"Turbulent" "Turbulent" edge "wallT_fore" "BOTTOM" "TOP"
"wallB_fore" "edge.1" "edge.2" "edge.3" "edge.4" "TopNozzle"
"BottomNozzle" "edge.7" "edge.8" "edge.12" "edge.10"
"BottomDiffuser" "TopDiffuser" add

sfunction create sourceedges "wallT_fore" "TOP" "BOTTOM"
"wallB_fore" "BottomDiffuser" "TopDiffuser" "TopNozzle"
"BottomNozzle" "edge.1" "edge.2" "edge.3" "edge.4" "edge.7"
"edge.8" "edge.12" "edge.10" growthrate 1.05 sizelimit 0.03
attachfaces "Laminar" "Turbulent" meshed
sfunction bgrid attachfaces "Laminar" "Turbulent"

face mesh "Laminar" "Turbulent" triangle size 1

physics create "Wall1" btype "WALL" edge "wallB_fore" "BOTTOM"
"BottomDiffuser" "BottomNozzle" "edge.10"

physics create "Pressure2" btype "WALL" edge "edge.3"
physics create "Suction2" btype "WALL" edge "edge.4" "edge.8"
physics create "Pressure3" btype "WALL" edge "edge.1"
physics create "Suction3" btype "WALL" edge "edge.2" "edge.7"
physics create "Wall4" btype "WALL" edge "wallT_fore" "TOP"
"TopDiffuser" "TopNozzle" "edge.12"

physics create "Inlet" btype "VELOCITY_INLET" edge "inlet"
physics create "Outlet" btype "OUTFLOW" edge "Outlet"
physics create "Laminar" ctype "FLUID" face "Laminar"
physics create "Turbulent" ctype "FLUID" face "Turbulent"

export fluent5 "tunnel.msh" nozval

```

yes

save name "MeshCreation.dbs"

yes

exit

force

A.3.2 Fluent

/file/read-case/

"tunnel.msh"

/parallel/partition/method

metis

12

/file/write-case

"tunnel.cas"

yes

exit

yes

file/read-case

"tunnel.cas"

/grid/smooth-grid

"skewness"

20

.4

/define/models/steady

yes

/define/models/viscous/ke-standard

yes

/define/boundary-conditions/fluid

Laminar

no

no

no


```
yes
0
0
no
yes
yes
no
```

```
/define/u-d/c-f
compile
"libudf"
yes
"udf_velmag.c"
```

```
/define/u-d/c-f
load
"libudf"
```

```
/define/boundary-conditions/velocity-inlet
inlet
yes
yes
yes
yes
```

```
no
.8192
no
.5736
no
no
yes
3
64
```

```
/solve/initialize/compute-defaults/velocity-inlet
inlet
```

```
/solve/initialize/set-defaults/y-velocity
```

0

/solve/initialize/initialize-flow
yes

/solve/monitors/residual/plot
yes

/solve/monitors/residual/c-c
yes
no
no
no
no

/solve/monitors/residual/convergence-criteria
.00001

/solve/set/pvc
21

/solve/set/ur/p
.9

/define/profiles/u-i
100

/solve/iterate
1000

/plot/plot
no
"Pressure2a.xy"
yes
yes
no
no
pressure-coefficient
yes
1
0

(suction2)

/plot/plot

no

"Pressure2b.xy"

yes

yes

no

no

pressure-coefficient

yes

1

0

(suction2:014)

/plot/plot

no

"Pressure3a.xy"

yes

yes

no

no

pressure-coefficient

yes

1

0

(suction3)

/plot/plot

no

"Pressure3b.xy"

yes

yes

no

no

pressure-coefficient

yes

1

0

(suction3:012)

```
/file/write-case-data  
"tunnel.cas"  
yes
```

```
exit  
yes
```

A.3.3 UDF Fluent Files

```
x v  
-2.34206 0  
-2.340029641 0.00814434  
-2.337796246 0.0168351  
-2.335339512 0.0263379  
-2.332637095 0.0367122  
-2.329664458 0.0480225  
-2.326394541 0.0603355  
-2.322797648 0.0737169  
-2.318841045 0.0882278  
-2.314488803 0.103918  
-2.309701313 0.120817  
-2.304435088 0.138925  
-2.29864229 0.158192  
-2.29227024 0.17851  
-2.285260705 0.199695  
-2.277550536 0.221497  
-2.269068991 0.243628  
-2.259739731 0.265816  
-2.249477225 0.286454  
-2.233482153 0.298769  
-2.215183741 0.303468  
-2.195291818 0.307039  
-2.173667295 0.30994  
-2.150159094 0.311975  
-2.124603348 0.313001  
-2.096814607 0.313233  
-2.066520691 0.313018  
-2.033427037 0.312635  
-1.997275455 0.312238  
-1.957800958 0.31188  
-1.915113058 0.311553  
-1.869577859 0.311219  
-1.821404793 0.310853  
-1.772220543 0.310465  
-1.723396003 0.31012
```

-1.675198956 0.309891
-1.627625405 0.309769
-1.58067535 0.309727
-1.533725295 0.309769
-1.486151744 0.309891
-1.437954697 0.31012
-1.389130157 0.310465
-1.339945907 0.310853
-1.29177284 0.311219
-1.246237642 0.311553
-1.203549743 0.31188
-1.164075246 0.312238
-1.127923663 0.312635
-1.09483001 0.313018
-1.064536093 0.313233
-1.036747352 0.313001
-1.011191606 0.311975
-0.987683405 0.30994
-0.966058882 0.307039
-0.946166959 0.303468
-0.927868548 0.298769
-0.911873475 0.286454
-0.901610969 0.265816
-0.892281709 0.243628
-0.883800164 0.221497
-0.876089995 0.199695
-0.86908046 0.17851
-0.86270841 0.158192
-0.856915612 0.138925
-0.851649388 0.120817
-0.846861897 0.103918
-0.842509654 0.0882278
-0.838553052 0.0737169
-0.834956159 0.0603355
-0.831686242 0.0480225
-0.828713604 0.0367122
-0.826011189 0.0263379
-0.823554454 0.0168351
-0.821321059 0.00814434
-0.8192907 0

```
/*  
udf_velmag.c  
UDF for specifying a steady-state velocity profile boundary condition  
*/
```

```

#include "udf.h" /* must be at the beginning of every UDF you write */

real plinterp(real *x, real *y, int n, real xp);

DEFINE_PROFILE(velocity_magnitude,thread,index)
{
    real loc[ND_ND]; /* this will hold the position vector */
    real x;
    face_t f;

    FILE *fp0;
    static real inx[1000];
    static real inu[1000];
    char str[50];

    if ((fp0=fopen("velmag_profile.txt","r"))==NULL)
    {
        Message0(" Cannot open velmag_profile.txt\n");
    }
    else
    {
        Message0(" Opened velmag_profile.txt\n");
    }
    fgets(str,50,fp0);
    int n=0;
    while (fscanf(fp0,"%f %f",&inx[n],&inu[n]) != EOF)
    {
        Message0("    x: %f\tu: %f\n",inx[n],inu[n]);
        n++;
    }

    begin_f_loop(f,thread) /* loops over all faces in the thread passed
                           in the DEFINE macro argument */
    {
        F_CENTROID(loc,f,thread);
        x = loc[0];
        F_PROFILE(f,thread,index) = plinterp(inx,inu,n,x);
    }
    end_f_loop(f,thread)
}

real plinterp(real *x, real *y, int n, real xp)
{
    int i;

```

```

if(xp < x[0])
{
    return (-999.);
}

if(xp > x[n-1])
{
    return (999.);
}

i=0;
while(x[i] < xp) i++;
return (y[i-1]+(xp-x[i-1])*(y[i]-y[i-1])/(x[i]-x[i-1]));
}

```

A.4 Streamline ICEM Coordinates

```

2 9
-0.8 2.1479 0
-0.55 2.3023 0
-0.3 2.4141 0
-0.05 2.4845 0
0.2 2.5435 0
0.45 2.5495 0
0.7 2.4772 0
0.95 2.3715 0
1.2 1.8418 0

```